NAVAL POSTGRADUATE SCHOOL

MONTEREY, CALIFORNIA

THESIS

LANGMUIR CIRCULATIONS IN A COASTAL ENVIRONMENT DURING CBLAST

by

Murat ELGE

September 2004

Thesis Advisor:	Timothy P. Stanton
Second Reader:	Edward B. Thornton

REPORT DOCUMENTATION PAGE			*Form Approved OMB No. 0704-0188*
Public reporting burden for this collection of information is estimated to average 1 hour per response, including the time for reviewing instruction, searching existing data sources, gathering and maintaining the data needed, and completing and reviewing the collection of information. Send comments regarding this burden estimate or any other aspect of this collection of information, including suggestions for reducing this burden, to Washington headquarters Services, Directorate for Information Operations and Reports, 1215 Jefferson Davis Highway, Suite 1204, Arlington, VA 22202-4302, and to the Office of Management and Budget, Paperwork Reduction Project (0704-0188) Washington DC 20503.			
1. AGENCY USE ONLY (*Leave blank*)	**2. REPORT DATE** September 2004	**3. REPORT TYPE AND DATES COVERED** Master's Thesis	
4. TITLE AND SUBTITLE: Langmuir circulations in a coastal environment during CBLAST			**5. FUNDING NUMBERS**
6. AUTHOR(S) Murat Elge			
7. PERFORMING ORGANIZATION NAME(S) AND ADDRESS(ES) Naval Postgraduate School Monterey, CA 93943-5000			**8. PERFORMING ORGANIZATION REPORT NUMBER**
9. SPONSORING /MONITORING AGENCY NAME(S) AND ADDRESS(ES) Office of Naval Research			**10. SPONSORING/MONITORING AGENCY REPORT NUMBER**
11. SUPPLEMENTARY NOTES The views expressed in this thesis are those of the author and do not reflect the official policy or position of the Department of Defense or the U.S. Government.			
12a. DISTRIBUTION / AVAILABILITY STATEMENT Approved for public release; distribution is unlimited			**12b. DISTRIBUTION CODE**
13. ABSTRACT (maximum 200 words) Langmuir circulations in a coastal environment at an inner shelf site with strong tidal forcing were examined using a 4-month observation of high-resolution velocity profiles during the ONR-sponsored CBLAST-Low air-sea interaction experiment. Because of their potential contributions to mixing processes in the surface boundary layer, Langmuir circulations are important for naval operations such as ASW, MCM and Amphibious operations in littoral waters. A detection algorithm for upwelling / downwelling velocities due to Langmuir circulations was developed. Analyses focused on long-fetch, unstratified water column conditions with locally developed seas. The observations showed that strong Langmuir circulations greatly reduced water column shear arising from the tidally forced bottom boundary layer, while there was no significant effect from the strong tidal boundary layer on the formation of Langmuir cells. Long fetch conditions had the strongest vertical velocities with Langmuir number 0.1-0.4, while short fetch conditions have weaker vertical velocities with Langmuir number greater than 0.5. Cell vertical velocities were correlated with the water friction velocity, but penetration depths did not depend on forcing mechanisms. Spacing and penetration depths were correlated for increasing wind speed and wave heights whereas this correlation was not seen for constant high wind speed and wave heights.			
14. SUBJECT TERMS Langmuir circulations, Coastal environment, Mixing processes in upper ocean, Turbulence flow, Tidal current.			**15. NUMBER OF PAGES** 125
			16. PRICE CODE
17. SECURITY CLASSIFICATION OF REPORT Unclassified	**18. SECURITY CLASSIFICATION OF THIS PAGE** Unclassified	**19. SECURITY CLASSIFICATION OF ABSTRACT** Unclassified	**20. LIMITATION OF ABSTRACT** UL

THIS PAGE INTENTIONALLY LEFT BLANK

LANGMUIR CIRCULATIONS IN A COASTAL ENVIRONMENT DURING CBLAST

Murat ELGE
Lieutenant Junior Grade, Turkish Navy
B.E., Turkish Naval Academy, 1998

Submitted in partial fulfillment of the
requirements for the degree of

**MASTER OF SCIENCE IN
METEOROLOGY AND PHYSICAL OCEANOGRAPGHY**

from the

**NAVAL POSTGRADUATE SCHOOL
September 2004**

Author: Murat Elge

Approved by: Timothy P. Stanton
                 Thesis Advisor

                 Edward B. Thornton
                 Second Reader

                 Mary Batteen
                 Chairman, Department of Oceanography

iii

THIS PAGE INTENTIONALLY LEFT BLANK

ABSTRACT

Langmuir circulations in a coastal environment at an inner shelf site with strong tidal forcing were examined using a 4-month observation of high-resolution velocity profiles during the ONR-sponsored CBLAST-Low air-sea interaction experiment. Because of their potential contributions to mixing processes in the surface boundary layer, Langmuir circulations are important for naval operations such as ASW, MCM and Amphibious operations in littoral waters. A detection algorithm for upwelling / downwelling velocities due to Langmuir circulations was developed. Analyses focused on long-fetch, unstratified water column conditions with locally developed seas. The observations showed that strong Langmuir circulations greatly reduced water column shear arising from the tidally forced bottom boundary layer, while there was no significant effect from the strong tidal boundary layer on the formation of Langmuir cells. Long fetch conditions had the strongest vertical velocities with Langmuir number 0.1-0.4, while short fetch conditions have weaker vertical velocities with Langmuir number greater than 0.5. Cell vertical velocities were correlated with the water friction velocity, but penetration depths did not depend on forcing mechanisms. Spacing and penetration depths were correlated for increasing wind speed and wave heights whereas this correlation was not seen for constant high wind speed and wave heights.

THIS PAGE INTENTIONALLY LEFT BLANK

TABLE OF CONTENTS

LIST OF FIGURES

THIS PAGE INTENTIONALLY LEFT BLANK

LIST OF TABLES

THIS PAGE INTENTIONALLY LEFT BLANK

ACKNOWLEDGMENTS

THIS PAGE INTENTIONALLY LEFT BLANK

I.   INTRODUCTION

The physical processes controlling atmosphere ocean momentum and scalar fluxes in the presence of waves remain an important research topic in Physical Oceanography and Meteorology. Meteorologists are trying to understand the effects of ocean waves in high and low wind conditions by examining the temperature, turbulence and humidity profiles in the Marine Boundary Layer (MBL) while the oceanographers are interested in measuring surface fluxes in Ocean Boundary Layers (OBL).

Mixing processes in the wind forced ocean surface boundary layer (OSBL) are very different from the wall boundary layers due to the action of surface gravity waves that modify the momentum, heat and gas exchange between the MBL and OSBL. The main physical processes that govern the mixing in OSBL are convective forcing due to night time cooling, shear stress instability generated by wind stress acting through waves and wave breaking, and Langmuir circulations resulting from the interactions between surface gravity waves and the wind driven surface currents.

A.   MOTIVATION OF THIS STUDY

Langmuir circulations in a coastal environment are investigated in this study to understand the role of coherent structures seen below wind-forced waves in mixing across the ocean mixed layer. In inner shelf coastal environments, the surface layer frequently interacts with a tidally forced bottom boundary layer in unstratified conditions. It is important for modern, high-resolution regional numerical models to correctly parameterize these multiple turbulent processes in littoral regions.

Langmuir circulations (Figure 1.1) are counter rotating vortices with convergence zones above the downwelling regions and divergence zones above the upwelling regions at the sea surface. They exist in the surface boundary layer due to the interactions between strong wind driven surface currents and the Stokes drifts of surface gravity waves. Under unstratified conditions, continental shelf circulations can penetrate down to the ocean bottom and have dominant effects on the turbulent kinetic energy budget (TKE) across the water column.
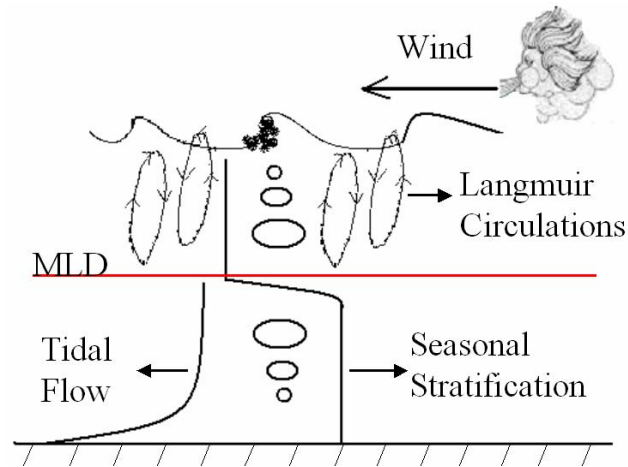
Figure 1.1   The mixing processes in a coastal region. The eddies due to surface mixing processes in surface boundary layer and the eddies due to strong tidal flow in bottom boundary layer are separated by the seasonal stratification (summer time) and merge with unstratified ocean (winter time). MLD is the mixing layer depth.

Langmuir circulations in a coastal environment with strong tidal forcing were examined using a 4-month observation of high-resolution velocity during CBLAST (Coupled Boundary Layers Air Sea Transfer) at a coastal observatory south of Martha's Vineyard during the fall of 2003. The study focuses on conditions with long fetch waves, an unstratified ocean water column and locally well-developed waves. An algorithm to detect downwelling / upwelling regions of Langmuir circulations was created for the vertically oriented beam of five beam BADCP (Broadband Acoustic Doppler Current Profiler) high-resolution velocity profiles. A review of ocean TKE budget and Langmuir circulations overview is given in Chapter II. Method of data collection with five beam BADCP and description of CBLAST experiment site is introduced in Chapter III. Methods used for data processing to detect Langmuir circulations and their features are explained in Chapter IV. Analysis, including definition of the supporting conditions of Langmuir circulations, Langmuir number calculation and relationship with the detected downwelling / upwelling velocities, the correlations between the downwelling / upwelling and the water friction velocity, horizontal and vertical length scales is discussed in Chapter V. Conclusions are presented in Chapter VI.

II. TURBULENCE FLOW AND LANGMUIR CIRCULATIONS

A. TURBULENCE FLOW

Turbulent flow exists in the upper ocean due to the mixing processes forced by convection and free convection. In this study, forced convection due to surface wind stress in the presence of surface gravity waves will primarily be considered. The important parameters to define the turbulent flow are the Richardson number and the Reynolds numbers. In this chapter, the turbulent kinetic energy equations for stratified flow are summarized to provide an overview of turbulent processes found in the coastal ocean.

The gradient shear stability Richardson number is a measure of the stability of the ocean flow, and it is the ratio of static stability and dynamic stability.

$$Ri = \frac{N^2}{|shear|^2} \tag{2.1}$$

where N is Brunt-Vaisala or buoyancy frequency,

$$N^2 = -\frac{g}{\rho_\theta} \times \frac{\partial \rho_\theta}{\partial z} \tag{2.2}$$

The g is gravitational acceleration, $-\frac{\partial \rho_\theta}{\partial z}$ is the stratification measured by the vertical density gradient and z is the depth, which is positive upward. Negative vertical density gradients represent a hydrostatically unstable ocean, which lead to convective instability, while a positive vertical density gradient represent a hydrostatically stable ocean. Sustained hydrostatically unstable conditions arise from free convection forces that are typically due to thermal cooling of the ocean surface.

The shear term in the denominator of Equation 2.1 is another factor responsible for turbulent flow and represents the forced convection. Forced convection in the coastal ocean is due to wind forcing, internal wave interactions, frontal and meso-scale horizontal shear, and the current interactions with the seabed. Shear in the water column creates horizontal and vertical vortices. If the Richardson number is less than ~ ¼,

turbulent flow is more likely to exist. The higher the shear term, the smaller the Richardson number is, and the stronger the turbulent flow.
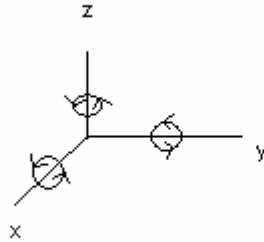
Figure 2.1   x, y and z coordinate system with vorticity circles.

For the coordinate system defined in Figure 2.1, u, v and w are the x, y, z velocity components of the velocity field respectively. The vorticitiy equations for x, y and z-axis are given in the Equations 2.3 through 2.5 respectively.

$$\omega_x = -\frac{\partial v}{\partial z} + \frac{\partial w}{\partial y} \tag{2.3}$$

$$\omega_y = \frac{\partial u}{\partial z} - \frac{\partial w}{\partial x} \tag{2.4}$$

$$\omega_z = -\frac{\partial u}{\partial y} + \frac{\partial v}{\partial x} \tag{2.5}$$

All the terms on the right hand side of the Equations 2.3 through 2.5 represent fluid shear components. The z-vorticity Equation 2.5 doesn't have any vertical component of the flow, which means there is no vertical mixing in this equation. The vertical mixing process exists only in the x-vorticity and y-vorticity equations.

Reynolds number is another estimation of strength of turbulent flow, defined as the ratio of inertial forces (advection terms) and viscous forces in the equations of motion (Equation 2.6)

$$\mathrm{Re} = \frac{U\,L}{\upsilon} \tag{2.6}$$

4

Where U is the velocity scale, L is the horizontal length scale and υ is the viscosity. If Reynolds numbers are much larger than one or greater than 2000, turbulent flow is likely to exist due to negligible molecular friction effects. This condition is true not only for turbulent flow, but also for every kind of flow in the ocean. The friction term in the equations of motion (momentum equations) depends upon the fluid characteristics and for most scales of motion in the ocean can be neglected, although all motions are dissipated due to the fluid viscosity at small (0.1-10 mm) scales.

Turbulence needs a continuing source of energy to be sustained. The basic balance of turbulent kinetic energy is given by

$$\frac{d}{dt}\left(\frac{TKE}{VOLUME}\right) = \frac{WORK\ RATE}{VOLUME} - \frac{VICOUS\ DISSIPATION}{VOLUME} \tag{2.7}$$

where TKE is turbulent kinetic energy, work rate is combination of the work done by free convection (thermally driven) and forced convection (wind forced), and the viscous term is the dissipation rate of the turbulence, which is commonly known as ε.

The driving properties of motion in the ocean can be generalized into the three processes of momentum, heat content and salt concentration. The motion driven by these processes have mean and fluctuating parts. If the driving property is called F, the conservation laws lead to Equation 2.8 and 2.9. Equation 2.9 is known as the continuity equation.

$$\frac{dF}{dt} = \frac{\partial F}{\partial t} + u\frac{\partial F}{\partial x} + v\frac{\partial F}{\partial y} + w\frac{\partial F}{\partial z} = \kappa_T \left(\frac{\partial^2 F}{\partial x^2} + \frac{\partial^2 F}{\partial y^2} + \frac{\partial^2 F}{\partial z^2}\right) + R_F \tag{2.8}$$

$$\frac{\partial u}{\partial x} + \frac{\partial v}{\partial y} + \frac{\partial w}{\partial z} = 0 \tag{2.9}$$

R_F represents the nonconservative processes in (2.8). The mean part of Equation 2.8 can be combined with Equation 2.9 to give Equation 2.10,

$$\frac{\partial \overline{F}}{\partial t} + \overline{u}\frac{\partial \overline{F}}{\partial x} + \overline{v}\frac{\partial \overline{F}}{\partial y} + \overline{w}\frac{\partial \overline{F}}{\partial z} + \frac{\partial \overline{u'F'}}{\partial x} + \frac{\partial \overline{v'F'}}{\partial y} + \frac{\partial \overline{w'F'}}{\partial z} = \kappa_T \left(\frac{\partial^2 \overline{F}}{\partial x^2} + \frac{\partial^2 \overline{F}}{\partial y^2} + \frac{\partial^2 \overline{F}}{\partial z^2}\right) + \overline{R_F} \tag{2.10}$$

The next step is to derive the variance equation for F. Variance is defined as $\overline{F'^2} = \overline{F'F'}$, this variance is a measure of the turbulent generation of fluctuations in F. By subtracting (2.10) from (2.8), multiplying by $2F'$, and taking the mean of each term while assuming horizontal homogeneity, a generalized variance budget for atmospheric and oceanic boundary layers results as,

$$\frac{\partial}{\partial t}\left(\frac{\overline{F'^2}}{2}\right) = -\overline{F'w'}\frac{\partial \overline{F}}{\partial z} - \frac{\partial}{\partial z}\left[\overline{w'\left(\frac{F'^2}{2}\right)}\right] - \kappa_F\left[\overline{\left(\frac{\partial F'}{\partial x}\right)^2} + \overline{\left(\frac{\partial F'}{\partial y}\right)^2} + \overline{\left(\frac{\partial F'}{\partial z}\right)^2}\right] + \overline{F'R_F'} \quad (2.11)$$

The first term is the unsteady rate of increase/decrease and usually called "storage term", the second term is "gradient production" and is always positive because of the second law of thermodynamics, the third term is the turbulent diffusion of variance through the water column, the fourth term is the rate of dissipation variance and can only be negative, the last term is collection of the nonconservative processes if they exist.

If F represents a horizontal velocity component u, the turbulent kinetic energy equation for this component is,

$$\frac{\partial}{\partial t}\left(\frac{\overline{u'^2}}{2}\right) = -\overline{u'w'}\frac{\partial \overline{u}}{\partial z} - \frac{\partial}{\partial z}\left[\overline{w'\left(\frac{u'^2}{2}\right)}\right] + \overline{R_u'^2} - \varepsilon_{u'^2} \quad (2.12)$$

$$\varepsilon_{u'^2} = \upsilon\left[\overline{\left(\frac{\partial u'}{\partial x}\right)^2} + \overline{\left(\frac{\partial u'}{\partial y}\right)^2} + \overline{\left(\frac{\partial u'}{\partial z}\right)^2}\right] \quad (2.13)$$

However, the processes and mathematical terms represented by R have not been defined yet. The u-momentum equation will be used to make this definition,

$$\frac{\partial u}{\partial t} + u\frac{\partial u}{\partial x} + v\frac{\partial u}{\partial y} + w\frac{\partial u}{\partial z} = \upsilon\left(\frac{\partial^2 u}{\partial x^2} + \frac{\partial^2 u}{\partial y^2} + \frac{\partial^2 u}{\partial z^2}\right) + 2\Omega_z v - 2\Omega_y w - \frac{1}{\rho}\frac{\partial p}{\partial x} \quad (2.14)$$

and by comparing (2.14) with (2.8), the nonconservative term is,

$$R_u = 2\Omega_z v - 2\Omega_y w - \frac{1}{\rho}\frac{\partial p}{\partial x} \tag{2.15}$$

Since all the terms are linear in Equation 2.15, averaging rules can be used to get the mean version of R_u,

$$\bar{R}_u = 2\Omega_z \bar{v} - 2\Omega_y \bar{w} - \frac{1}{\rho}\frac{\partial \bar{p}}{\partial x} \tag{2.16}$$

The complete mean u-momentum equation is,

$$\frac{\partial \bar{u}}{\partial t} + \bar{u}\frac{\partial \bar{u}}{\partial x} + \bar{v}\frac{\partial \bar{u}}{\partial y} + \bar{w}\frac{\partial \bar{u}}{\partial z} + \frac{\partial \overline{u'u'}}{\partial x} + \frac{\partial \overline{v'u'}}{\partial y} + \frac{\partial \overline{w'u'}}{\partial z} =$$
$$\upsilon\left(\frac{\partial^2 \bar{u}}{\partial x^2} + \frac{\partial^2 \bar{u}}{\partial y^2} + \frac{\partial^2 \bar{u}}{\partial z^2}\right) + 2\Omega_z \bar{v} - 2\Omega_y \bar{w} - \frac{1}{\rho}\frac{\partial \bar{p}}{\partial x} \tag{2.17}$$

The last step is to define the nonconservative part, $\overline{F'R_F'}$, of the variance budget (2.11) by using (2.16),

$$\overline{u'R_u'} = \overline{u'\left(2\Omega_z v' - 2\Omega_y w' - \frac{1}{\rho}\frac{\partial p'}{\partial x}\right)} = 2\Omega_z\overline{u'v'} - 2\Omega_y\overline{u'w'} - \frac{1}{\rho}\overline{u'\frac{\partial p'}{\partial x}} \tag{2.18}$$

Substituting (2.18) in (2.12) the final version of the u-TKE equation is obtained,

$$\frac{\partial}{\partial t}\left(\frac{\overline{u'^2}}{2}\right) = -\overline{u'w'}\frac{\partial \bar{u}}{\partial z} - \frac{\partial}{\partial z}\left[\overline{w'\left(\frac{u'^2}{2}\right)}\right] - \varepsilon_{u'^2} - 2\Omega_y\overline{u'w'} + 2\Omega_z\overline{u'v'} - \frac{p'}{\rho}\frac{\partial u'}{\partial x} \tag{2.19}$$

The corresponding Reynolds and TKE equations for v resemble their counterpart Equations 2.17 and 2.19, except for the Coriolis terms.

$$\frac{\partial \bar{v}}{\partial t} + \bar{u}\frac{\partial \bar{v}}{\partial x} + \bar{v}\frac{\partial \bar{v}}{\partial y} + \bar{w}\frac{\partial \bar{v}}{\partial z} + \frac{\partial \overline{u'v'}}{\partial x} + \frac{\partial \overline{v'v'}}{\partial y} + \frac{\partial \overline{w'v'}}{\partial z} =$$
$$\upsilon\left(\frac{\partial^2 \bar{v}}{\partial x^2} + \frac{\partial^2 \bar{v}}{\partial y^2} + \frac{\partial^2 \bar{v}}{\partial z^2}\right) + 2\Omega_z\bar{u} - \frac{1}{\rho}\frac{\partial \bar{p}}{\partial y} \tag{2.20}$$

$$\frac{\partial}{\partial t}\left(\frac{\overline{v'^2}}{2}\right) = -\overline{v'w'}\frac{\partial \overline{v}}{\partial z} - \frac{\partial}{\partial z}\left[\overline{w'\left(\frac{v'^2}{2}\right)}\right] - \varepsilon_{v'^2} - 2\Omega_z\overline{u'v'} - \frac{\overline{p'}}{\rho}\frac{\partial v'}{\partial y} \qquad (2.21)$$

The vertical balance of forces in flux form and multiplied through by density is defined in Equation 2.22, before deriving the vertical Reynolds equation and vertical TKE equation.

$$\rho\left(\frac{\partial w}{\partial t} + \frac{\partial uw}{\partial x} + \frac{\partial vw}{\partial y} + \frac{\partial ww}{\partial z}\right) = 2\rho\Omega_y u - \frac{\partial \tilde{p}}{\partial z} - \rho g + \rho\upsilon\left(\frac{\partial^2 w}{\partial x^2} + \frac{\partial^2 w}{\partial y^2} + \frac{\partial^2 w}{\partial z^2}\right) \qquad (2.22)$$

The hydrostatic approximation "$0 = -\frac{\partial \tilde{p}}{\partial z} - \rho g$", which is acceptable for large-scale motions, neglects the vertical accelerations due to the fluctuations in density and pressure and will exclude the turbulent motion and small-scale internal waves. It is necessary to keep the vertical forces that cause the vertical accelerations in Equation 2.22 in order to describe turbulent motion. The "Boussinesq Approximation" can be used to accomplish this. The total pressure, $\tilde{p}$, is broken into two parts, hydrostatic pressure P and dynamic pressure p according to the Boussinesq approximation. Hydrostatic pressure is the pressure that would be caused by representative or average density ρ_o and if the fluid were motionless with no horizontal forces, is defined as,

$$\frac{\partial P}{\partial z} = -\rho_o g \qquad (2.23)$$

Substituting (2.23) into total pressure and gravity terms in (2.21),

$$-\frac{\partial \tilde{p}}{\partial z} - \rho g = \left[\frac{\partial(P+p)}{\partial z}\right] - \rho g = g(\rho_o - \rho) - \frac{\partial p}{\partial z} \qquad (2.24)$$

"Buoyancy force" or "reduced gravity force" is defined as,

$$g' = b = \frac{g(\rho_o - \rho(t,x,y,z))}{\rho_o} \qquad (2.25)$$

Substituting (2.25) in (2.24),

$$-\frac{\partial \tilde{p}}{\partial z} - \rho g \cong \rho_o b - \frac{\partial p}{\partial z} \qquad (2.26)$$

Finally substituting (2.26) in (2.21), getting an average of each term and dividing each term by ρ_o in (2.21), the vertical Reynolds equation is obtained as,

$$\frac{\partial \overline{w}}{\partial t} + \frac{\partial \overline{uw}}{\partial x} + \frac{\partial \overline{vw}}{\partial y} + \frac{\partial \overline{ww}}{\partial z} + \frac{\partial \overline{u'w'}}{\partial x} + \frac{\partial \overline{v'w'}}{\partial y} + \frac{\partial \overline{w'w'}}{\partial z} =$$
$$2\Omega_y \overline{u} - \frac{1}{\rho_o}\frac{\partial \overline{p}}{\partial z} + \overline{b} + \upsilon\left(\frac{\partial^2 \overline{w}}{\partial x^2} + \frac{\partial^2 \overline{w}}{\partial y^2} + \frac{\partial^2 \overline{w}}{\partial z^2}\right) \qquad (2.27)$$

Buoyancy force described in (2.25) has mean and fluctuating parts, $b = \overline{b} + b'$ and $b' \cong -\rho' g / \rho_o$. Fluctuations in buoyancy force cause positive or upward and negative or downward accelerations attributable to the negative density fluctuations and positive density fluctuations respectively.

w-TKE equation is obtained by subtracting (2.27) from (2.22), multiplying by w' and averaging the resultant equation.

$$\frac{\partial}{\partial t}\left(\frac{\overline{w'^2}}{2}\right) = -\frac{\partial}{\partial z}\left[\overline{w'\left(\frac{w'^2}{2}\right)}\right] - \frac{\partial}{\partial z}\left[\frac{\overline{w'p'}}{\rho_o}\right] + \overline{b'w'} + 2\Omega_y \overline{u'w'} - \frac{\overline{p'}}{\rho_o}\frac{\partial w'}{\partial z} - \varepsilon_{w'^2} \qquad (2.28)$$

The two differences between vertical TKE Equation 2.28 and the horizontal TKE equations (2.21), (2.19) are that there is no gradient production term and there is an extra buoyancy flux, $\overline{b'w'}$, in vertical TKE equation. There is also no gradient production term because there is no shear in $\overline{w}$ if mean flow is horizontal.

Summarizing what has been done so far, three components of the TKE and the Reynolds equations are derived assuming horizontal homogeneity. The u, v and w components of TKE are rewritten in Equations 2.29, 2.30 and 2.31 respectively in order to explain the physical meanings of each term.

$$\frac{\partial}{\partial t}\left(\frac{\overline{u'^2}}{2}\right) = -\overline{u'w'}\frac{\partial \overline{u}}{\partial z} - \frac{\partial}{\partial z}\left[\overline{w'\left(\frac{u'^2}{2}\right)}\right] - \varepsilon_{u'^2} - \frac{\overline{p'}}{\rho}\frac{\partial u'}{\partial x} - 2\Omega_y \overline{u'w'} + 2\Omega_z \overline{u'v'} \qquad (2.29)$$

9

$$\frac{\partial}{\partial t}\left(\frac{\overline{v'^2}}{2}\right) = -\overline{v'w'}\frac{\partial \overline{v}}{\partial z} - \frac{\partial}{\partial z}\left[\overline{w'\left(\frac{v'^2}{2}\right)}\right] - \varepsilon_{v'^2} - \frac{\overline{p'}}{\rho}\frac{\partial v'}{\partial y} - 2\Omega_z \overline{u'v'} \tag{2.30}$$

$$\frac{\partial}{\partial t}\left(\frac{\overline{w'^2}}{2}\right) = \overline{b'w'} - \frac{\partial}{\partial z}\left[\overline{w'\left(\frac{w'^2}{2} + \frac{p'}{\rho_o}\right)}\right] - \varepsilon_{w'^2} - \frac{\overline{p'}}{\rho_o}\frac{\partial w'}{\partial z} + 2\Omega_y \overline{u'w'} \tag{2.31}$$

The physical processes identified by each term are the most necessary part of understanding the turbulent flow. The first terms are the time rate of change of the TKE or "storage terms". If there is a statistical steady state, these terms are equal to zero. Due to the usual rapid time adjustment of turbulence to changes in forcing, these terms are often assumed to be negligible compared with the production and dissipation terms described below.

The second terms are called "Production Terms" which represents the production processes of turbulence. The second terms in (2.29) and (2.30) are the shear production terms which are caused by forced convection and the Reynolds stresses working against the mean shear. The second term, buoyancy flux term, in (2.31) is called buoyant production only if it is positive. The buoyancy flux, $\overline{b'w'}$, will be positive when the mean vertical density gradient is positive, and the mean vertical buoyancy gradient is therefore negative. This is the hydrostatically unstable case and free convection occurs where consecutive buoyant parcels of fluid rise and denser particles sink due to the gravity. On the other hand, whenever the mean density profile is stable or negative, the buoyancy flux term in (2.31) will be negative. In this case, the vertical mixing due to mechanical or forced convection will be damped by the buoyancy flux term, so the buoyancy flux term will act as an obstacle to the vertical TKE, and will result in a loss of the vertical TKE instead of a gain in it. This is frequently the case for the oceanic mixed layer in the afternoon due to solar heating of the ocean surface while, the marine atmospheric boundary layer is less likely to become strongly stable unless warm air is horizontally advected over cold water and creates the inversion layer. Over the land, the atmospheric boundary layer is likely to be stable due to the radiation inversion at night, after the ground has given up heat by long wave radiation to sky.

10

The third terms represents the vertical transport of turbulence by itself. If $w^{'}$ carries the TKE, advective turbulent transport occurs. The vertical TKE equation has an additional kind of transport, which is called as pressure transport. The pressure transport occurs when fluid parcels exchange energy vertically by collision. The transport terms only move the total energy around vertically and they never change it. Consequently if the sign of these terms is negative at a given height, it must be positive at another height.

The fourth, or ε terms are the viscous dissipation terms and are effective at the smallest scale (Kolmogorov micro scale) of the turbulence where molecular viscosity overwhelms inertial components of the turbulence.

The fifth terms in each component are pressure-strain correlation terms. These terms explain the energy transfer among the three components. Pressure can also transfer the kinetic energy from one direction to the lateral direction. Since the TKE is conservative, the summation of these terms in each component will be zero.

The last terms represents the Coriolis redistribution of a fluid parcel. The motion of a fluid parcel changes its direction under the Coriolis force to the right in northern hemisphere and to the left in southern hemisphere, but the total kinetic energy remains the same. The summation of these terms in each component is zero.

The total TKE equation can be obtained by adding up Equations 2.29, 2.30 and (2.31). The total TKE is,

$$\frac{\partial}{\partial t}\left[\frac{\overline{u^{'2}+v^{'2}+w^{'2}}}{2}\right]=\left[-\overline{u^{'}w^{'}}\frac{\partial \overline{u}}{\partial z}-\overline{v^{'}w^{'}}\frac{\partial \overline{v}}{\partial z}\right]+\left[\overline{b^{'}w^{'}}\right]-\frac{\partial}{\partial z}\left[\overline{w^{'}\left(\frac{u^{'2}+v^{'2}+w^{'2}}{2}+\frac{p^{'}}{\rho_{o}}\right)}\right]-\left[\varepsilon\right] \quad (2.32)$$

The dissipation term has nine components in it, which are the combination of each TKE component's dissipation terms.

$$\varepsilon = \varepsilon_{u^{'2}}+\varepsilon_{v^{'2}}+\varepsilon_{w^{'2}}=\upsilon\left[\begin{array}{c}\overline{\left(\frac{\partial u^{'}}{\partial x}\right)^{2}}+\overline{\left(\frac{\partial u^{'}}{\partial y}\right)^{2}}+\overline{\left(\frac{\partial u^{'}}{\partial z}\right)^{2}}\\+\overline{\left(\frac{\partial v^{'}}{\partial x}\right)^{2}}+\overline{\left(\frac{\partial v^{'}}{\partial y}\right)^{2}}+\overline{\left(\frac{\partial v^{'}}{\partial z}\right)^{2}}\\+\overline{\left(\frac{\partial w^{'}}{\partial x}\right)^{2}}+\overline{\left(\frac{\partial w^{'}}{\partial y}\right)^{2}}+\overline{\left(\frac{\partial w^{'}}{\partial z}\right)^{2}}\end{array}\right] \quad (2.33)$$

11

At the finest scales, Kolmogorov micro scale, turbulence is nearly isotropic and there is no direction preference at these scales, so each component of ε is 1/3 of the total dissipation. Furthermore, the total dissipation is approximately fifteen times any one of the diagonal terms in (2.33) due to the isotropy. Hence ε can be presented as,

$$\varepsilon = 3\varepsilon_{u^{'2}} + 3\varepsilon_{v^{'2}} + 3\varepsilon_{w^{'2}} = 15\upsilon \overline{\left(\frac{\partial u^{'}}{\partial x}\right)^2} = 15\upsilon \overline{\left(\frac{\partial v^{'}}{\partial y}\right)^2} = 15\upsilon \overline{\left(\frac{\partial w^{'}}{\partial z}\right)^2} \qquad (2.34)$$

The energy spectrum of the total TKE shows us how strong the turbulent velocity is at different time or length scales. The log-log plot of the wave number and the correspondent energy at each wave number for a steadily forced flow is shown in Figure (2.2).
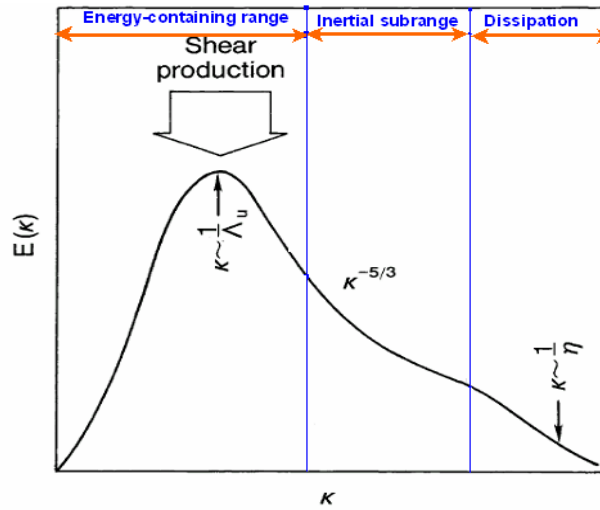
Figure 2.2   Energy Density Spectrum of TKE: k is wave number (1/cm), E (k) is the Energy as a function of k

Figure 2.2 shows the energy density spectrum of TKE for a steadily forced turbulent fluid with forcing scales much larger than dissipation scales. If the Reynolds number is much larger than one, which means small molecular viscosity, an inertial-sub range occurs. The wider the (in wave number space) inertial sub range, the larger the TKE. If the slope of the inertial sub range is at least $k^{-5/3}$, there is a turbulent flow. Energy enters the flow at low frequencies, at macro scale, and then this energy is transported from larger eddies to the smaller eddies along the energy density spectrum. Λ is the integral or macro scale of turbulent flow. This is the scale where the largest

12

eddies occur. η is the Kolmogorov or micro scale of the turbulent flow and is the scale of the smallest eddies where molecular viscosity becomes important, and finally dissipation of the turbulent flow occurs.

The basic equations related to turbulent flow and their physical meanings were explained since the Langmuir circulations, the main focus of this study, are coherent motions that co-exist with turbulent eddies in ocean mixed layers in the presence of wind forcing and waves. These circulations play an important role for the mixing in the upper ocean. A review of these circulations will be given in the next section.

B.   LANGMUIR CIRCULATIONS

Langmuir circulations are parallel series of the counter rotating helical vortices in the surface layer of the oceans and the lakes having their axes aligned within a few degrees along the wind direction in the presence of surface gravity waves. Because of their long-lived, significantly large-scale circulation within the ocean mixed layer, it is hypothesized that they contribute to the heat and momentum transfer in the mixing layer in oceans and lakes.
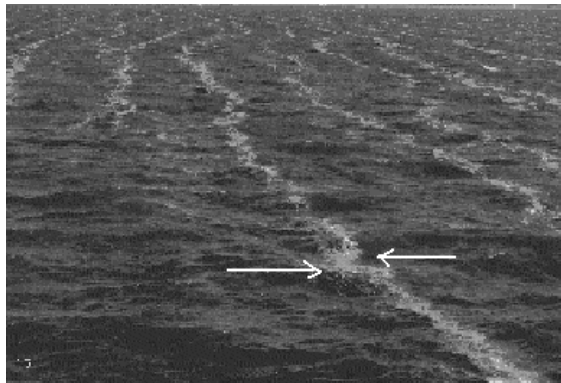
Figure 2.3   The collection of the bubbles into long and narrow streaks on the ocean surface

Langmuir (1938) showed that the collection of the seaweed, marine organisms, and foam from breaking waves or oil leakages into streaks, like those in Figure 2.3, is the visible evidence of counter rotating helical vortices near the surface. These features are known as Langmuir circulations after Dr. Irving Langmuir who was the first scientist to

study them and defined their properties without explaining the formation mechanisms. The most significant features of Langmuir circulations are lateral coherence and long life, which makes them different from eddies typical of turbulent flow.

The sketch in Figure 2.4 shows the basic structure of the Langmuir circulations as described by Langmuir (1938) and following investigators.
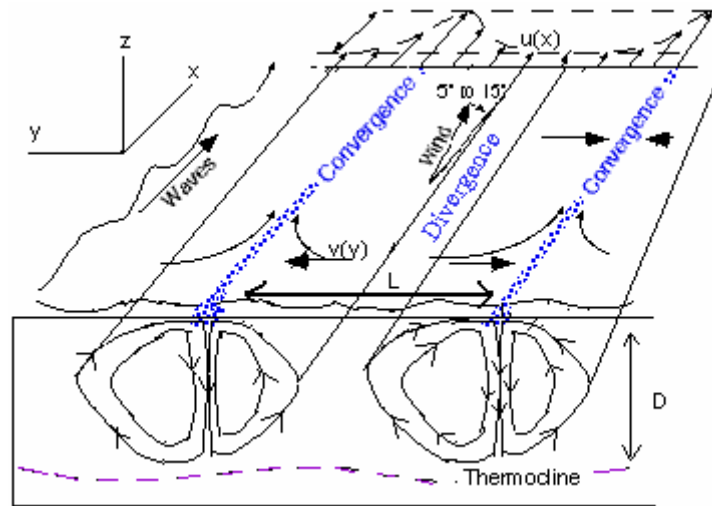
Figure 2.4   A schematic of forcing factors and structures of Langmuir circulations (From Smith 2001)

In Figure 2.4, L is the horizontal length in the crosswind direction between two convergence zones or two divergence zones, also known as row spacing. D is the vertical length scale or penetration depth, and is often limited by the pycnocline depth (Langmuir 1938). The common coordinate system used by most of the investigators is the wind-based coordinate system, which represents x in along wind direction, z in upward and y is cross wind direction. Velocity components u, v and w are in the directions of x, y and z respectively. Wind speed (U_w), generally defined 10 m above the water surface, is also an important parameter for the Langmuir circulations since wind is believed to be a main factor forming these circulations. Observations show that there is downwelling under the convergence zones and upwelling under the divergence zones. The u velocity component is maximum over the convergence zones and minimum over the divergence zones as shown in Figure 2.4.

14

1.   Formation Theories of Langmuir Circulations

There have been many theories proposed for the formation of Langmuir circulations where the observed features of the circulations are attempted to be described by physical models. However there is still not a theory, which can explain all the observed features exactly. The most commonly accepted theories are related to the wave-current interactions. A review of Langmuir circulation theories follows.

Thermal convection has been hypothesized to be main formation mechanism by several investigators following observations of collections of convective plumes into rows by the wind shear in the atmosphere (Pollard 1977). However, Langmuir (1938) advocated that the wind is the primary mechanism for the circulations, supported by observed circulations under stable or neutral conditions. Stommel (1951), Faller (1964), Csanady (1965), Ichye (1967) and Myer (1969) have all observed the Langmuir circulations in conditions of stable stratifications (Pollard 1977). Li and Garrett (1995) found that wave forcing dominates over the thermal convection for typical wind speed and surface cooling in driving Langmuir circulations. Since Langmuir circulations are observed under stable conditions, thermal convection cannot be considered as a primary formation mechanism, but may have secondary effects contributing to the primary mechanism. For example, under the surface cooling conditions, circulations may occur with less wind speed than the stable conditions, while stratification induced by strong surface heating may suppress the circulations generated by the wave forcing (Li and Garrett 1995).

Coupling of the ocean with the atmospheric rolls has also been considered as a forcing mechanism for the circulations. However the air moving with these rolls advects too quickly across the surface to couple with the water and has negligible effect on the water. Pollard (1977) cited that the observations of sea smoke above lakes made by Langmuir (1938) and Stommel (1951) support this conclusion. Leibovich (1983) also stated that the position of these rolls do not align with the windrow streaks above the Langmuir circulations.

Damping of the capillary waves in slicks occurs in the presence of surface films. Welander (1963) and Kraus (1967) proposed that the effects of these surface films might

be the main process, which create the Langmuir circulations. Welander (1963) hypothesized that smoothing the surface by damping the capillary waves in slicks would cause a higher wind speed, accelerating the water, then producing a secondary inflow into the slicks region. Leibovich (1983) discounted this suggestion since increasing wind speed is the result of the decreasing surface drag, and therefore the water speed in slicks would be smaller than the surrounding water, which is not observed. Kraus (1967) suggested another surface film related mechanism where energy is transferred from capillary waves into the slicks while they are being damped as they approach the slicks accelerating the slicks in the wind direction. Pollard (1977) argues that it is doubtful whether the capillary waves can supply energy fast enough to be sufficient for the observed rapid generation of Langmuir circulation. The energy budget given by Myer (1971) supports Pollard's argument since the total energy transfer from the capillary waves to the slicks is about   10 % of the rate needed to generate the circulations. Furthermore Leibovich (1983) stated that the formation of circulations in laboratory experiments exists in the absence of surface films.

Ekman layer instabilities may result as convective rolls with a small angle to the wind, and Faller (1964) suggested that these instabilities of Ekman spiral could be the driving mechanisms for Langmuir circulations. Leibovich (1983) stated that the growth rates of such instabilities are too small to account for Langmuir circulations. Gammelsrod (1975) enhanced the Faller (1964) idea by starting with a steady along wind shear flow, which is the result of the balance between Coriolis force and friction. The vertical advection of the mean shear by vertical perturbation velocity will accelerate the along wind perturbation flow and then the resultant along wind velocities will be turned to the cross wind direction by the Coriolis force. As a result, the Langmuir like cellular structures will occur due to the new cross wind shear flow. Gammelsrod's theory predicts the cell orientation at an angle to the vertical and along wind velocities at the surface to be zero, which are the main differences from the observed vertical Langmuir cells. Furthermore, the Coriolis force acting on the along wind perturbation velocities is not balanced by friction and remain long enough to create the crosswind velocities. This is not realistic, because the friction is created by small-scale turbulence via Reynolds stresses and this feature is displaced vertically by itself and the friction term will continue

16

to balance the Coriolis force on the perturbation horizontal velocities preventing the growth of crosswind velocities (Pollard 1977).

Theories based on wind forcing mechanisms in the presence of surface gravity waves are the most consistent with the observations. All the experimental studies including Langmuir's own indicate that the wind is the primary driving mechanism for the Langmuir circulations. However, the question of how the wind sets up these circulations is still not clear. The wind-based theories can be generalized as waves and wind drift current interaction theories. Craik and Leibovich (1976) and Garrett (1976) are two leading studies that propose the most accepted wave and current interaction theories. Both theories assume a nearly irrotational wave field and a much weaker rotational current in upper layer, with the nonlinear interactions between the waves and currents forming Langmuir circulations. The mechanism of how the interactions create the circulations is expressed differently in these two theories.
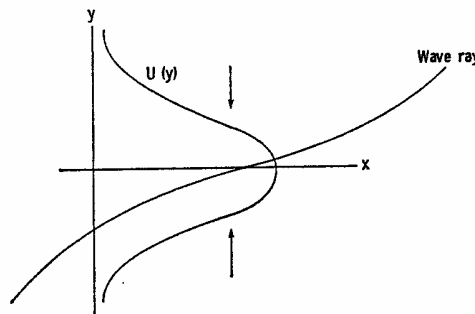
Figure 2.5   Refraction of a wave ray by a current U (y). The arrows indicate the lateral forces exerted by the wave (From Garrett 1976)

Garrett (1976) related Langmuir circulations to the refraction of the surface waves by the mean current anomaly, which is in the direction of the winds. Figure 2.5 illustrates the refraction of the waves by the mean current jet U(y). The first mechanism of this refraction is the lateral forces that tend to produce an inflow towards the maximum downwind current. The wave speed perpendicular the mean current will decrease in the current zone and then increase out of the current zone, so there must be a momentum transfer between the waves and currents to accomplish this action, and the lateral forces are the result of this momentum transfer. In Figure 2.6, the arrows indicate the forces exerted by waves propagating in positive x-y directions. Garrett showed that the force is

17

predominantly towards the current maximum for waves at a small angle to the x-axis. The inflow produced by dominant lateral forces creates along wind vorticity, which is the signature of Langmuir circulations.
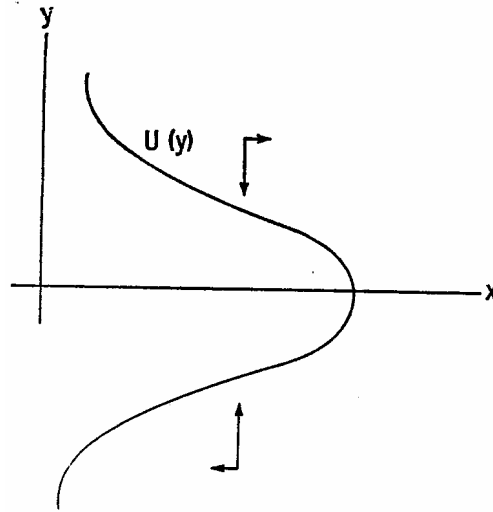
Figure 2.6   Lateral forces produced by refraction of the waves (From Garrett 1976)

Enhanced wave breaking is the second consequence of the wave refraction effect. (Garrett 1976). The wave amplitude will increase as the wave speed is decreasing in the high current zone and this will increase the wave breaking in that region resulting the momentum transfer from the waves to the currents which will reinforce U(y). The momentum transfer in the y-direction is canceled since the wave spectrum is assumed to be symmetric about the downwind direction (Garrett 1976). Enhanced U(y) creates a feedback for the first mechanism, thus the combination of two mechanisms produces an instability mechanism, which forces the Langmuir circulations.

Figure 2.7 shows that the vortex line of z-vorticity is tilted towards the downwind direction by the Stokes drift of the waves. According to the Garret's theory, the z-vorticity with a vertical vortex line is created by the wave dissipation in the y direction and the vortex line is bent in the x direction by the x-component of the Stokes drift. Finally the cellular motion will be about this new x-oriented vortex line creating the x-vorticity as a signal of the Langmuir circulations.

18
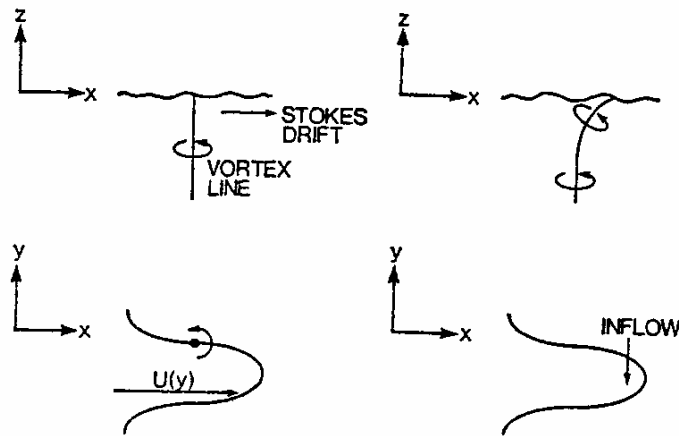
Figure 2.7   The z- vorticity becomes x- voticity due to tilting of the z- oriented vortex line towards the direction of maximum U(y) by the Stokes drift (From Garrett 1976)

Garrett (1976) also stated the basic limitations of his theory. The internal reflection of the waves by the current is neglected. For the small wave angles to the current zone used in the theory, it has been found that the weak currents can internally reflect the waves which creates the inflow towards the line of reflection instead of maximum U(y) region. Although, the convergence zone exists in a different place than Garrett (1976) explained previously, Garrett (1976) asserts that lateral forces are still exerted by the reflected waves and the feedback mechanism for the instability remains the same. The assumption of slow variation of U(y) was stated as another limitation. The wave modification by the currents is mathematically and physically explained by assuming mean steady flow while the mean flow is being enhanced in time, and there seems to be a contradiction between the assumption and the application. Although Garrett (1976) explained this inconsistency as a limitation, he mentioned that the developing time scale of the mean flow is much slower than the set up time scale of the Langmuir circulations by the wave packet. Another possible limitation given by Garrett (1976) is the constant surface currents over the depth of waves and he emphasized that even though the current is not uniform over this depth; the interaction stresses exerted by the waves will still cause the vertical shear.

Leibovich (1983) stated that the modification of the wave field by the horizontal current and the preferential wave breaking are doubtful theoretically and experimentally. Leibovich (1983) claimed that WKBJ theory used by Garrett to explain the amplification

of the waves and may lead to wrong conclusions. Leibovich (1983) cited that Smith (1980) was unable to find amplification of the waves predicted by Garrett's (1976) model without WKBJ theory. Leibovich (1983) also cited the experimental studies done by Thorpe and Hall (1980) and Kenney (1977), and these experimental studies found the wave breaking between streaks and in them with equal frequency instead of dominantly on the line of convergence.

Pollard (1977) suggested that Garrett's theory is plausible since it can qualitatively explain all observed features but he criticized the mathematics of this theory in terms of the same aspects as Leibovich (1983)

The other important theory related to the wave and current interactions is the Craik and Leibovich (CL) (1976) theory. Craik and Leibovich (1976) defined the common qualitative observed features of the circulations that a theory should be able to explain:

CL (1) A parallel system of vortices aligned with the wind must be predicted.

CL (2) A means must be given by which these vortices are driven by the wind.

CL (3) The resulting cells must have the possibility of an asymmetric structure with downwelling speeds larger than the upwelling speeds.

CL (4) Downwelling must be below where the wind directed surface current is greatest

CL (5) The Langmuir circulations must have maximum downwelling speeds comparable to the mean wind directed surface currents.

There are two distinct versions of CL theories. The first one, CL-1, was developed by Craik and Leibovich (1976) and the second one, CL-2, was first proposed by Craik (1977) and then explored by Leibovich (1977a-1977b). Both versions depend upon the discussion of the "Vortex Force", which is the cross product of Stokes drift and the mean vorticity,

$$f = u_s \times \omega \tag{2.35}$$

20

where ω is the mean vorticity and u_s is the Stokes drift of surface waves. According to the small amplitude sinusoidal wave theory, water particles move in closed circular orbits, and there is no net motion of the water mass. However in real water waves of finite amplitude, the orbits are not closed, therefore there is a small amount of net motion of water mass in the wave traveling direction. This is called Stokes drift and Philips (1977) defined the Stokes drift as $u_s = \left\langle \int^t u_w \, dt . \nabla u_w \right\rangle$ where brackets represent the temporal mean, u_w is the orbital velocity of the water mass. Basically, CL theories are based on the restoring of the mean vorticity by surface wave Stokes drift via vortex force.

Craik and Leibovich (1976) introduced the CL-1 theory by evolving the previously developed equations by Craik (1970) and Leibovich and Ulrich (1972). The initial assumptions are the coverage of the surface by short crested wind generated irrotational gravity waves, which have a discrete directional frequency spectrum with two peaks at an equal angle θ in both sides of the wind direction (monochromatic bimodal wave), infinite depth, constant eddy viscosity to represents the turbulence effects, and a wave spatial structure that remains coherent for Stokes drift averaging. Craik and Leibovich (1976) explained the Stokes drift is periodic in the y direction (cross-wind direction) for the monochromatic bimodal wave assumption.
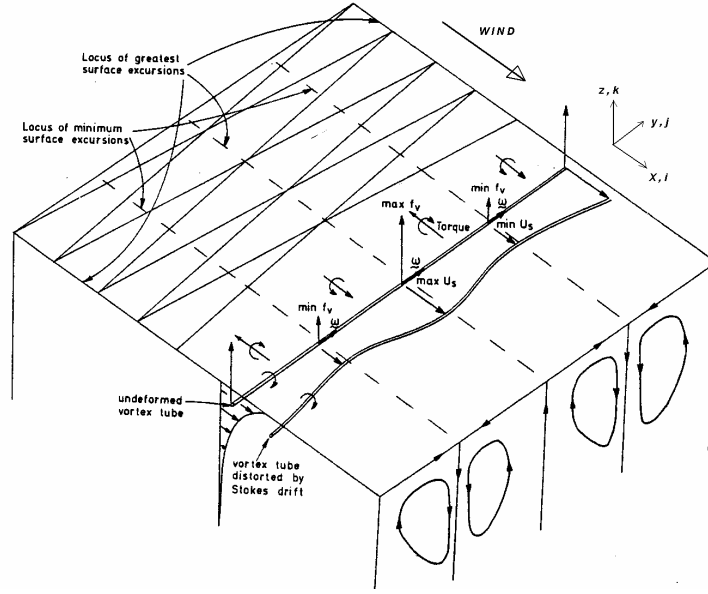
Figure 2.8   CL – 1 instability mechanism creating Langmuir circulations. f_v is the vortex force, ω is y-vorticity, and U_s is the Stokes drift in the x-direction. The coordinate system is the wind-based coordinate system with the positive x-axis towards the wind direction. (From Leibovich 1983)

Leibovich (1983) illustrated the CL-1 mechanism (Figure 2.8). The coordinate system in Figure 2.8 is the wind-based coordinate system. When the wind blows in a fixed direction, the initial wave field will have a unidirectional Stokes drift in the same direction as the wind. This initial Stokes drift is $u_s = U_s i$, where U_s is the total Stokes drift magnitude (Leibovich 1983). The momentum transfer from the wind to the water dictates the horizontal velocity in the same direction with the wind. Horizontally averaged velocity is defined as $u = U(z,t) i$ with positive y-vorticity $\omega = (\partial U / \partial z) j$ by neglecting the Coriolis force (Leibovich 1983). The cross product between the Stokes drift and the y-vorticity using Equation 2.35 will give an upward vortex force.

$$f_v = kU_s (\partial U / \partial z) \qquad (2.36)$$

Leibovich (1983) explained that this vortex force is analogous to the buoyancy force, and if the horizontal velocity is only a function of depth, the vortex force will be balanced by the hydrostatic pressure gradient, which produces unidirectional current. After the characteristic of initial wave field turns into the assumed wave field, the Stokes

drift will be periodic in the y-direction. The total Stokes drift, periodic in y-direction is given by Craik and Leibovich (1976) in Equation 2.37.

$$u_s = 2ke^{2z}\left[1 + k^2 \cos 2ly\right] \tag{2.37}$$

Where $k = \cos\theta$ and $l = \sin\theta$ are the wave numbers in x- and y-directions respectively. θ is the angle between the wind direction and the crests of the bimodal short-crested surface gravity waves on each side of the wind. Since the Stokes drift will vary in the y-direction, the upward vortex force will not be balanced by the hydrostatic pressure gradient anymore and will also change in the y-direction as a result of rectified Stokes drift. The variations of the upward vortex force in the y-direction will produce overturning about the x-axis. In Figure 2.8, the Stokes drift u_s at the wave crests is higher than the Stokes drift between the wave crests, and the upward vortex force is maximum and minimum at the same places where the Stokes drift is maximum and minimum respectively. The variation of the upward vortex force in the y-direction produces two circular counter-rotating rolls converging at the surface between the wave crests. These two counter-rotating circular motions are the Langmuir circulations as described by the CL-1 theory.

Craik and Leibovich (1976) reported that their model results qualitatively matched with the observed circulation characteristics. Nevertheless, for realistic wind speeds and the wave slopes, Craik and Leibovich (1976) were forced to admit that their model failed to satisfy requirement CL (3). Pollard (1977) noted that the CL-1 model forecasts upwelling regions where the Stokes drift is largest, which is inconsistent with observations. Pollard (1977) also emphasized that such a Stokes drift pattern as explained in the CL-1 theory requires that variances in the y-direction should remain fixed in space for a long enough time to produce Langmuir circulations, and crossed wave pairs should be phase locked for several wave periods to achieve this. This type of phase locking is not expected in a wind-generated sea, although it can be generated in laboratory experiments (Leibovich 1983).

It is generally accepted that the assumptions of time independent currents, crossed waves and invariance of rectified motion in the x-direction are the weakest points of the

23

CL-1 theory. Leibovich (1977a) modified the theory to include time evolution of the wind-directed currents and circulations under the assumption that the wave field was symmetric with respect to the x-axis and invariant in the x-direction. This assumption made the motion independent of x, and the formulation of the phenomena was explained as an initial value problem where the currents and circulations were initially zero. The dimensionless Langmuir number, *La*, was derived by Leibovich (1977a) to represent the initial value problem.

$$La = \left(v_T^3 k^2 / \sigma a^2 u_*^2 \right)^{1/2} \tag{2.38}$$

In this expression, v_T is the eddy viscosity, σ is the surface waves frequency, u_* is the friction velocity for constant wind stress when $t \geq 0$, k is the wave number, and a is the wave amplitude. The Langmuir number, which is the simply the inverse of the Reynolds number, physically expresses the balance between the rate of diffusion and the rate of production of stream-wise vorticity (Leibovich 1983).

Leibovich (1977a) also assumed infinite depth, constant eddy viscosity, constant density, and that the Stokes drift was produced by a pair of uniform, narrow-banded wave trains propagating at equal and opposite angles with respect to the wind direction. Leibovich (1977a) used the Langmuir number to define the scales of Langmuir circulations, as shown in Table 1.

Length	Time (T_d)	Wind-directed component of rectified current	Crosswind velocity component of rectified currents
k^{-1}	$\left(v_T / \sigma \right)^{1/2} / a k u_*$	$u_*^2 / v_T k$	$\left(a u_* / v_T \right)\left(\sigma v_T \right)^{1/2}$

Table 1.   Scales of Langmuir circulations defined by Leibovich (1976a) (From Leibovich 1983)

The improved version of the CL-1 mechanism by Leibovich (1977a) satisfies the listed features CL (1) through CL (5) and matches observed results better than its

predecessor. In the revised model, the maximum surface sweeping speeds are close to the maximum downwelling speeds, and the maximum downwelling speeds range from slightly less than twice to more than seven times the maximum upwelling speeds. The maximum along-wind current anomaly is found over the downwelling zones with a speed approximately 55-75 % greater than the speeds midway between zones. (Leibovich 1983).

Craik (1977) first introduced the second version of the CL theory (CL-2) for a constant density system. Leibovich (1977b) adapted the theory to include density stratifications under the Boussinesq approximation. The time-dependent development of the waves by the wind is neglected in CL-2 theory, and both momentum and thermal eddy diffusivities are assumed to be constant. It is necessary to have a non-coherent surface wave structure (Leibovich 1983). The vortex force is again the reason for the circulations, but the CL-2 mechanism producing the vortex force is different from that used by the CL-1 theory. Leibovich (1983) illustrates both the dynamics and kinematics of the CL-2 mechanism, as shown in Figure 2.9.
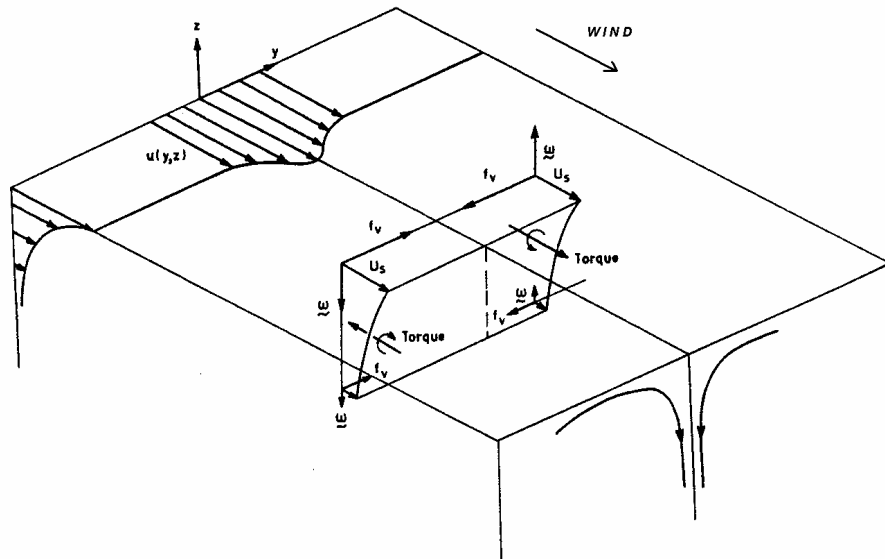
Figure 2.9   CL-2 instability mechanism of Langmuir circulation generation. f_v is the vortex force, ω is the z-vorticity, and U_s is the Stokes drift in the x-direction The coordinate system is the wind-based coordinate system with the positive x-axis towards the wind direction. (From Leibovich 1983)

25

Stokes drift is defined as $u_s = U_s(z)i$ if the waves lack a coherent spatial structure. Decreasing U_s and U with depth will lead to decreasing vortex force with depth, and combined results of such a distribution of U_s and U are similar to those obtained with a statically unstable density distribution (Leibovich 1983). If dissipation is weak enough, the current is unstable. Horizontal uniform current $U(z)$ is unidirectional in the wind direction, because the vortex force in Equation 2.35 is balanced by a pressure gradient force in the absence of the disturbances in the y-direction, as assumed in CL-1 theory. The vertical vorticity ω_z is produced by the irregularities, $u(y,z,t)$, in the largely horizontally uniform current $U(z)$. Equation 2.5 becomes $\omega_z = -(\partial u / \partial y)k$ (where k is the unit vertical vector). The vortex force per unit mass is then defined as in Equation 2.39.

$$f_v = -U_s \omega_z j \qquad\qquad 2.39$$

If the z-vorticity ω_z is positive (upward), vortex force will be in the negative y-direction, and if z-vorticity ω_z is negative (downward), vortex force will be in the positive y-direction. In both cases the water mass accelerates towards the maximum current anomaly, so convergence zones will be created in this region. Because of the conservation of mass, water at the convergence zones will sink, and the sinking water will be replaced by the horizontally converging flow. This increases the magnitude of the convergent jet due to the vortex force. In summary, the rotation and stretching of the vertical vorticity by Stokes drift results in convergence and amplification of the surface current anomaly. This instability process is the basis of CL-2 theory and creates the Langmuir cells.

Leibovich (1977b) estimated the instability, *M(z)*, of the system condition for an inviscid stratified fluid in infinite depth.

$$M(z) = U_s'(z)U'(z) - N^2(z) \qquad\qquad (2.40)$$

The instability occurs when $M(z)$ is positive and does not occur when $M(z)$ is negative. $N^2(z)$ is the Brunt-Vaisala, or buoyancy, frequency of the initial state as

described in Equation 2.2. However, it can be also formulated in terms of thermal expansion as $\beta g \overline{T}^{'}(z)$, where β is the thermal expansion coefficient and $\overline{T}^{'}(z)$ is the vertical gradient of temperature distribution. $U_s^{'}$ is the vertical gradient of the Stokes drift and $U^{'}$ is the vertical gradient of the shear currents. $M(z)$ is maximum at the surface $(z = 0)$. Leibovich (1977b) defined the maximum growth rate σ_{max} of the circulations for unstable system conditions with infinitesimal wavelengths as

$$\sigma_{max} = \sqrt{M(0)} \tag{2.41}$$

When the instability of the system occurs with stable density stratification, there will be a depth below which the disturbances will not penetrate. Leibovich (1983) expressed the instability condition in terms of the Richardson number, Ri.

$$Ri = \min\left[N^2/U^{'}(z)U_s^{'}(z)\right] \leq 1 \tag{2.42}$$

Leibovich (1983) cited the studies Leibovich and Paolucci (1980a, b, 1981) and Leibovich and LeLe (1982), which have explored the CL-2 mechanism with nonzero eddy diffusivities. Constant positive N^2 and a time-dependent unidirectional current solution of the equations of motion were considered in Leibovich (1977b) for infinitely deep water and constant surface stress at $t = 0$. Leibovich and Paolucci (1980a) found that the small-scale, very weak disturbances grew in strength while they cascaded to larger scales unless the domain size prevented them from growing. Leibovich and Paolucci (1981) calculated the linear stability limits for two-dimensional rolls in terms of Richardson number, inverse Langmuir Number and length scale (Table 2).

Ri	La_c^{-1}	k_c
0.00	1.52	0.32
0.10	1.58	0.31
0.25	1.66	0.30

Table 2.   Critical inverse Langmuir number (La_c^{-1}) and critical wave number (k_c) of linear theory at various Richardson numbers (Ri) defined by Leibovich and Paolucci (1981) (From Leibovich 1983)

Leibovich and Paolucci (1980a) expressed the Richardson number in Table 2 with Equation 2.43 for a temperature-stratified ocean

$$Ri = \beta g \overline{T}' \Big/ \Big[\left(a u_* k \right)^2 \sigma / \upsilon_T \Big]$$
(2.43)

where k is the dominant wave number. The convective motions mix the upper layers and form a layer of strong temperature gradient. After correcting several errors in the work of Leibovich and Paolucci (1980a), Leibovich and LeLe (1982) found smaller penetration depth of Langmuir circulations. They also found that preexisting thermoclines act like a strong obstacle, which prevent convective motions from deeper penetrations (Leibovich 1983).

Leibovich (1983) recommended that both CL theories be tested for conditions in which waves and currents exist in the absence of the wind, such that u_s is not parallel to the horizontally averaged current U. The CL theories suggest that an instability will occur whenever $u_s U \geq 0$, whether this results in Langmuir circulations or not. Leibovich (1983) also noted that the CL theory of Langmuir circulations in two dimensions is analogous to the double diffusive convection problems mathematically, but Leibovich and Tandon (1992) stated that this is not true for CL theory in three dimensions.

Craik (1982a) proved that water waves induce the weak viscous Eulerian current by the instability of CL-2 theory in the absence of wind, and noted that this may be the same case for the currents induced by internal waves near a density interface. Leibovich (1983) cited this study as one to be explored in terms of the CL theories.

After reviewing previous analysis, numerical models, laboratory simulations, and filed work, Smith (2001) concluded that the CL-2 mechanism is the dominant factor in Langmuir circulations.

2. Field and Laboratory Observations of Langmuir Circulations

Basic features of Langmuir circulations examined in either field or laboratory studies are windrow spacing, vertical velocities below the convergence and divergence zones, surface velocities, depth of penetration, formation times after wind speed reaches the significant velocity, realignment time after the wind speed shift, and angle between the surface streaks and the wind direction. In addition to these observed features of the circulations, most field experiments measure wind speed, water temperature, and water density data to relate the observed features to the wind forcing, thermal forcing and density structures respectively. The threshold wind speed to initiate the circulations is commonly reported as 3 ms^{-1} (Leibovich 1983). Myer (1971) observed that circulations were likely to occur at lower wind speeds in thermally unstable conditions than would be required in stable conditions.

a. Streak Spacing

Langmuir (1938) explained the difficulties of defining the distance between surface streaks because of the occurrence of numerous smaller streaks between the well-defined larger streaks. The larger surface vortices contain smaller and shallower vortices in the same way large waves have smaller waves upon them (Langmuir 1938). Langmuir (1938) reported the spacing in Lake George to be between 5 to 25 m and changing seasonally depending upon the thermocline depth, and also reported the spacing in the North Atlantic from 100-200 m. Leibovich (1983) explained that the row spacing in the ocean is greater than in lakes and ranges from two to hundreds of meters. He also cited some studies such as Assaf et al (1971), Williams (1965), Ichiye (1967), Scott et al (1969), Myer (1969, 1971), and Harris and Lott (1973), which showed a dynamical cascade from smaller scales towards dominant larger scales.

Langmuir (1938) and the most of the following studies related the spacing (L) to the penetration depth of the circulations or mixing layer depth (D). Langmuir (1938) suggested that the circulations penetrate down to the bottom of the thermocline, which is deeper in the fall than in the spring and early summer, and found larger spacing during the times when the thermocline was deeper. Assaf et al (1971) found spacing of the largest streak scales to be 280 m, with a mixed layer depth of 200 m, which shows

that $L/D = 1.4$ and Maratos (1971) reported $L/D = 1.66$. Smith (1992) found that the spacing was 2 to 3 times the mixed layer depth while it varied from 40-60 m due to the baroclinic tide modulation of mixed layer depth. Smith (1992) also found that the circulations deepened the mixed layer.

Faller and Caponi (1978) reported that L / H = 4.8 [1-exp (-0.5 L_w / H)] during their laboratory experiments, where H is the mean depth of the water in the wind-wave tank or estimated mixed layer depth for oceanic data, L is the spacing between convergence zones, and L_w is the wavelength of the surface waves. Their laboratory results and several sets of oceanic data fit this equation. They noted that the circulations begin within seconds after arrival of the waves and concluded that the scale of the surface waves is important in forcing the circulations.

Uzaki and Matsunaga (2000) examined the Langmuir circulations in a laboratory wind-wave tank. The depth of the tank was varied from 2 cm to 16 cm. They observed that the spacing depend upon the water depth rather than the wave parameters and wind speed, and reported the spacing 2.5 times the water depth in a shallow water region. Faller and Woodcock (1964) related the mean spacing to the wind speed and found that L = (4.8 s) x U_w, where U_w is the wind speed 10 m above the sea surface. Maratos (1971) reported a similar relationship with L = 0.1 m + (4.8 s) x U_w. Leibovich (1983) stated that the number of samples and the range of wind speed used in these experiments were small and these relationships may not be accurate. Scott et al (1969) attempted to find a similar relationship but could not find a statistically significant correlation between spacing and wind speed.

b. Orientation

The orientation of the streaks was generally observed with the axis nearly aligned with the wind direction. Different studies reported different orientation angles between the wind and the streaks. Leibovich (1983) noted that the windrows were nearly aligned with wind direction with a maximum deviation of 20°. Langmuir (1938), Walther (1967), Kenny (1977) found that windrows were aligned within a few degrees of the wind direction in their experiments in the lakes, and the same result was found by Williams (1965), Welander (1963), and Maratos (1971) in the ocean.

Faller (1964) looked for a systematic deviation from the wind direction and analyzed oceanic data from the Northern Hemisphere, finding consistent deflection of $13^o \pm 2^o$ to the right of the wind direction.

Leibovich and A. Tandon (1993) found that the small windrow angles were due to weak density stratifications. The largest angle that they found was 5.3 degrees with an equal likelihood of being on either side of the wind direction. They reported that the speed of the lateral drift associated with the angular deviation increases with increasing stratification strength.

c.   Formation Times

Pollard (1977) indicated that Langmuir circulations appear within a few tens of minutes after the onset of winds having speeds larger than 3 ms^{-1}. The reorientation time of the circulations after the wind direction shift was studied by several scientists. Maratos (1971) observed that Langmuir circulations reoriented with the new wind direction within 2 to 4 minutes after the rapid shift of wind direction. Langmuir (1938) noted that the reorientation time was within 20 minutes after a wind direction shift in Atlantic Ocean. Welander (1963) observed that 8-m spaced rows reoriented within 10 minutes after the wind shift, and the reoriented rows had the same spacing as the previous ones. Stommel (1951) found the smallest reorientation time, and reported that small-scale windrows on ponds reoriented within 1 –2 minutes after the wind shift. Faller (1981) suggested that small scale Langmuir circulations have more rapid responses to wind shifts than larger scale Langmuir circulations.

d.   Strength and Persistence

Plueddemann et al (1996) related Langmuir circulations' strength to wind speed and Stokes drift and formulated the strength as $\left(u_* U_s\right)^{1/2}$, where $u_* = \left(\tau/\rho\right)^{1/2}$ is the water friction velocity and U_s is the Stokes drift velocity. They also observed that the Langmuir circulations were maintained for up to 24 hours after the wind relaxation and hypothesized that the waves were responsible for this persistence, because the waves had much slower relaxation time than the winds during their observations.

e. *Surface and Subsurface Current Structure*

Surface current structures associated with Langmuir circulations were determined from the collecting time of the surface tracers into rows, and the vertical velocities were determined from the sinking motions of the surface particles until the 1980s. Smith (2001) noted that the velocity components of the Langmuir circulations had started to be estimated using the Doppler shift of the backscattering sound signals in the late 1980s.

Leibovich (1983) reported that the along-wind horizontal velocity component measured at streaks was larger than those between them. Ichiye (1967) reported that along-wind velocities at streaks were two times larger than the along-wind velocities between the streaks. 10 cms^{-1} and 6 cms^{-1} differences were reported by Assaf et al (1971) and Harris and Lott (1973) respectively, but Leibovich (1983) stated that these results were reported without reference to other components of the current system or prevailing wind speed.

Langmuir (1938) reported average cross wind horizontal velocities at the surface of 3 cms^{-1}, while Woodcock (1944) and Ichiye (1967) reported approximately 6 cms^{-1} and 5 cms^{-1} respectively. Plueddemann et al (1996) related the crosswind surface velocities to the wind speed and waves, and parameterized with $(WU_s)^{1/2}$ where W is wind speed. Smith (1996) parameterized the same relation with $(W^2U_s)^{1/3}$. Both parameterizations were made for the initial growth of the Langmuir circulations. However Smith (2001) examined the data from MBLEX-1 (marine boundary layer experiment) and noted that wind speed contribution to the scaling vanished after Langmuir circulations had developed, and described the scaling as $v \sim U_s$. Smith (2001) also investigated if this scaling was valid for other data sets and applied this scaling to the SWAPP (Surface Waves Process Program) data. He found that the relationship between cross wind surface velocities, wind speed, and Stokes drift was still statistically significant but correlations were not as strong as the MBLEX-1 data.

Langmuir (1938) reported downwelling vertical velocities of 2 to 3 cms^{-1} below the surface streaks, and upwelling vertical velocities below the midway adjacent streaks were 1 to 1.5 cms^{-1}. Myer (1969, 1971) found the downwelling velocities 3 cms^{-1}

under thermally stable conditions and 5 cms^{-1} under thermally unstable conditions. Leibovich (1983) described maximum downwelling velocities as roughly one percent of the wind speed or one third to one quarter of maximum wind-induced surface currents.

Sutcliffe et al (1963) correlated the downwelling velocities with wind speed and found that w = 0.85 x 10^{-2} W or 1 cms^{-1} per 1 ms^{-1} wind, where W is wind speed and w is downwelling velocity.
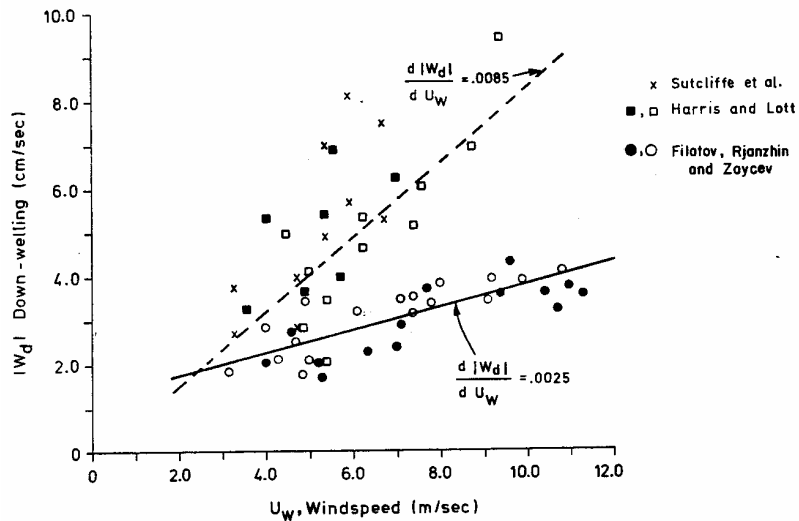
Figure 2.10   Measured downwelling speeds below streaks as a function of wind speed. The open squares and circles correspond to surface heating, closed symbols to surface cooling. The dashed line is a least square linear fit to all of the Sutcliffe et al (1963) and Harris and Lott (1973) data taken together while the solid line is the corresponding fit to all of the Filatov et al (1981) data (From Leibovich 1983).

Leibovich (1983) correlated the vertical down wind velocities with the wind speed by using the data collected by Harris and Lott (1973), Filatov et al (1981), and Sutcliffe (1963) and produced the correlation plot in Figure 2.10 and concluded that downwelling velocity increases linearly with increasing wind speed.

Smith et al (1987.) found that the vertical velocities range from 15 to 30 cms^{-1} in 15 ms^{-1} winds or about 1 or 2 % of wind speed.

THIS PAGE INTENTIONALLY LEFT BLANK

III. SITE DESCRIPTION AND DATA COLLECTION

A broadband acoustic Doppler current profiler (BADCP) was used to measure velocity profiles across the water column during the Coupled Boundary Layers Air Sea Transfer (CBLAST) project. Data were collected in 2003 between year day 228 and 360. The BADCP was cabled to the Air Sea Interaction Tower (ASIT), which provided power and sent a continuous data stream to a data logging computer at the Martha's Vineyard Coastal Observatory (MVCO).

A. THE COUPLED BOUNDARY LAYERS AIR SEA TRANSFER (CBLAST)

The coupled boundary layers air-Sea transfer (CBLAST) project focuses on processes that occur in the oceanic and atmospheric surface boundary layers, which are regions influenced by ocean surface waves. This research was sponsored by the Office of Naval Research (ONR) to develop improved parameterizations to be used in high-resolution coupled air-ocean regional numerical models.
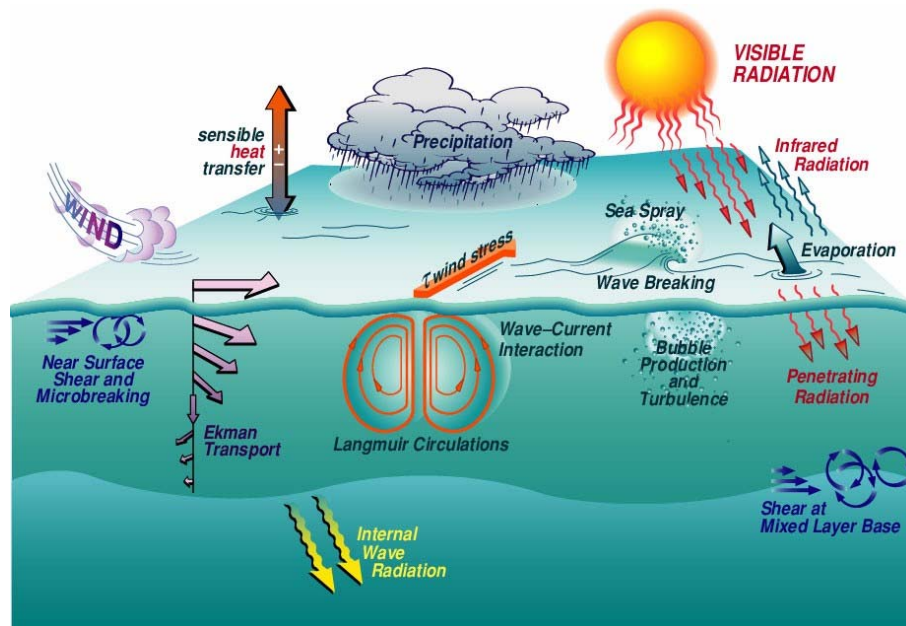
Figure 3.1   The Physical Processes in the atmospheric and oceanic boundary layers examined in CBLAST (From www.whoi.edu)

CBLAST investigated the processes that couple momentum, mass, and heat across the turbulent atmospheric and oceanic boundary layers in the presence of surface gravity waves. The main objectives of CBLAST were to understand the influence of surface waves in air-ocean coupling and determining the 3-D structures of these boundary layers, and to improve the understanding of air-sea interactions in low to moderate winds.

Figure 3.1 summarizes processes studied in the CBLAST project. CBLAST had both observational and modeling components. The observational measurement tools are fixed towers and moorings, satellite and airborne remote sensing, autonomous under water vehicle (AUV), research vessels and aircraft. The *in situ* observations included oceanic and atmospheric turbulence and mean flow from the fixed towers and moorings, 2-D and 3-D structure of the boundary layers, 2D ocean surface structure from the remote sensing measurements, and surface wave measurements with a special emphasis on small scale and wave breaking. All the observational investigations will help quantify the turbulent kinetic energy (TKE) momentum, mass and heat budgets in the oceanic mixed layer and atmospheric boundary layer in a hierarchy of large eddy simulation (LES) and regional coupled atmosphere / ocean models.

1.   Air Sea Interaction Tower (ASIT)

The ASIT (Figure 3.2) was built to meet some of the observational requirements for CBLAST. ASIT was instrumented from top to bottom with sensors capable of measuring momentum, heat and mass exchange between the atmosphere and the ocean. The tower structure was designed by Appledore Engineering Inc. and constructed by RDA Construction Corporation under the direction of Dr. Tim Edson at WHOI, and was funded by ONR. It was specifically designed to make the measurements in the ocean and the atmosphere to investigate the ocean processes, which include air-sea interactions, gas exchange, ocean mixing, bio-optics and sediment transport.
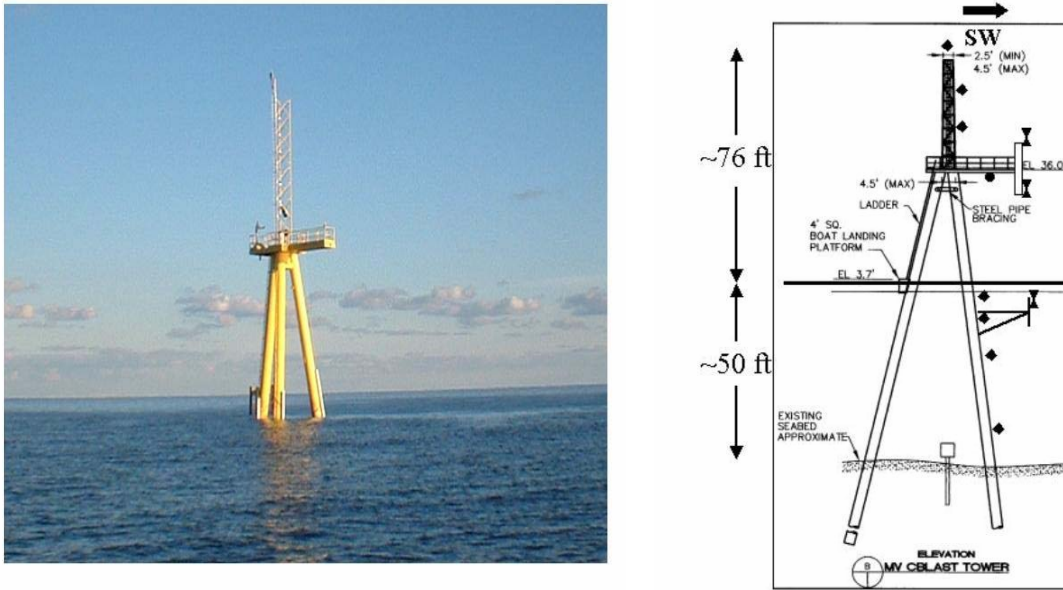
Figure 3.2   Air Sea Interaction Tower (From www.whoi.edu)

       The ASIT is located 3.5 km. due south of MVCO (Figure 3.3) in 16.5 m. water and extends 25 m. above the water line into the marine boundary layer. It is connected to Martha's Vineyard coastal observatory (MVCO) by a hybrid fiber optic data and power cable. Routine data measured by ASIT are integrated with MVCO data, and the integrated data time series includes wind speed and wind direction, tidal heights, air and sea temperature, off shore bottom and surface currents, and wave directional spectra. The ASIT location is $41^o\ 19.5'\ N\quad 70^o\ 34.0'\ W$ and marked with the letter C in Figure 3.3.
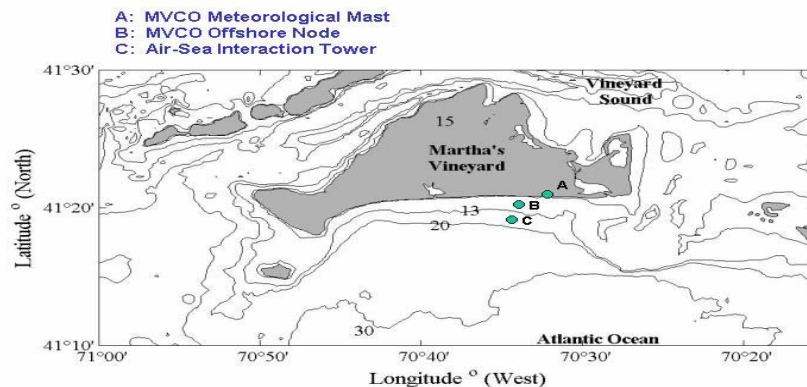
Figure 3.3   Martha's Vineyard with gray color and ASIT Location marked with 'C' symbol 3.5 km south of Martha's Vineyard (From www.whoi.edu)

37

The BADCP used in this study was deployed by Res. Prof. T. P. Stanton as a component of his ocean measurements for CBLAST.
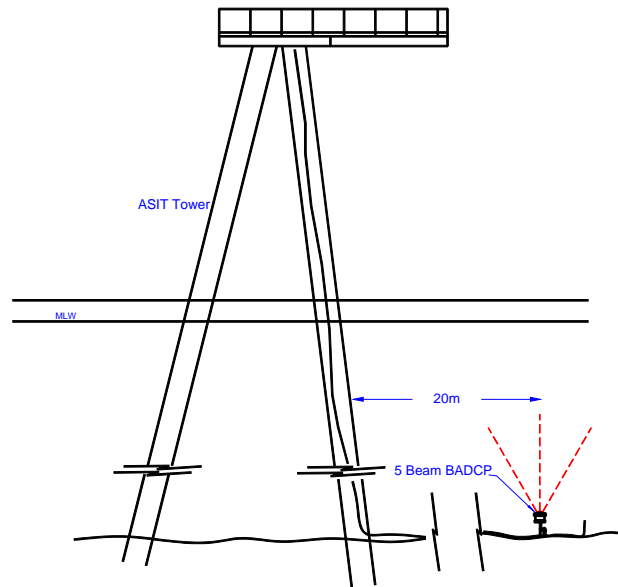
Figure 3.4   BADCP and ASIT orientation at the ocean bottom. The distance between ASIT and the BADCP is about 20m and there is data node between the ASIT and BADCP

The NPS 5-beam BADCP was deployed offshore 20 meters south of ASIT from a pipe jetted into the seabed, looking upward to the water surface (Figure 3.4). The distance between the BADCP and the seabed was about 1.5 m and the first bin was 1 m above the transducer. The BADCP was connected to an underwater data node, which provided communication to the shore-based Linux data-logging computer through the ASIT ethernet system. The ~0.5 Hz sampled profile data was acquired by a C-program running on the shore computer at the MVCO shore lab, and the data files were routinely transferred back to NPS for processing and analysis. The local data logging removed dependence on the T1 data link from MVCO to the mainland.

B.   BROADBAND ACOUSTIC DOPPLER CURRENT PROFILER (BADCP)

The custom-built 5-beam BADCP manufactured by RD Instruments transmits acoustic pulses from five individual transducers along five individual beams, and the transducers receive the sound backscattered from the zooplankton and small particles such as bubbles floating with the water currents. By comparing the frequency of

transmitted and received sound signals, the BADCP measures the velocity profiles along the beams at each depth cell by using the Doppler shift principle.
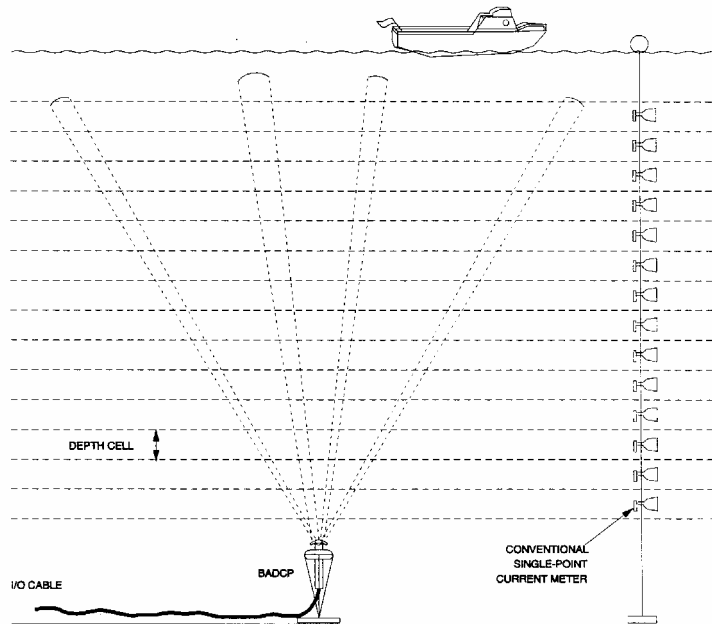
Figure 3.5   Typical BADCP profiling technique that allows collecting the data at different depth cells (bins) along five beams. Depth cells represent conventional single-point current meters (From RDI BADCP technical manual)

The depth cell shown in Figure 3.5 is the vertical length of each cell or bin where the velocities are measured. Depth cells or bins represent the conventional single point current meters that are deployed in different depths throughout the water column. The BADCP not only collects the velocity data, but also calculates the echo intensity of the backscattered sound signals and the correlation magnitudes at each bin. Echo intensity is useful in determining signal strength and the relative volume of the particles backscattering the sound signal to the transducers, and can be used to check data quality too. Correlation magnitudes are the measure of the pulse-to-pulse correlation in a ping for each bin, and represent the validity or confidence of the data.

Broadband ADCPs transmit a series of short pulses instead of one long pulse. Since this feature allows the separation of pulse width and pulse lag, longer lags can be chosen for lower velocity noise measurements independent of the size of the pulse.

39
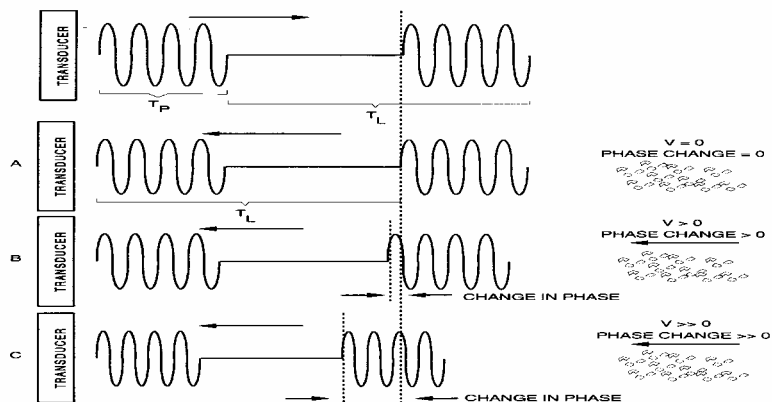
Figure 3.6　　Phase change process for the Broadband System (From RDI BADCP technical manual)

In Figure 3.6, a broadband ADCP transmits two pulses of duration T_P, separated by a lag T_L. Figure 3.6-A shows no phase change, Figure 3.6-B shows a small phase change and Figure 3.6-C shows a bigger phase change due to the relative velocity of the particles, which backscatter the transmitted sound signal to the transducers.
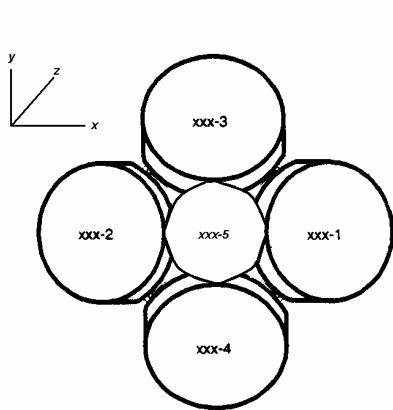
Figure 3.7-A
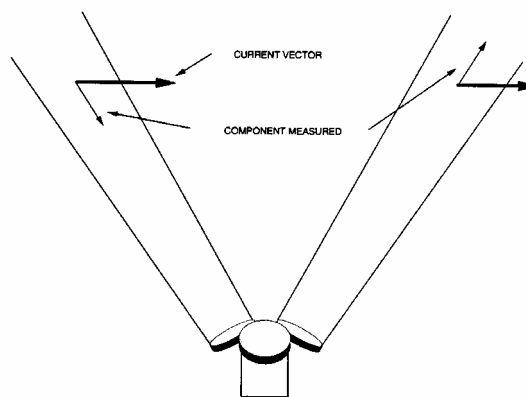
Figure 3.7-B

Figure 3.7　　NPS five-beam BADCP Beam geometry (From RDI BADCP technical manual)

　　　　The BADCP coordinate system and the transducer orientation is shown in Figure 3.7-A. Beam 1 and beam 2 measure the combination of the velocity components in the x and z directions, while beam 3 and beam 4 measure the combination of the velocity components in the y and z directions. Beam 5 only responds to vertical velocity

40

components. Figure 3.7-B is the side view of any two slanted beams and shows measured components of the actual current.

The BADCP has four slanted beams and one vertical beam and the angle between the slanted beams and the vertical is 30 degrees.

BADCP Frequency	Depth Cell or Bin Size	Number of Depth Cells	Pings Per Ensemble	Ensemble Interval
600 kHz.	0.5 m.	40	10	~ 2 sec.

Table 3.   NPS five BADCP parameters used during CBLAST experiment.

The instrument parameters used for this experiment are shown in Table 3. The ensemble interval depends on the pings per ensemble. When pings per ensemble are adjusted to 10, the ensemble interval is automatically assigned by the BADCP to be about two seconds providing a ~0.5 Hz data rate.

THIS PAGE INTENTIONALLY LEFT BLANK

IV. DATA PROCESSING

A series of matlab program modules were written to load the 0.5 Hz (two-second) beam profile data, find the surface return bin, and determine thirty-second low-pass filtered profile time series of velocity and backscatter data beneath the surface. An algorithm to detect the upwelling and downwelling regions of Langmuir circulations was created based on the coherency features of these circulations using the thirty-second beam five vertical velocities in two-hour intervals. Following cell detection, maximum upwelling and downwelling velocities, penetration depth and spacing were defined.

A. LOADING AND BLANKING THE DATA

1. Loading the 0.5 Hz Data

The Loadbadcp matlab function was created to load the two-second data. Loadbadcp uses the mex functions findfile and arin, which link into the raw database. Findfile identifies files for each desired time period, and arin loads the velocity, intensity, and correlation data from each of these files. Loadbadcp concatenates the loaded data into the variables assigned for each data type. For example, v1, v2, v3, v4 and v5 are the variables for the velocity data of beam 1, beam 2, beam 3, beam 4 and beam 5 respectively. Loadbadcp also used the pdrin matlab function to get the header information of the BADCP data, including tilt and heading information for the deployed instrument. In the following analysis thirty-second segments of 0.5 Hz data were loaded.

2. Blanking the Data

The BADCP used in this experiment has no pressure sensor in it, making it difficult to define the sea surface accurately, since the sea surface is changing continuously in response to both waves and tides. However since the BADCP was programmed to collect the data for forty bins (20 m), well beyond the 16 m instrument depth, the sea surface was determined from the strong surface returns seen in the intensity profile time series of beam 5. This allowed the reference bin number, or top safe bin closest to the sea surface, to be defined for each 0.5 Hz raw profile sample.

After loading the two-second data, the sea surface, corresponding to the bin number of maximum intensity, was found between bins 20 and 40 (Figure 4.1). The

vertical beam 5 was chosen for this process to avoid the side lobe and penetrating bubble effects seen in the sloping beams.
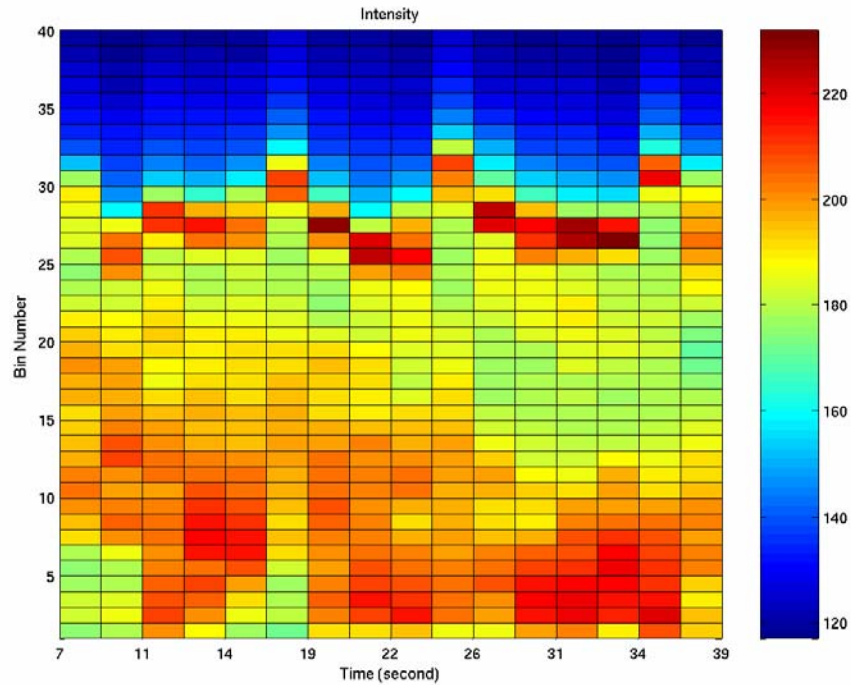
Figure 4.1   The vertical beam 5 intensity time series color plot for 40 seconds during year day 318

Once the surface bin was selected, the bin number three below it was chosen as the blanking boundary, and all the data above this blanking boundary was replaced by NaNs (NaN means not a number in the Matlab programming language). This process was done for each ensemble of two-second data for thirty-second time periods throughout the data set. Vertical beam 5 data were directly blanked while slanted beams were not.

B.   HORIZONTAL AND VERTICAL VELOCITY COMPONENTS

Horizontal velocities were calculated with two different methods, a four-beam solution of slanted beams and a two-beam solution exploiting the vertical beam 5.

1.   Four-Beam Solution of Horizontal Velocity Components

The four-beam solution of horizontal velocity components is typically used in four-beam ADCP's. The horizontal velocity component in the x-direction, u, is calculated by differencing beam 1 and beam 2 (Figure 4.2-A), while the horizontal velocity

component in the y-direction, v, is calculated by differencing beam 3 and beam 4 (Figure 4.2-B). All these solutions presume that the horizontal flow is uniform over the spatial scale between the selected beams at each bin depth.
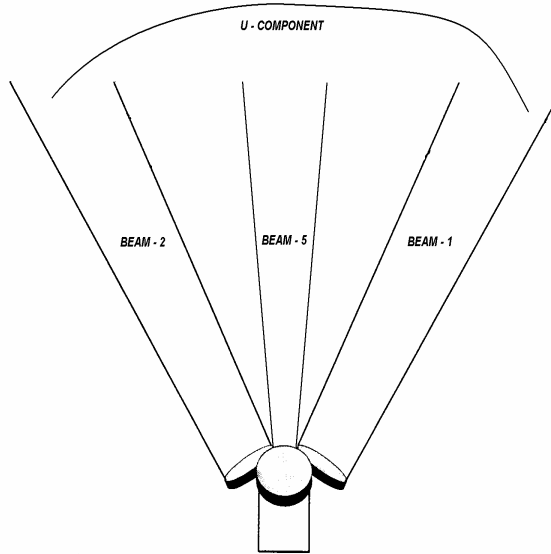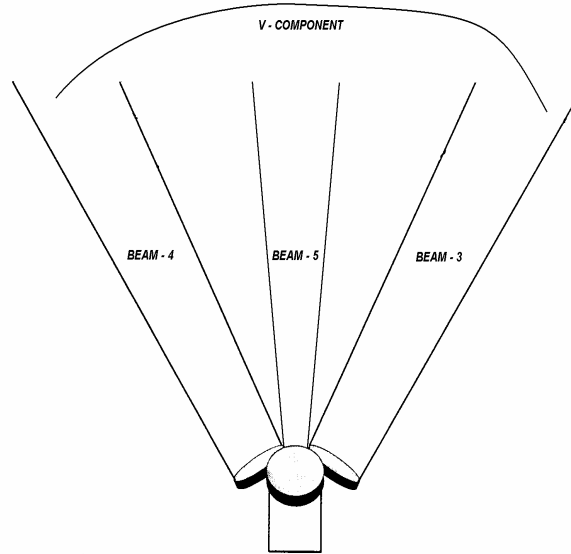
Figure 4.2-A   Figure 4.2-B

Figure 4.2   Horizontal velocity components four-beam solution geometry. The u-component is calculated between beam 1 and beam 2 (Panel A), the v-component is calculated between beam 3 and beam 4 (Panel B) (From RDI BADCP technical manual)

The formulations for the four-beam solution are based on those found in RDI's publication, " Direct Reading and Self-Contained Broadband Acoustic Doppler Current Profiler Technical Manual".

$$u = (-V1 + V2)/\sin\theta \qquad (4.1)$$

$$v = (-V3 + V4)/\sin\theta \qquad (4.2)$$

where, V1, V2, V3, V4 are the measured beam 1, beam 2, beam 3, beam 4 velocities respectively and θ is the thirty degree angle between the vertical axis and the slanted beams. These formulas assume a uniform flow across the aperture formed by the diverging beams at each bin.

2.   Two-Beam Solution of Horizontal Velocity Components

The two-beam solution method calculates the horizontal velocity components between the slanted beams and vertical beam by using the trigonometry between beams as shown earlier in Figure 3.7-B.
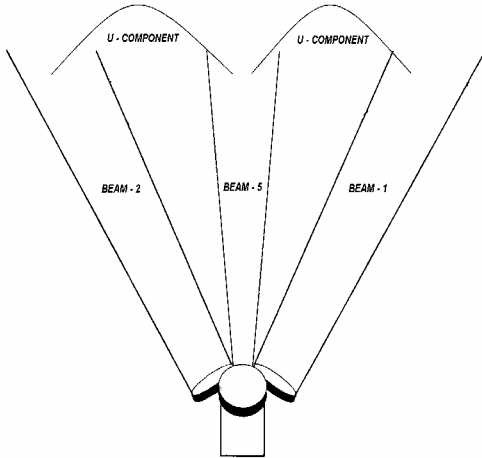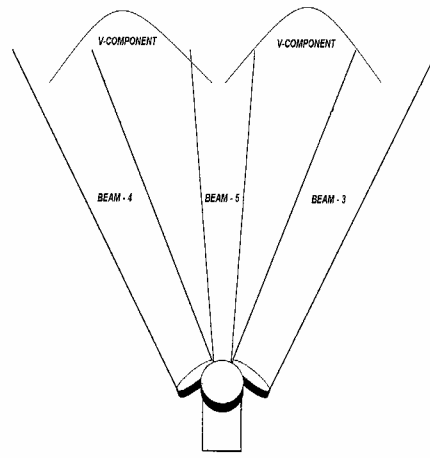
<div style="display:flex; justify-content:space-around;">
Figure 4.3-A   Figure 4.3-B
</div>

Figure 4.3   Panel A: Two different calculation of the u-component with the two-beam solution between beams 1 and 5, and beams 2 and 5. Panel B: Two different calculations of the v-component with the two-beam solution between beams 3 and 5, and beams 4 and 5. The lateral scale over which the horizontal velocity estimates are made is 1/2 that of the four beam solution.

The two-beam solution (Figure 4.3) allows higher resolution estimates of u and v than the four-beam solution as it uses half the scale of the four-beam solution. The u-component between beam 1 and beam 5 is given by

$$u = -\left(\left(V_1 - \left(V_5 \times Cos\theta\right)\right)/Sin\theta\right) \tag{4.3}$$

while the u-component between beam 2 and beam 5 is given by

$$u = \left(V_2 - \left(V_5 \times Cos\theta\right)\right)/Sin\theta \tag{4.4}$$

and the v-component between beam 3 and beam 5 is given by

$$v = -\left(\left(V_3 - \left(V_5 \times Cos\theta\right)\right)/Sin\theta\right) \tag{4.5}$$

while the v-component between beam 4 and beam 5 is given by

$$v = \left(V_4 - \left(V_5 \times Cos\theta \right) \right) / Sin\theta \qquad (4.6)$$

where V_1, V_2, V_3, V_4 and V_5 represent the measured beam 1, beam 2, beam 3, beam 4 and beam 5 velocities respectively, and θ is the thirty degree angle between the slanted beams and vertical beam.

3. Vertical Velocity Solutions

The fifth vertical beam produces vertical velocity profiles from ~0.2 m diameter by 0.5 m vertical sample volumes, and consequently does not require the horizontal homogeneity presumption seen in the u /v velocity estimates above. The vertical fifth beam also provides two u, and two v estimates as discussed above, allowing crude horizontal strain estimates to be made at bin-lag scales.

C. TIME AVERAGING THE DATA

After blanking the two-second beam 5 vertical velocities and calculating horizontal velocity components, the data were averaged into thirty-second blocks to reject orbital motion from surface gravity waves using the matlab function zapmeanmat. Zapmeanmat is an NPS turbulence group function that calculates the mean of every row in an M by N matrix ignoring NaNs, which were put in the velocity matrices by the blanking process. (Figure 4.4)
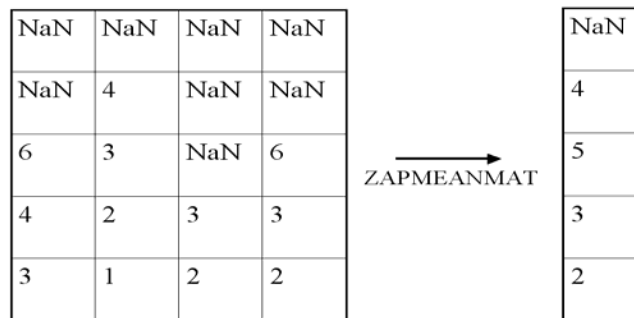
Figure 4.4   Thirty-second temporal averaging of the BADCP data. The 5 by 4 matrix represents the 40 by 15 raw data matrix. The rows are numbered from bottom to top and represent the bin numbers while the columns represent the two-second ensembles, with 15 columns of data loaded for every thirty-second time period.

Loading, blanking and averaging processes were done in the "mnvelcom" matlab routine. Mnvelcom loops through two-hour intervals between selected start and end days.

It loads the raw data in thirty-second increments at each step of the loop, and applies the blanking and averaging processes. Finally, mnvelcom creates thirty-second beam 5 vertical velocities, horizontal velocity components and intensity profile time series for each two-hour period. Mnvelcom also calculates the mean and the standard deviation of the boundary bin numbers of the blanking process for every thirty-second period in the loop, as shown in Figure 4.5
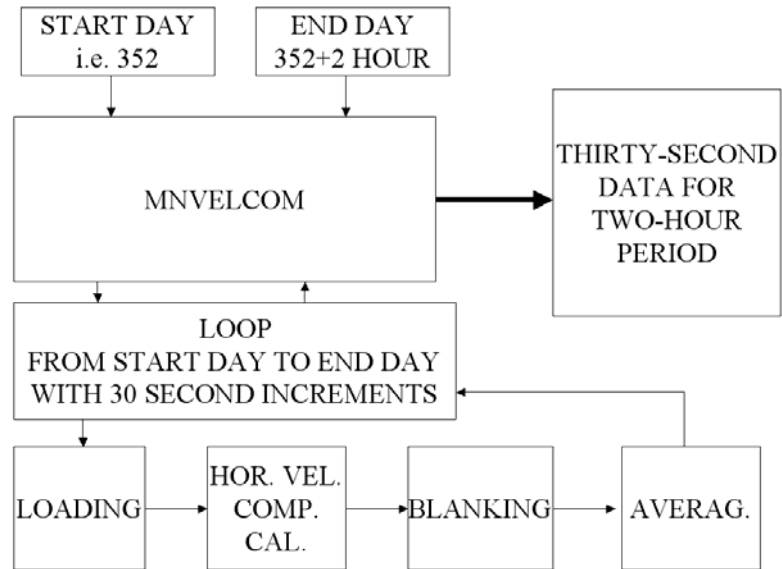
Figure 4.5   Mnvelcom matlab routine algorithm for loading the 0.5 Hz data, blanking and thirty-second temporal averaging processes and creating thirty-second data for two-hour periods.

D.   DEFINING THE NEAR-SURFACE REFERENCE BIN NUMBER

A near-surface reference bin number was found for the bin closest to the sea surface that has valid data for each thirty-second data set in every two-hour period. The Refbindefin.m matlab routine was created to define the reference bin number, which allows near-surface vertical velocity to be calculated for detecting Langmuir circulations in subsequent analyses.

The near-surface reference bin number was found from profiles of standard deviations of the thirty-second averaged data for each two hour period. Under energetic waves with large amplitudes (Figure 4.6), there is a distinct break in vertical velocity standard deviations increasing toward the surface due to surface beat, turbulence and

Langmuir circulations and very high values close to the surface (Figure 4.7). These large standard deviation values are attributed to surface-hit-contaminated vertical velocity measurements not screened out from the relatively slow two-second sampling of intensity profiles. This distinct breakpoint allowed these velocity bins to be excluded from subsequent analyses.
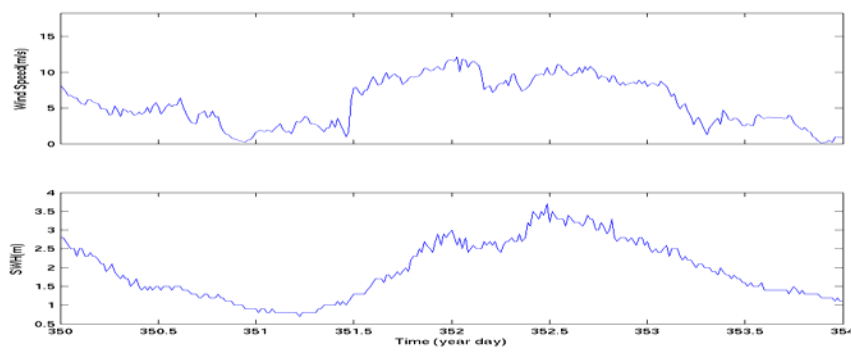
Figure 4.6   Wind speed and significant wave heights (SWH) for the days between 350 and 354. The energetic high amplitude waves are in between days 351.5 and 353.5
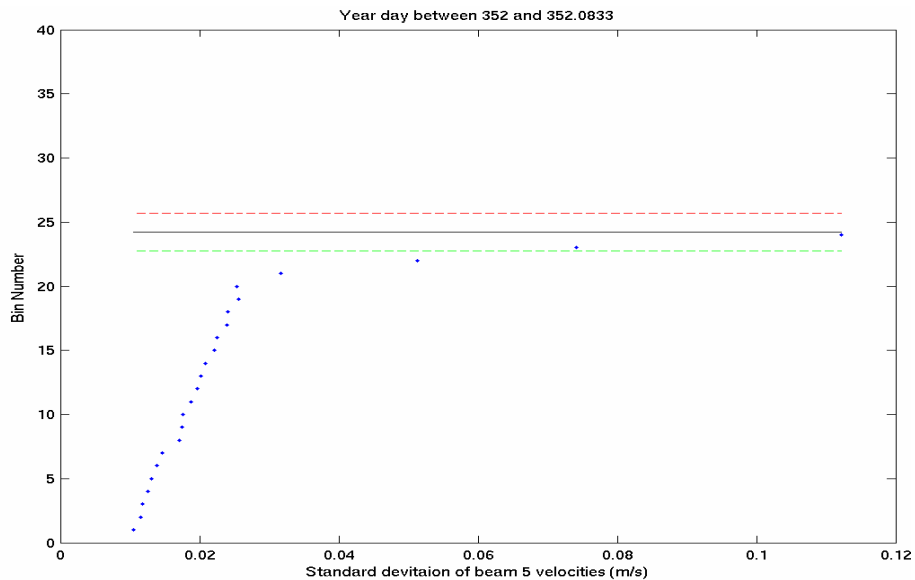
Figure 4.7   Temporal Standard Deviations (dots) of beam 5 vertical velocities for the high wind / wave time period between the days 352 and 352.0833. Solid line is the mean bin number (or mean sea level) defined during the blanking process while red and green lines are standard deviations from mean sea level.

To illustrate this screening process, Figure 4.6 shows the significant wave heights and wind speed between the days 350 and 354 with wave height increasing from 0.8m to

3.5m during twelve-hour period. Figure 4.7 shows the standard deviations (dots) of the thirty-second beam 5 vertical velocities for a two-hour period between year day 352 and 352.0833.

The slope between each dot was calculated as

$$slope = \frac{\Delta(std(V5))}{\Delta(Bin\,No)} \tag{4.7}$$

where std is the standard deviation in time, V5 is beam 5 vertical velocities in ms^{-1} and Δ represents the difference between each point and each bin. For the slopes greater than 0.01, the corresponding velocity bins were considered as bad. The bin number one below the highest bin whose slope was less than 0.01 was chosen as reference bin number for high wave cases. For the case shown in Figure 4.7, the reference bin number was defined as 19.

For low wave cases (Figure 4.8), the same method was used as the high wave case but in this case the bin number two below the slope break-point was chosen as reference bin number.
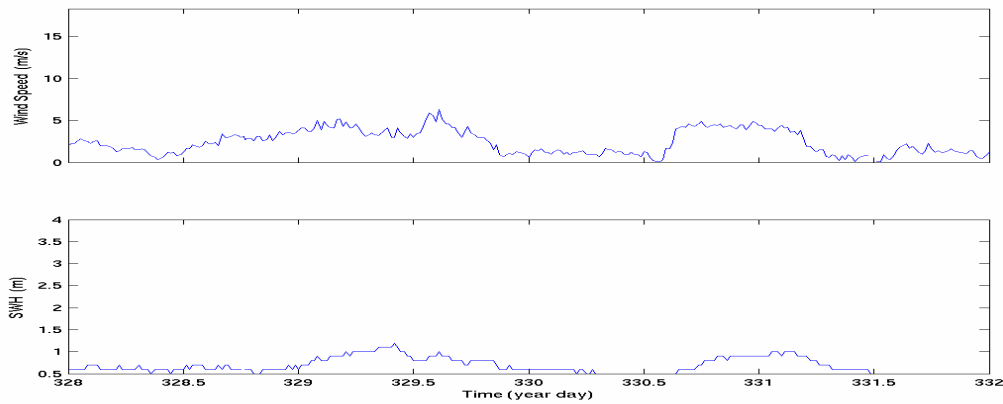
Figure 4.8   Wind speed and significant wave heights between (SWH) the days 328 and 332 representing the low wave case.
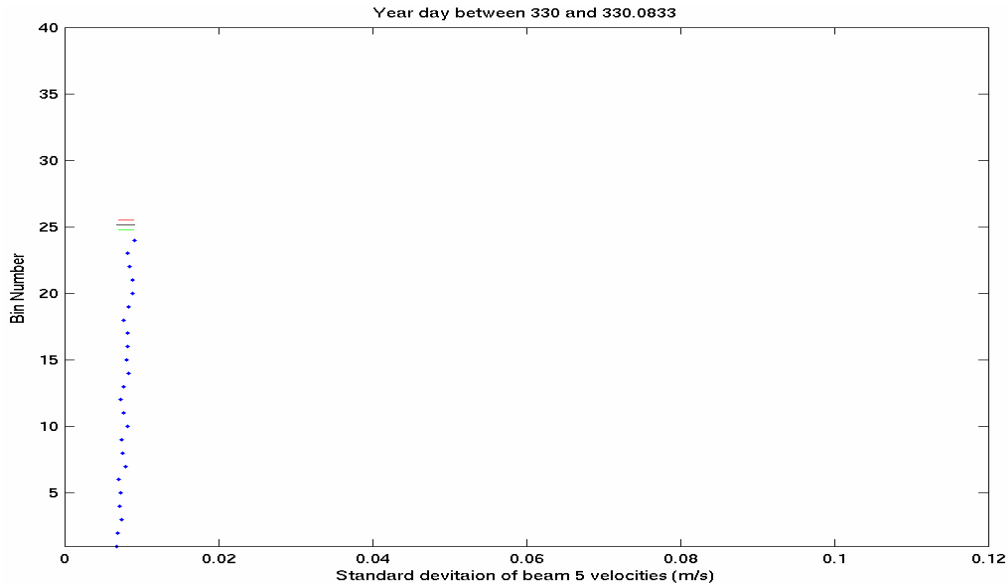
Figure 4.9 Temporal Standard Deviations (dots) of beam 5 vertical velocities for low wind / wave time period between the days 330 and 330.0833. Solid line is the mean bin number (or mean sea level) defined during the blanking process while red and green lines are standard deviations from mean sea level.

Figure 4.9 represents the standard deviations of the beam 5 velocities for the time period between the year day 330 and 330.0833 to show a typical low wind and low wave case. Low winds and low waves are dominant in day 332 (Figure 4.8). If the standard deviation of the blanking boundary bin numbers shown with green or red dashed lines from mean sea level (solid line) in Figure 4.9 is less than 0.47 (about 0.2 m), the program considers this case as low wave case and defines a reference bin number two bins below the break-point bin number estimated by the algorithm explained above.

Having defined the near-surface top safe velocity bin, all the data matrices' sizes were adjusted to their reference bin number. For example, if the reference bin number was 20, bin numbers above the twentieth bin were neglected in a 40 by 240 matrix. Therefore adjusted the matrix became 20 by 240.

E. FILTERING THE DATA

The beam 5 vertical velocities and the horizontal velocity components were two minute low-pass filtered in time to minimize the residual effects of orbital swell motion. The vertical velocity data were also 20-minute high-pass filtered in time to reject the

horizontal velocities entering from the slightly tilted vertical beam. The NPS Lpfilt matlab function was used to apply low-pass filtering while hpfilt matlab function was used to apply high-pass filtering, with both filters using a four-pole Butterworth response. Beam 5 vertical velocity data also was spatially low-pass filtered vertically through the water column with a 4 m cutoff and second order filter, before calculating the maximum upwelling / downwelling velocities and the penetration depths of the Langmuir circulations.

F.   LANGMUIR CIRCULATIONS DETECTION PROCESS

After completing the processes described above, beam 5 vertical velocities were used to detect the Langmuir circulations. The detection process was based on the coherency features of the Langmuir circulations through the water column.

The mean of the top four clean velocity bins was calculated, where the top of these four bins was the reference bin number. The near-surface mean velocities were used to define upwelling and downwelling regions of Langmuir circulations.
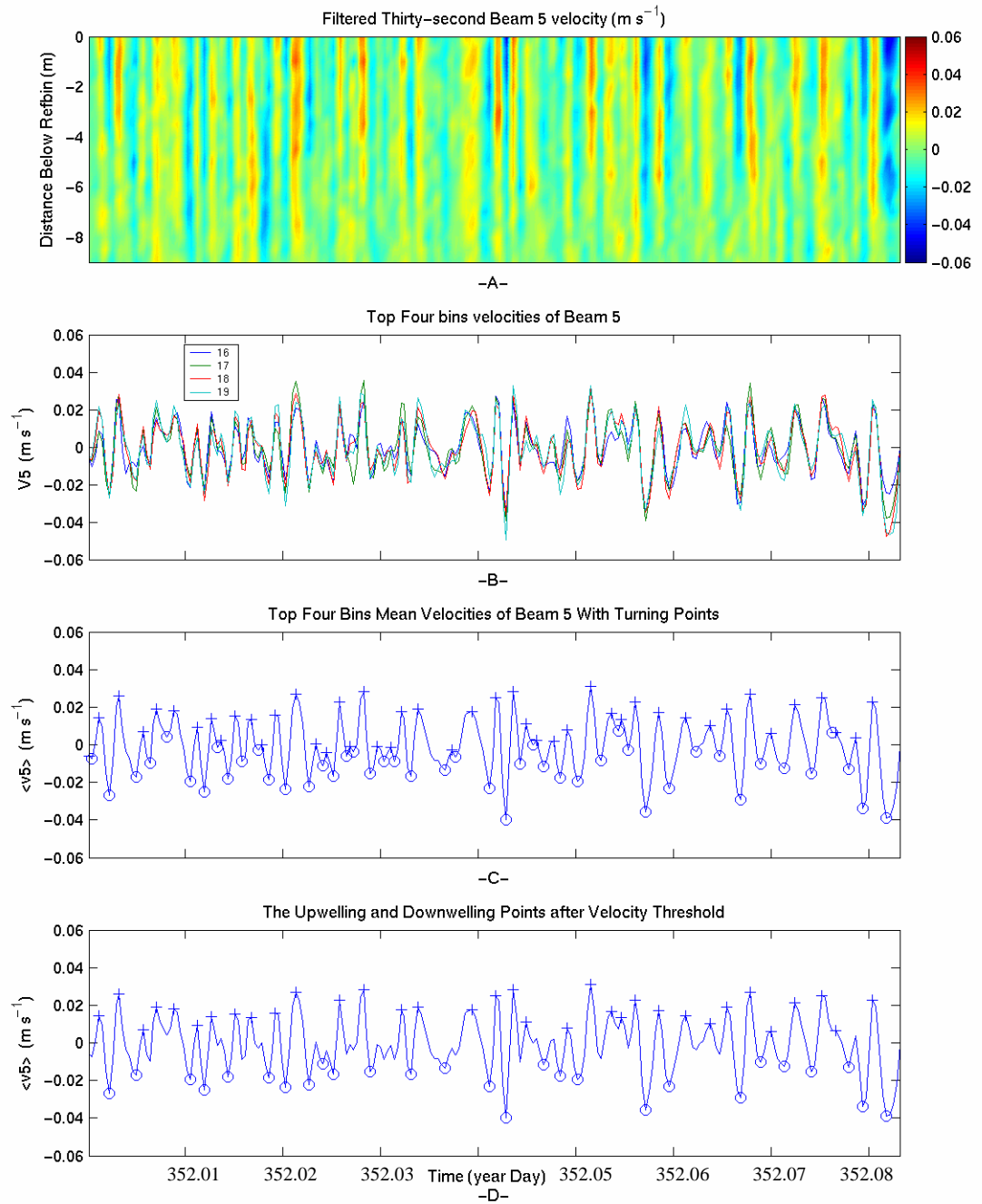
Figure 4.10   Langmuir circulations Detection Process: The color contour plot of vertical velocities (Panel A); Time series plot of upper four bin (2 m) vertical velocities where the reference bin number is 19 (Panel B); Mean of the upper four bin (2m) vertical velocities and finding all the turning points where the circles are downwelling velocities, crosses are upwelling velocities (Panel C); Applying thresholds + 0.005 ms^{-1} for upwelling velocities, and -0.01 ms^{-1} for downwelling velocities in panel C and yields panel D

53

Figure 4.10 represents the beam 5 vertical velocity profile including the upwelling and downwelling velocities between the days 352 and 352.0833 (two hour period) when the high waves and high winds were dominant. In this case, reference bin number is 19. Figure 4.10-A is a color contour plot of beam 5 velocities after the band pass filtering process, with the color scale on the right panel. Downwelling regions are presented by the bluish colors while the upwelling regions presented by reddish colors. Figure 4.10-B is the top four bins' velocities of beam 5 versus time. Each bin is represented by a different color. In Figure 4.10-C, the solid blue line is the mean of the upper two-meter clean vertical velocities shown in Figure 4.10-B. The plus signs in Figure 4.10-C show the upward turning points of the solid blue line and the circles show the downward turning points of the solid blue line, and thus show the upwelling and downwelling velocities respectively. In order to detect the Langmuir circulations velocity thresholds were applied to these upwelling and downwelling regions. Velocities less than $+ 0.005$ ms^{-1} were neglected for upwelling regions while the velocities less than $- 0.01$ ms^{-1} were neglected for downwelling regions. The plus signs and the circles in Figure 4.10-D show the remaining upwelling and downwelling regions after velocity thresholds respectively.

A vertical coherency test was applied to the remaining points as the last step of the detection process. The vertical velocities of the top four bins were tested for coherency by measuring the normalized standard deviation (NSD) of the top four clean bins at each selected upwelling / downwelling event. For NSD > 0.35 across these four bins, the detected event was deemed vertically incoherent, and was rejected. The value of 0.35 was chosen after many trials of data sets for different cases, including low winds-low waves, high winds-high waves, increasing winds-increasing waves, and decreasing winds- decreasing waves. For NSD less than 0.35 corresponding downwelling and upwelling points were assigned as Langmuir circulation events.
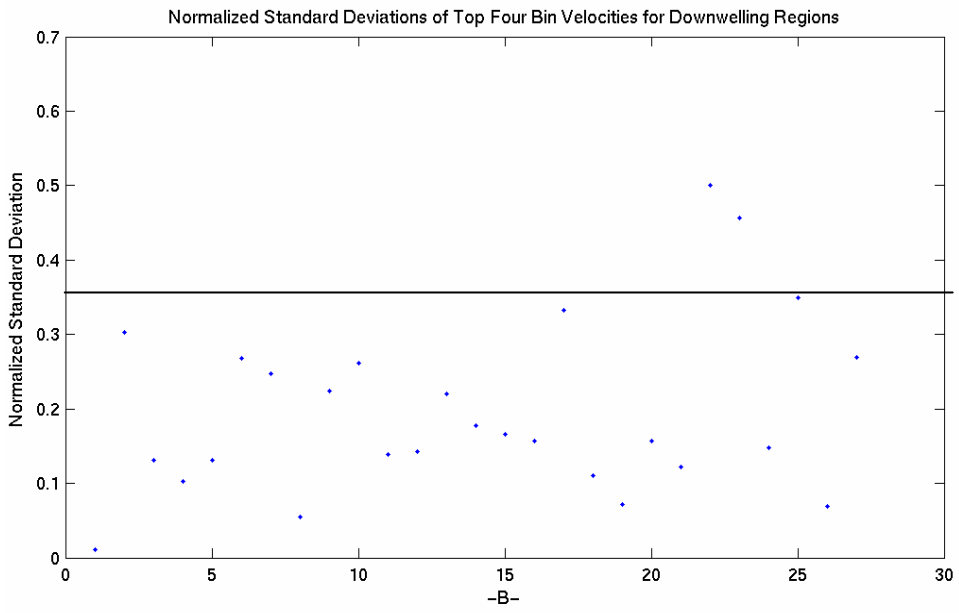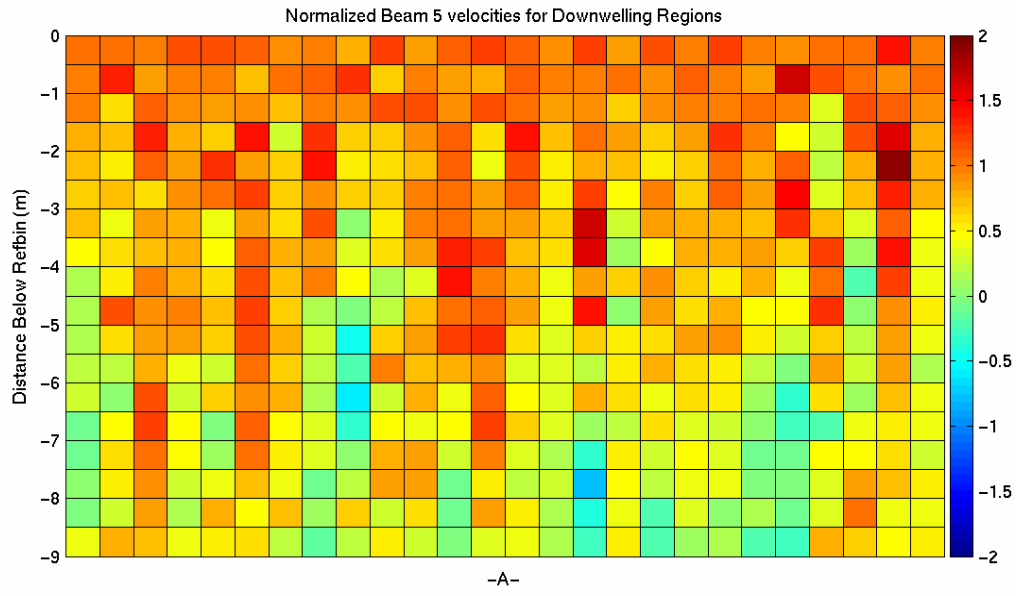
Figure 4.11   Normalized Beam 5 vertical velocities (Panel A) and Normalized standard deviations (NSD) of top four bin vertical velocities (Panel B) for downwelling events shown in Figure 4.10-D. The horizontal solid line in Panel B represents the 0.35 NSD thresholds.
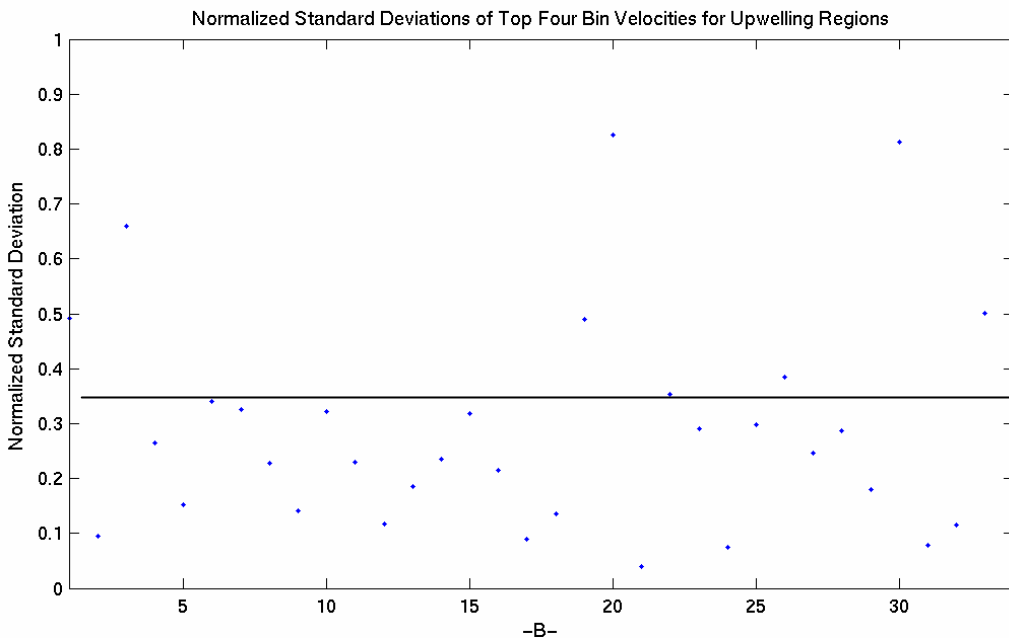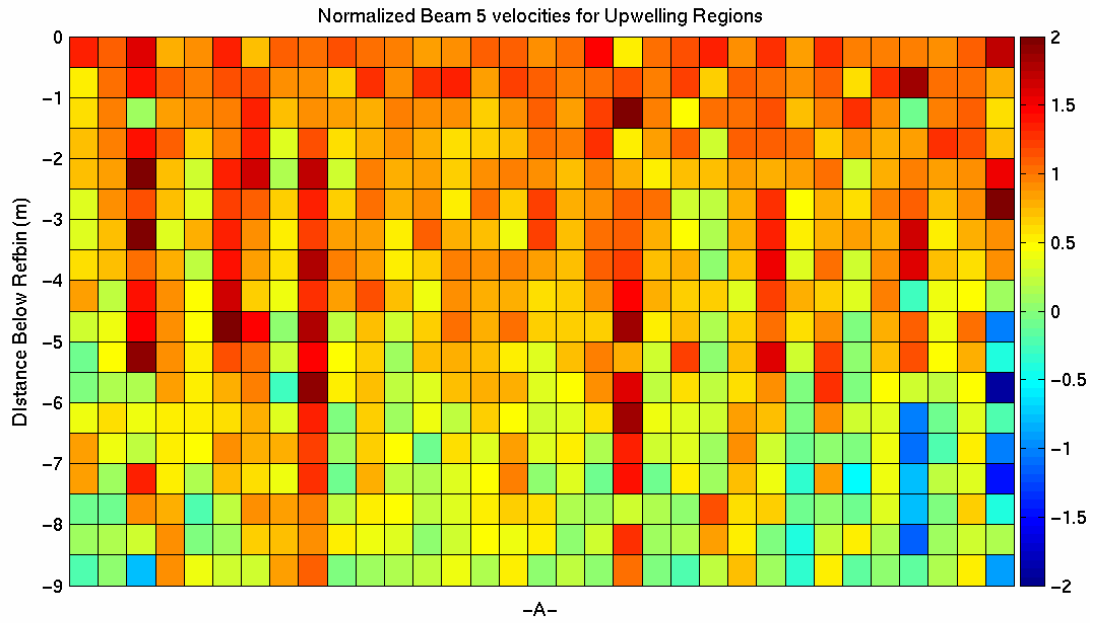
Figure 4.12   Normalized Beam 5 vertical velocities (Panel A) and Normalized standard
deviations (NSD) of top four bin vertical velocities (Panel B) for
upwelling events shown in Figure 4.10-D. The horizontal solid line in
Panel B represents the 0.35 NSD thresholds.

In Figures 4.11 and 4.12 the top four bin normalized velocities for each downwelling and upwelling points have the similar color shading if their NSD values are less than 0.35 while they have distinguishable contrast colors (i.e. red, yellow, blue etc). if their correspondent NSD values are greater than 0.35.
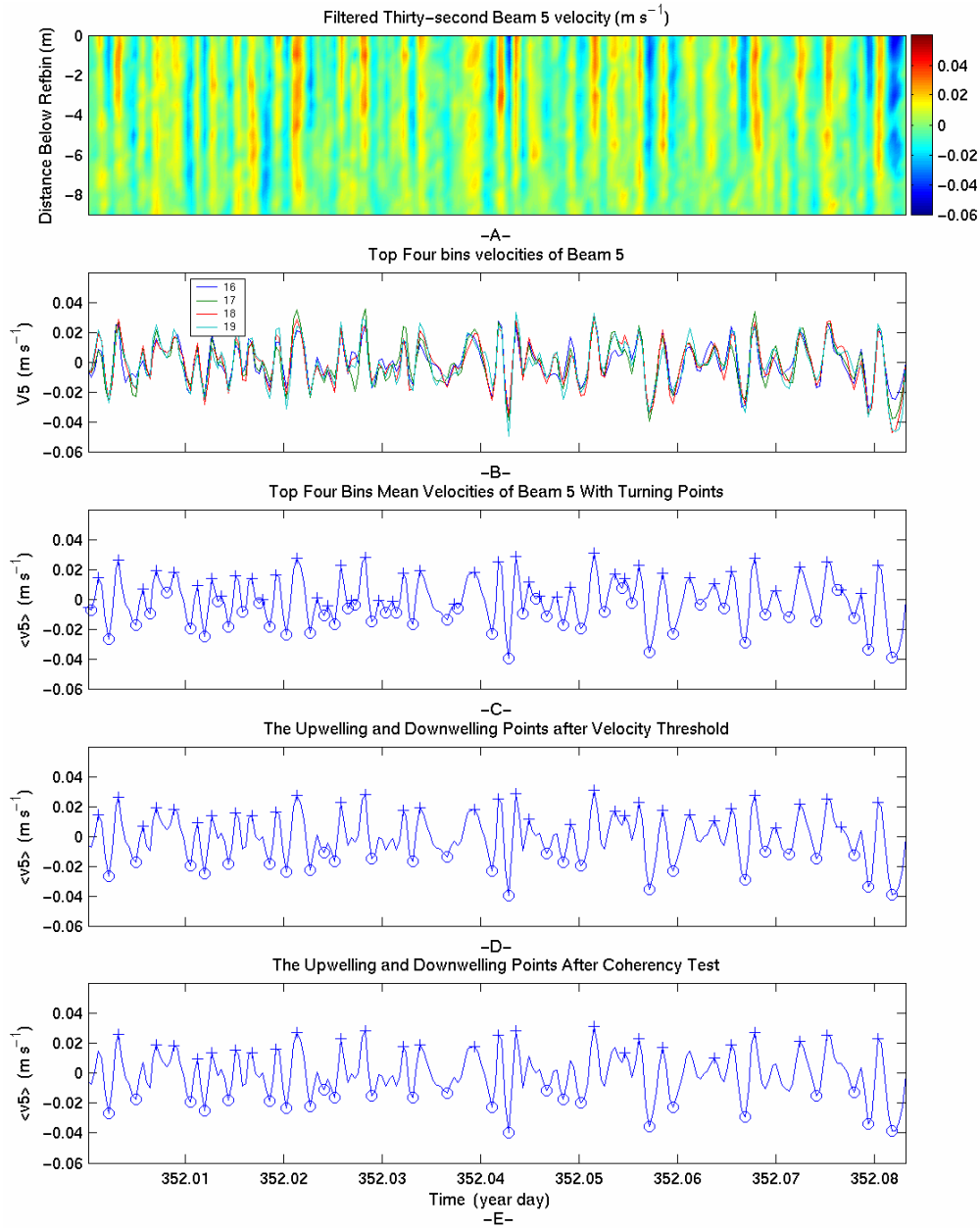
Figure 4.13   Langmuir circulations detection process: Detected downwelling and upwelling velocities of Langmuir circulations after the coherency test of the downwelling and upwelling regions shown in Figure 4.10 –E. The first four panels are the same as in Figure 4.10.

The detection algorithm was applied to other cases with different forcing conditions as follows.
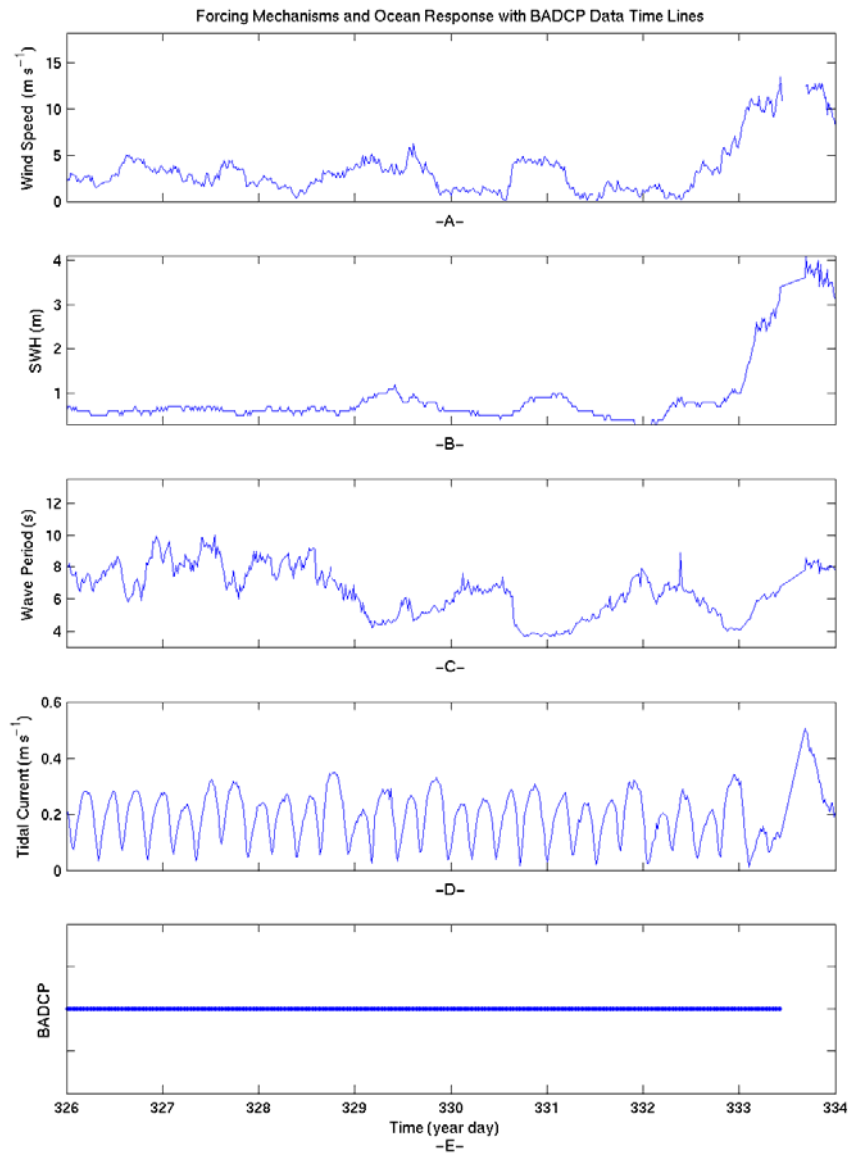
Figure 4.14   Atmospheric and oceanic forcing mechanisms with the available BADCP data in winter time between the days 326 and 334. The wind speed in Panel A is low to moderate till the day 332.3 and after this day storm system is effective. The increasing wind speed from 0 to 14 ms^{-1} between the days 332.3 and 333.5, trigger the ocean and wave heights in Panel B increases from 0 to 4 m during the same time period which is a good case for Langmuir circulation development. The wave period is in Panel C and the tidal currents at the surface in Panel D, which are strong enough to compete with the Langmuir circulations horizontal velocities. Times of available BADCP data are in Panel E for this time period of year.

58

Two hour time periods between the days 326 and 334 (Figure 4.14) were chosen to apply the detection algorithm for different forcing mechanisms. The following 5 figures represent the detected downwelling / upwelling regions of Langmuir circulations and have the same format of Figure 4.13.
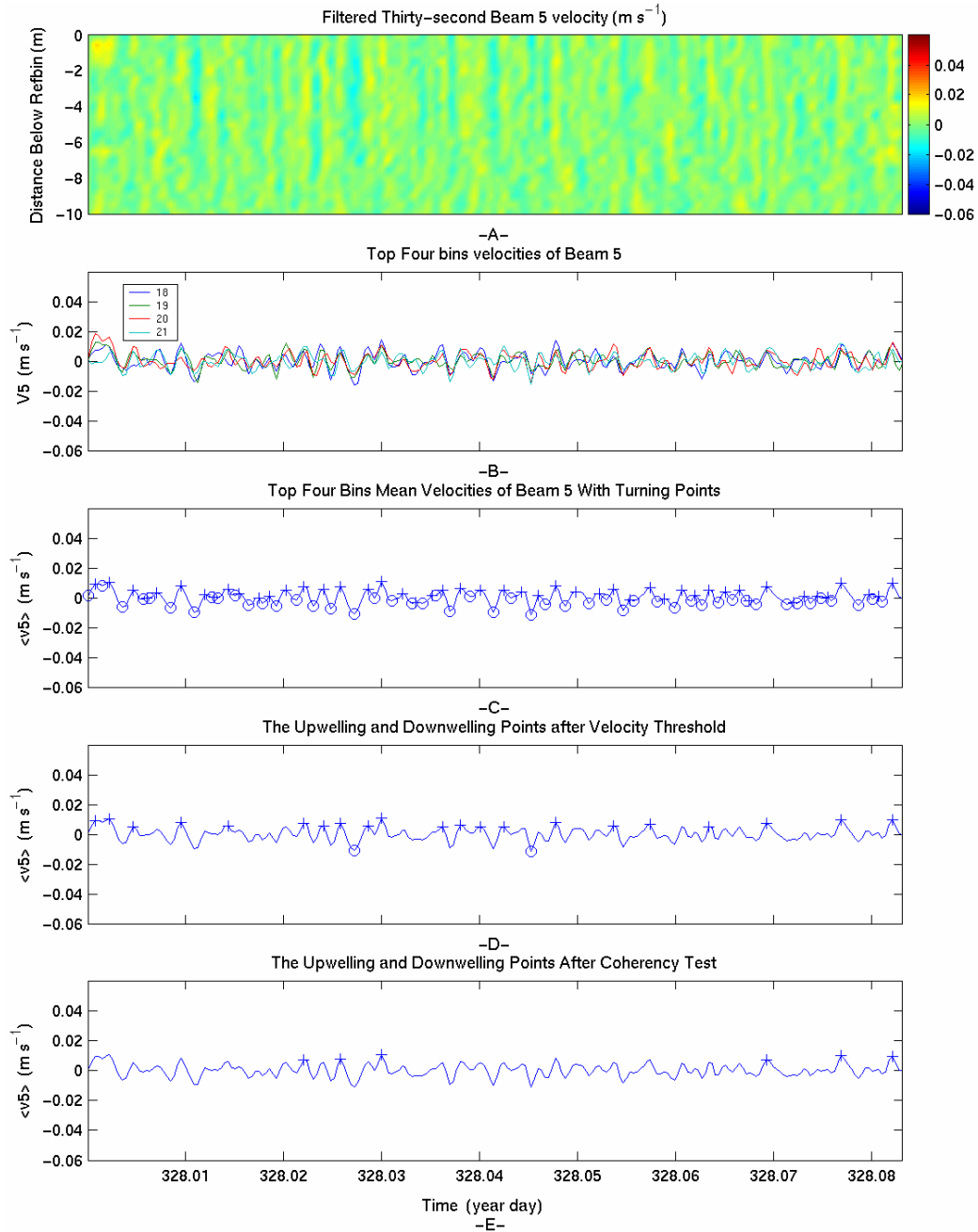
Figure 4.15   Detection of upwelling / downwelling regions of Langmuir circulations between the days 328 and 328.0833. The wind speed is ~2 ms^{-1} and the wave height is ~ 0.3 m. 6 upwelling regions (Panel E) were detected.

The vertical velocities (Figure 4.15-A) are low as well as the wind speed and wave heights. So most of the upwelling / downwelling velocities detected in Figure 4.15-C is eliminated after the velocity thresholds and remaining ones are in Figure 4.15-D. Only six upwelling regions pass the coherency test (Figure 4.15-E) for this low wind speed and wave height case.
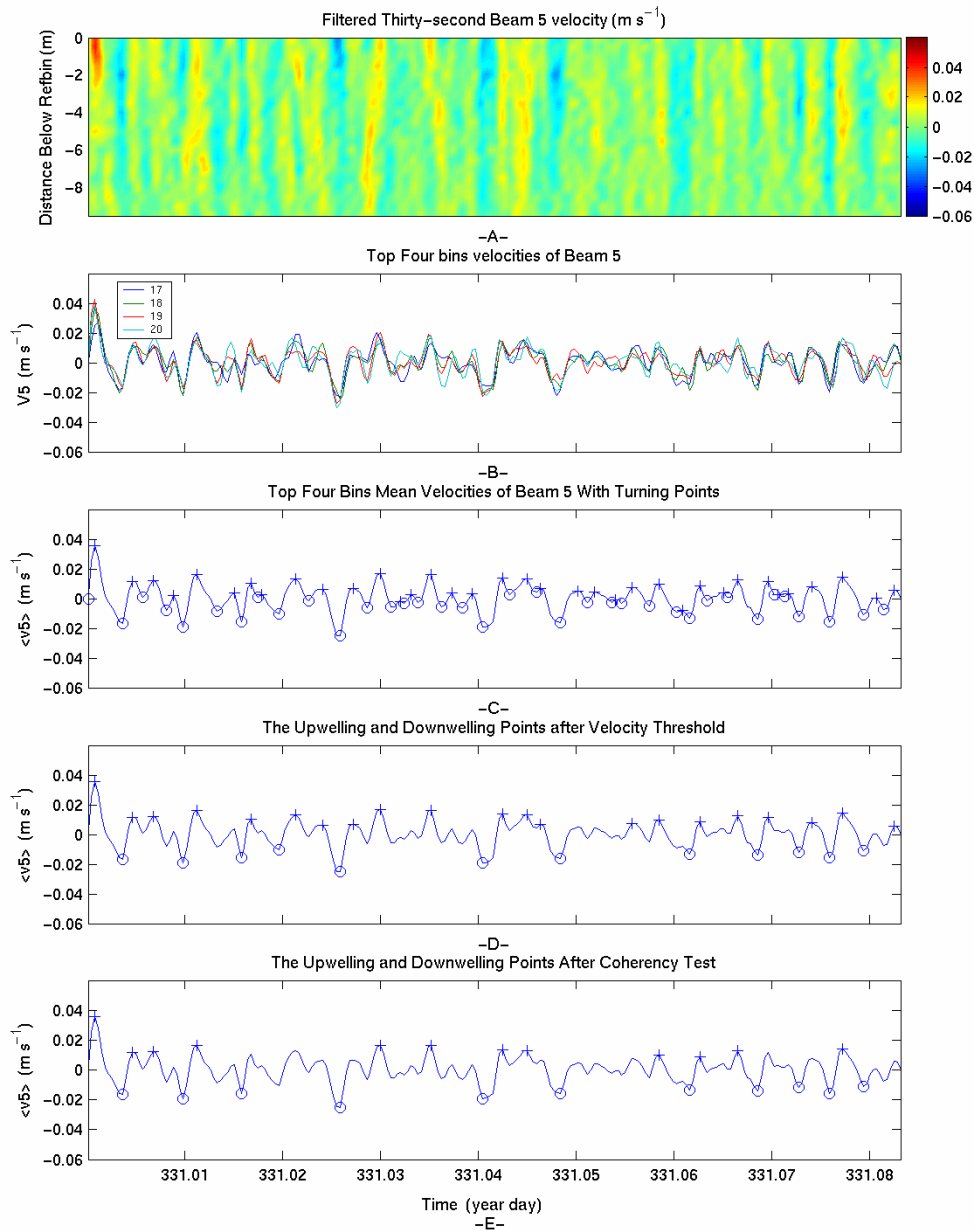
Figure 4.16   Detection of upwelling / downwelling regions of Langmuir circulations between the days 331 and 331.0833. The wind speed is ~5 ms^{-1} and the wave height is ~ 1 m. 12 upwelling regions and 11 downwelling regions (Panel E) were detected.

60

The increasing wind speed and wave height case (locally developed seas) is between the days 331 and 331.0833 (Figure 4.16). The vertical velocities (Figure 4.16-A) are stronger and there are more coherent upwelling / downwelling velocities through the water column than the previous case. This is a typical case for Langmuir circulations to occur in the ocean, which has increasing wave height due to increasing wind speed.
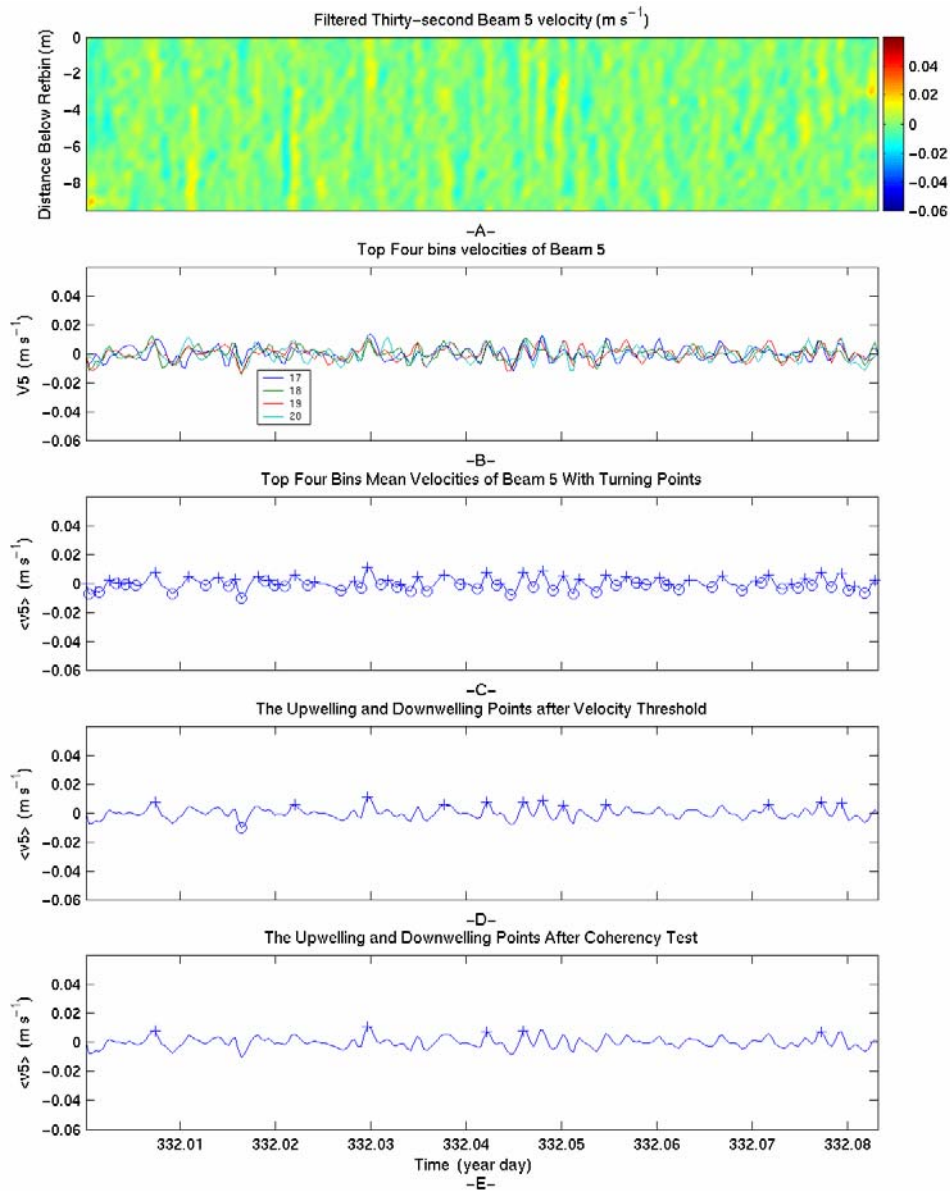
Figure 4.17   Detection of upwelling / downwelling regions of Langmuir circulations between the days 332 and 332.0833. The wind speed is ~1 ms^{-1} and the wave height is ~ 0 m. 5 upwelling regions (Panel E) were detected. This is the time period right before a storm case between the days 332.6 and 334.

The case shown in Figure 4.17 has low wind speed / wave height and few detected upwelling velocities (Figure 4.17 –E). This is a time period right before a storm case. The following two cases are for developing and well-developed storm cases to show the increasing amount of detected Langmuir circulations.
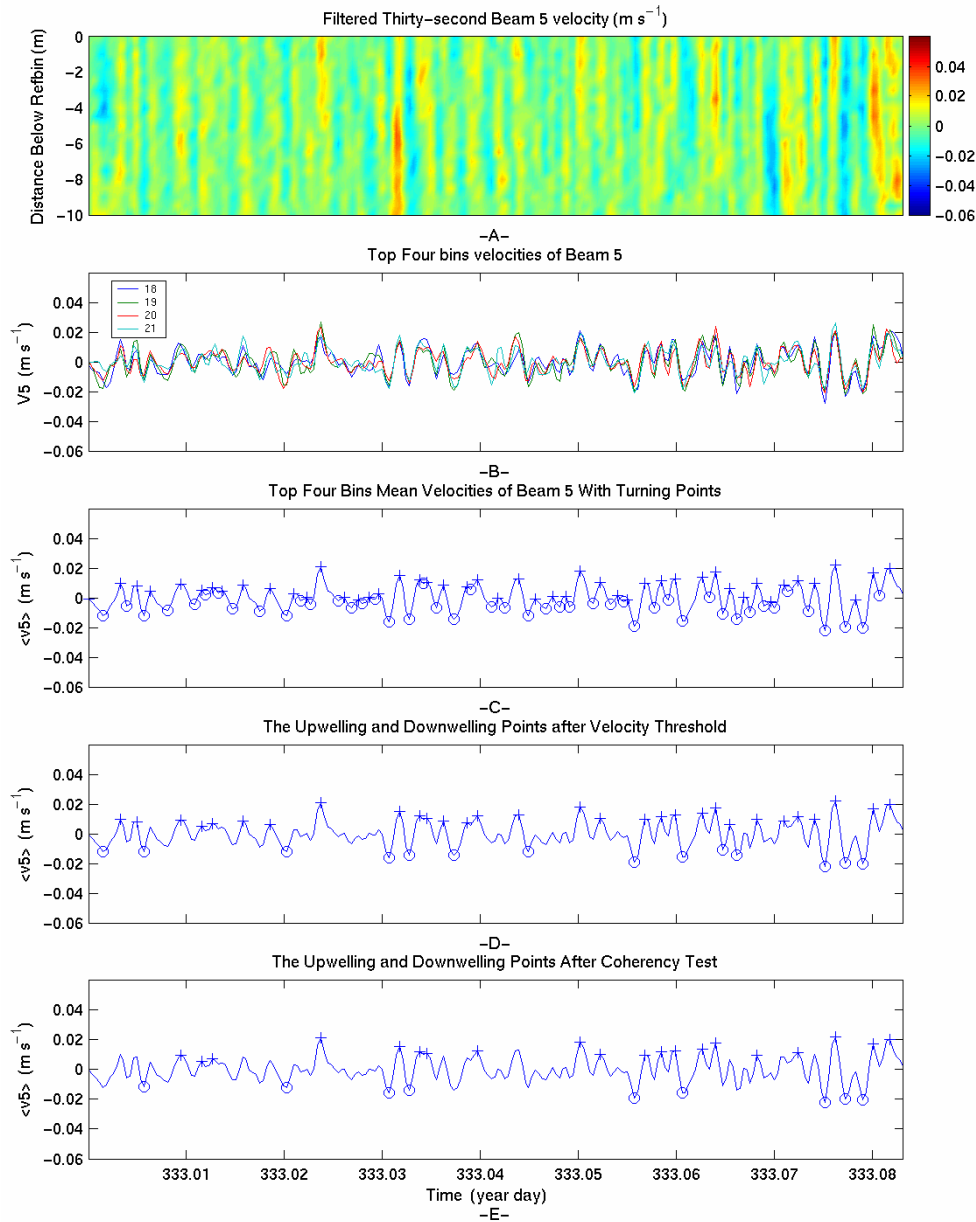
Figure 4.18   Detection of upwelling / downwelling regions of Langmuir circulations between the days 333 and 333.0833. The wind speed is ~7 ms^{-1} and the wave height is ~ 1.2 m. 20 upwelling regions and 9 downwelling regions (Panel E) were detected. The beginning stage of the storm event where the wind speed and wave height are increasing simultaneously.

62

The vertical velocities are getting stronger between the days 333 and 333.0833 (Figure 4.18-A). The Langmuir circulations upwelling and downwelling velocities are very distinguishable in Figure 4.18-A, where the reddish colors represent the upwelling while the bluish colors represent the downwelling regions and these regions are detected in Figure 4.18-E.
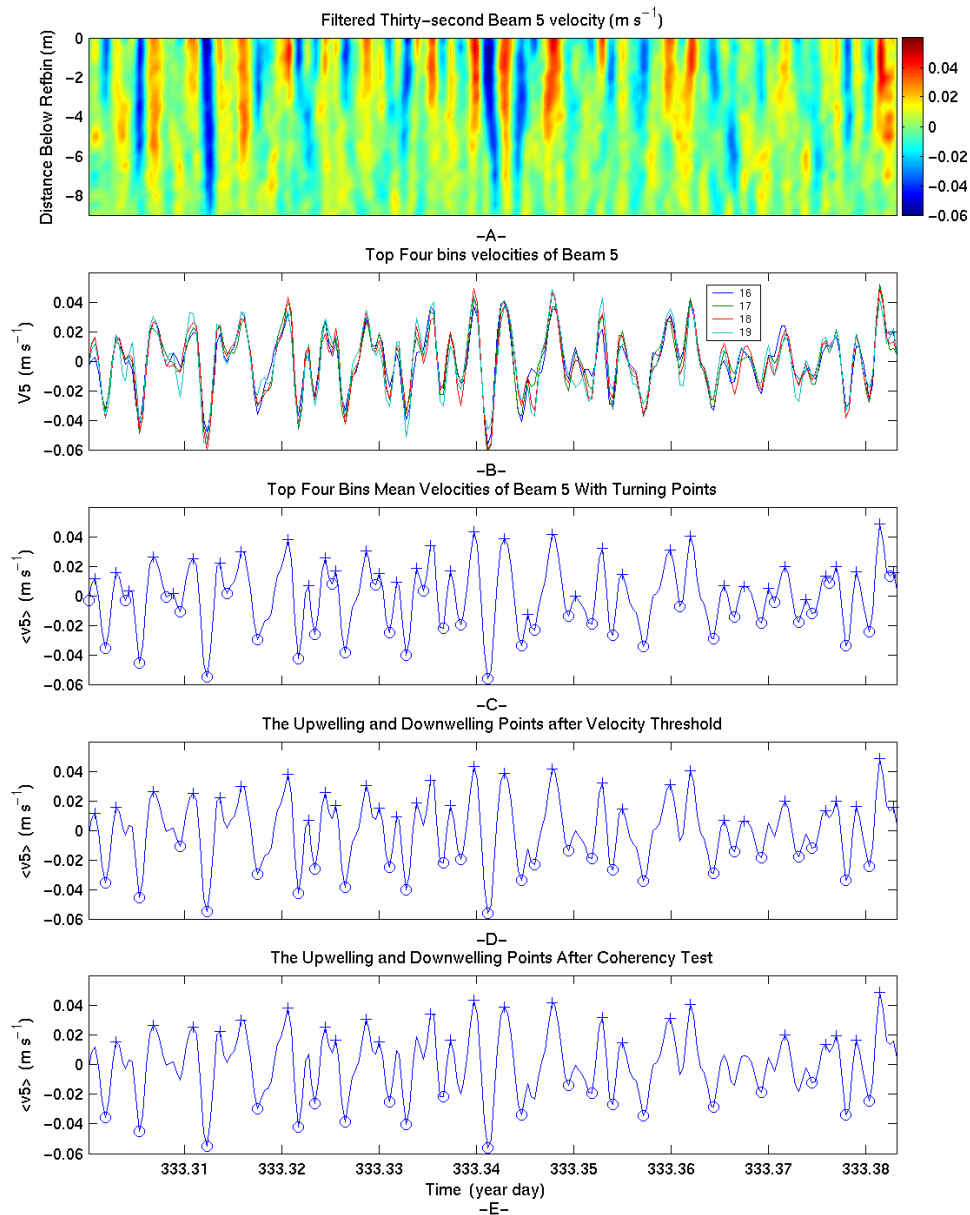
Figure 4.19   Detection of upwelling / downwelling regions of Langmuir circulations between the days 333.3 and 333.3833. The wind speed is ~11 ms^{-1} and the wave height is ~ 3 m (the peak of the storm). 24 upwelling regions and 21 downwelling regions (Panel E) were detected.

63

The peak of the storm event is shown in Figure 4.19 with clean detected Langmuir circulations. The vertical velocities in Figure 4.19–A are very strong (about 0.06 ms^{-1} for downwelling, 0.05 ms^{-1} for upwelling) through the water column at locations detected Langmuir circulations in Figure 4.19–D. The high wind speed and energetic waves due to this high wind speed creates stronger Langmuir circulations and the algorithm for detection of these circulations is working well.

AVERAGING TOP FOUR BIN VELOCITIES OF BEAM 5

FINDING ALL UPWELLING AND DOWNWELLING REGIONS

APPLYING VELOCITY THRESHOLDS
>0.005 M/S FOR UPWELLING REGIONS
>0.01 M/S FOR DOWNWELLING REGIONS

CREATING NORMALIZED BEAM 5 VELOCITIES AND
CALCULATING NORMALIZED STD. OF TOP 4 BIN

APPLYING TRESHOLD TO THE NORMALIZED STD.
<0.35 (COHERENCY TEST)

DETECTION OF THE UPWELLING/DOWNWELLING
REGIONS RELATED TO LANGMUIR CIRCULATIONS

Figure 4.20   Summary of detection algorithm of upwelling / downwelling regions related to Langmuir circulations.

The diagram in Figure 4.20 shows the steps of the detection algorithm of Langmuir circulations in a hierarchy.

G.   MAXIMUM UPWELLING / DOWNWELLING VELOCITIES

The maximum vertical velocities of Langmuir circulations in the water column were searched for each individual detected upwelling and downwelling regions. The Beam five vertical velocities, previously low and high-pass filtered in time, were 4 meters low-pass filtered in space (vertically) before defining the maximum velocities. The depth of each of these maximum velocities was also saved for the following penetration depth analysis.

H.   PENETRATION DEPTHS OF UPWELLING AND DOWNWELLING REGIONS

The penetration depths of each detected event were defined as the maximum depth where the coherent Langmuir circulations differed from near-surface values by a selected ratio. The algorithm to define the penetration depth was based on the beam five vertical velocities after vertical low-pass filtering. The normalized beam five velocities were calculated by taking the ratio

$$ratio(z,t) = \frac{v5(z,t)}{\langle v5(t) \rangle} \qquad (4.8)$$

where z is the vertical depth and $\langle v5(t) \rangle$ is the vertical mean of the upper four bin velocities at each time t. At each detected upwelling and downwelling event, this ratio was used to determine the penetration depth by finding the depth where the vertical velocity had decreased from the near-surface values by a selected ratio. Threshold ratios of 0.2, 0.3 and 0.4 were evaluated for skill in defining upwelling / downwelling depths, and three different bin numbers with regard to the three different thresholds were found as representative of the penetration depth. One of these three different bin numbers was assigned as final penetration depth bin number by the method described below. The bin number representing the penetration depth was converted to meters since every bin number was 0.5 m length, and the distance between the reference bin number and mean sea level was added to the penetration depth.
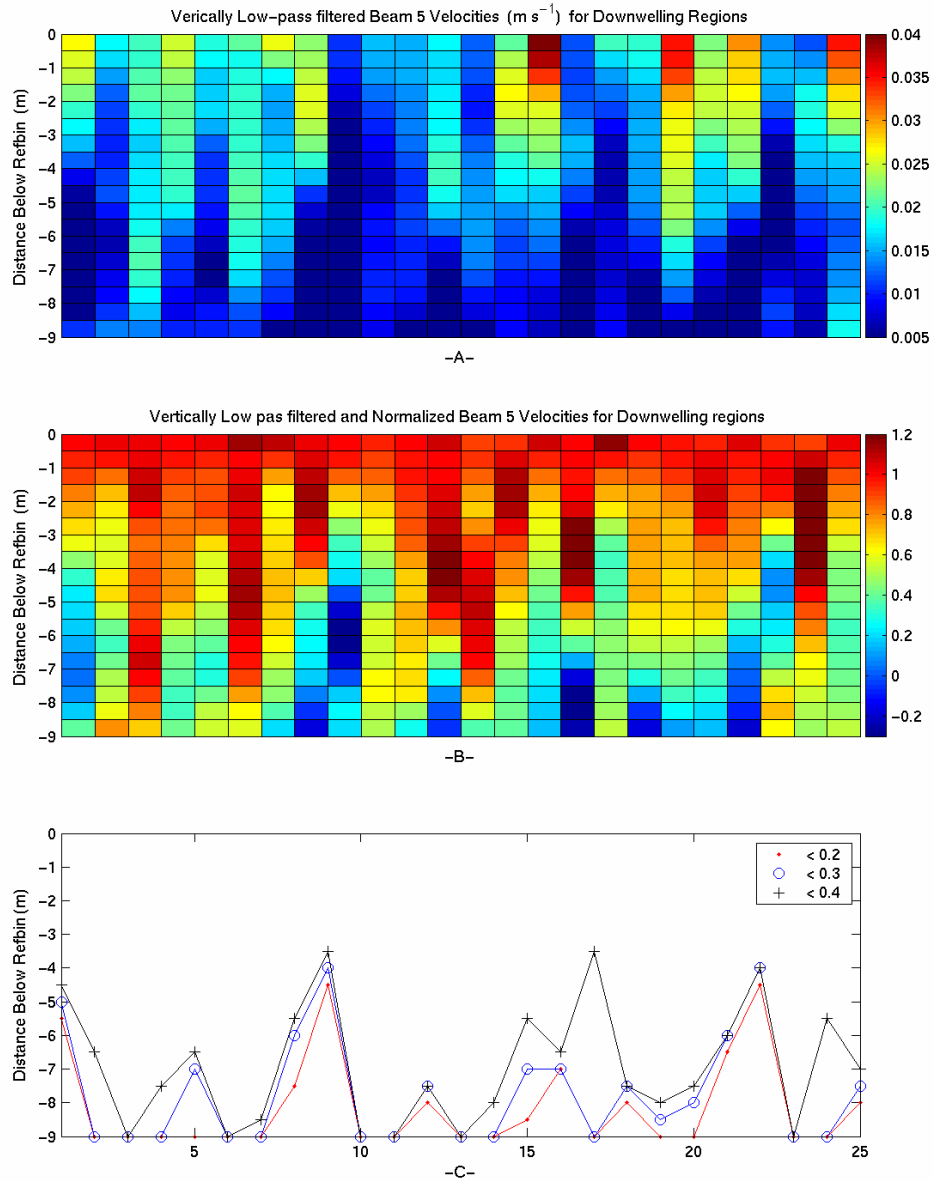
Figure 4.21   Detection of penetration depths for downwelling regions related to Langmuir circulations between the days 352 and 352.0833 (two-hour period). Panel A is vertically 4 m low-pass filtered beam 5 vertical velocities. Panel B is normalized beam 5 vertical velocities by Equation 4.2, the reddish shading color indicates the velocities similar to the near surface velocities while the bluish shading indicates weaker velocities than the near-surface velocities and Panel C shows the penetration depths for the downwelling regions after ratio thresholds.

The reddish color shading in Figure 4.21-B indicates vertical velocities with values similar to near-surface values, while the bluish color shading represents the values

66

significantly less. Comparisons of the detected penetration depths in Figure 4.21-C show that the threshold ratio of 0.4 consistently tracks the depth of the vertical velocity cells seen in Figure 4.21-A. 0.4 threshold ratio was used to define the penetration depth in the remaining analysis.
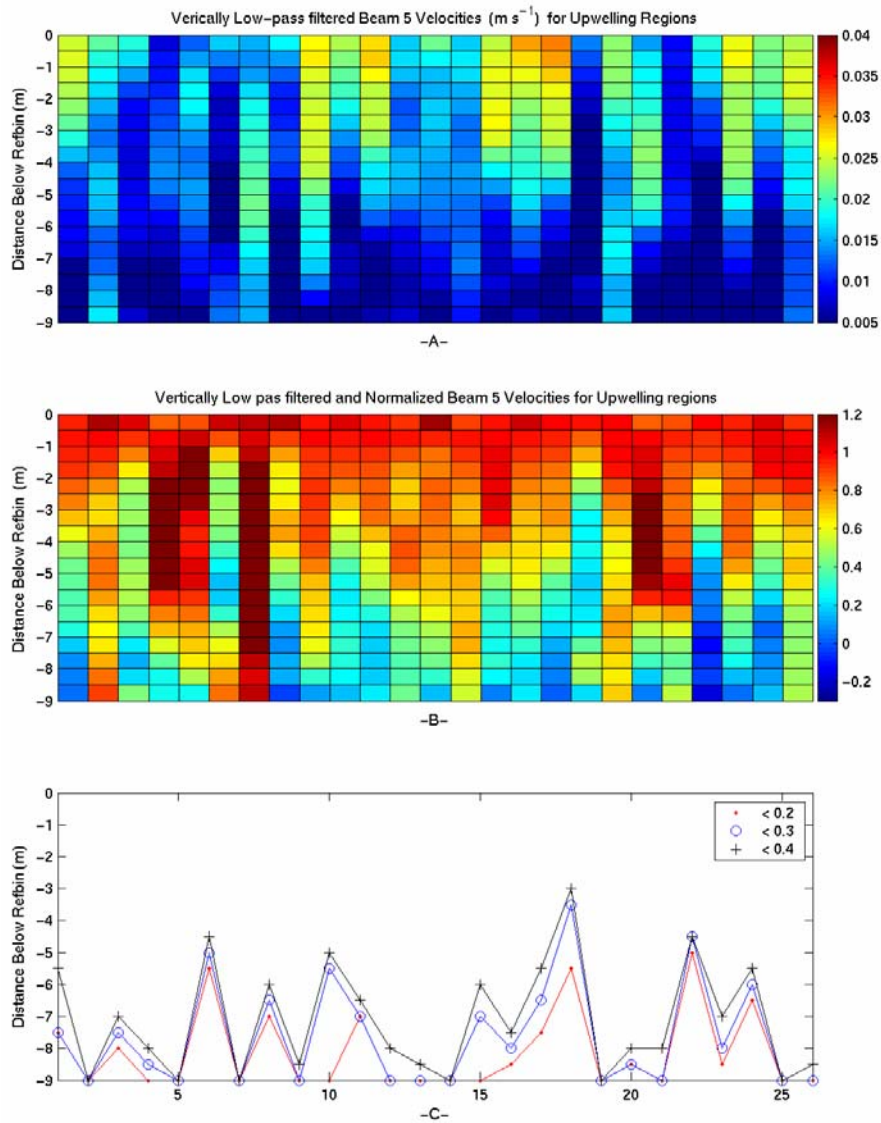
Figure 4.22   Detection of penetration depths for the upwelling regions related to Langmuir circulations between the days 352 and 352.0833 (two-hour period). Panel A is vertically 4 m low-pass filtered beam 5 vertical velocities. Panel B is normalized beam 5 vertical velocities by Equation 4.2, the reddish shading color indicates the velocities similar to the near surface velocities while the bluish shading indicates weaker velocities than the near-surface velocities and Panel C shows the penetration depths for the upwelling regions after ratio thresholds.

67

The same threshold ratio of 0.4 was chosen for finding upwelling cell depth as seen in Figure 4.22.

I. SPACING BETWEEN UPWELLING / DOWNWELLING REGIONS

Horizontal spacing between successive upwelling regions or downwelling regions can be used to estimate the horizontal length scale of the Langmuir circulations described in section II.B. For much of the time at the ASIT site, Langmuir circulations were advected by strong east-west tidal currents. The four-beam solution of horizontal velocity components and the time difference between successive upwelling regions or downwelling regions were used to calculate the spacing during periods where the advective speed exceeded 0.1 ms^{-1}.
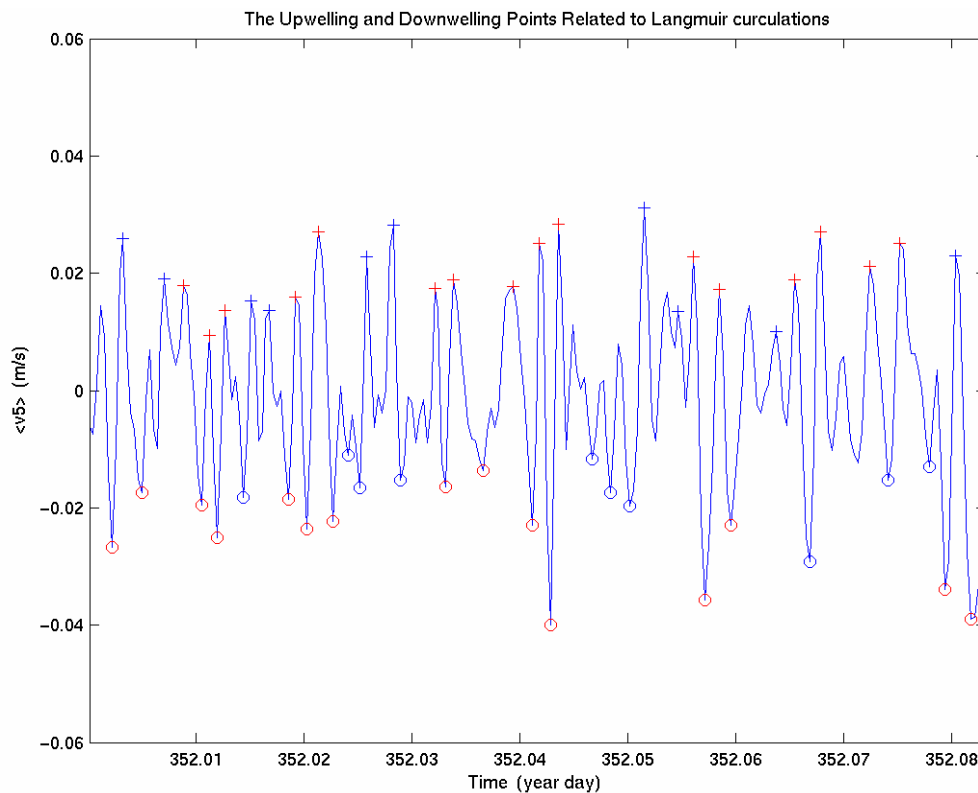
Figure 4.23   Successive upwelling (red cross) and downwelling (red circles) regions between the day 352 and 382.0833 (two hour period)

For example, in Figure 4.23 the spacing for the downwelling regions was calculated between the consecutive red circles by multiplying the time difference between them with horizontal advection mean velocity. The spacing for the upwelling regions was calculated between the consecutive red crosses with the same method. This method requires a fairly

68

uniform, discreet cell field to unambiguously define distinct successive upwelling and downwelling events. This is generally true under strong forcing conditions, but challenging in light wind / wave conditions.

THIS PAGE INTENTIONALLY LEFT BLANK

V. ANALYSIS AND RESULTS

Statistical relationships between the Langmuir circulation features and potential forcing mechanisms such as wind speed and waves Stokes drift were explored in this long time series observation. The tidally forced inner shelf site provided an opportunity to investigate the concurrent effects of a strong tidal boundary flow with a wide range of wind forcing conditions.
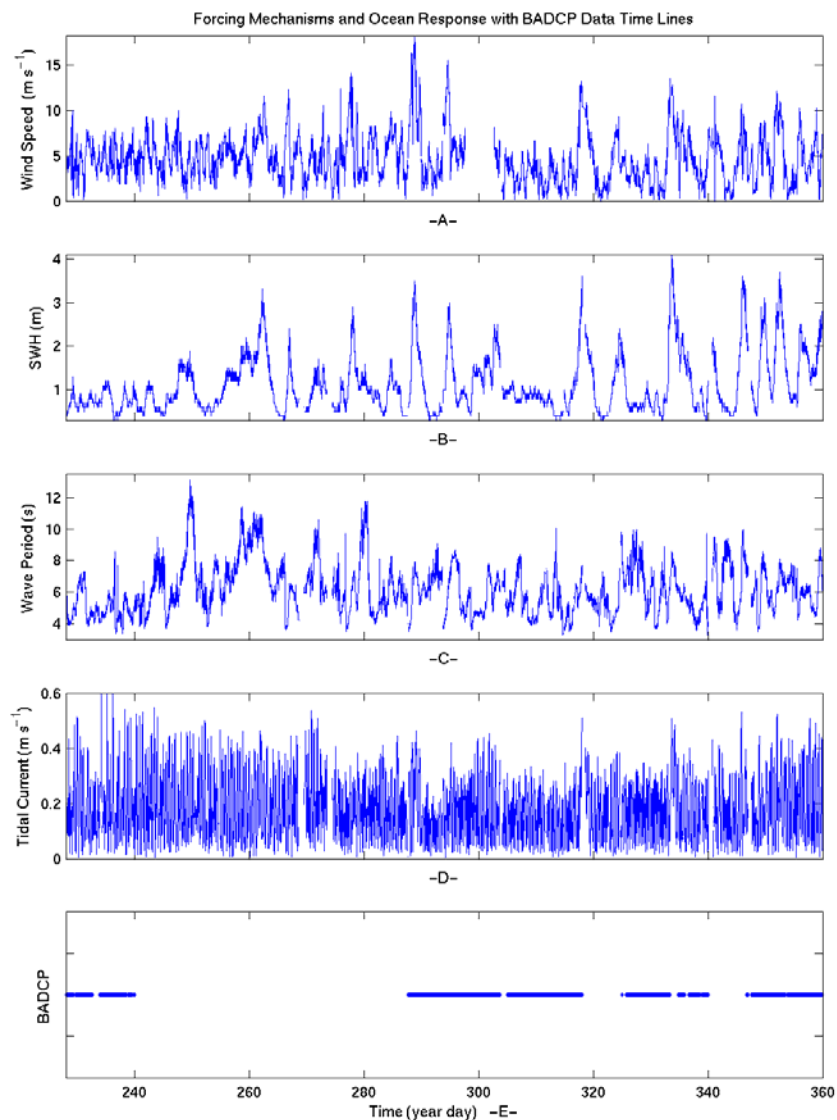
Figure 5.1   Wind speed (Panel A), wave parameters (Panel B and C) and tidal currents (Panel D) time series from MVCO with the BADCP data between the days 228 and 360 (Panel E) during CBLAST experiment. The gaps in BADCP data are due to a power outage.

Winds were measured 4 km north of ASIT at the southern shore of Martha's Vineyard, and directional wave spectra 1 km. north at 12 m depth to provide time series of surface forcing and wave condition at the BADCP site. Southerly winds provide long fetch conditions, whereas northerly winds result in short fetch conditions for the ASIT location due to blocking by Martha's Vineyard Island seen in Figure 3.3. The tidal currents shown in Figure 5.1-D are strong for the experiment region, and are dominantly in the alongshore (east-west) direction.

The surface boundary layer and the bottom boundary layers are generally decoupled in the summer time due to strong seasonal stratification, and Langmuir circulations characteristics are affected by this stratification. Surface cooling and strong storm events diminish the seasonal summertime stratification and couple the surface and bottom boundary layers in the fall and wintertime. The available BADCP data between days 228 and 240 are representative of summertime, and there are no significant storm events during this time (Figure 5.1). The BADCP data between the days 280 and 360 are in fall / wintertime conditions and span a series of strong storm systems.

In this study locally well-developed seas with long fetch winds under the weak stratification oceanic conditions were chosen as a focus for the analysis of Langmuir circulations. Locally well-developed seas represent increasing wave conditions with increasing wind speed in the experiment region without dominant influence of energetic pre-existing swell from the Atlantic. The cases meeting these criteria were selected between days 280 and 360 by plotting the wind speed time series, wind / wave direction time series, and time series of wave energy density spectrum.
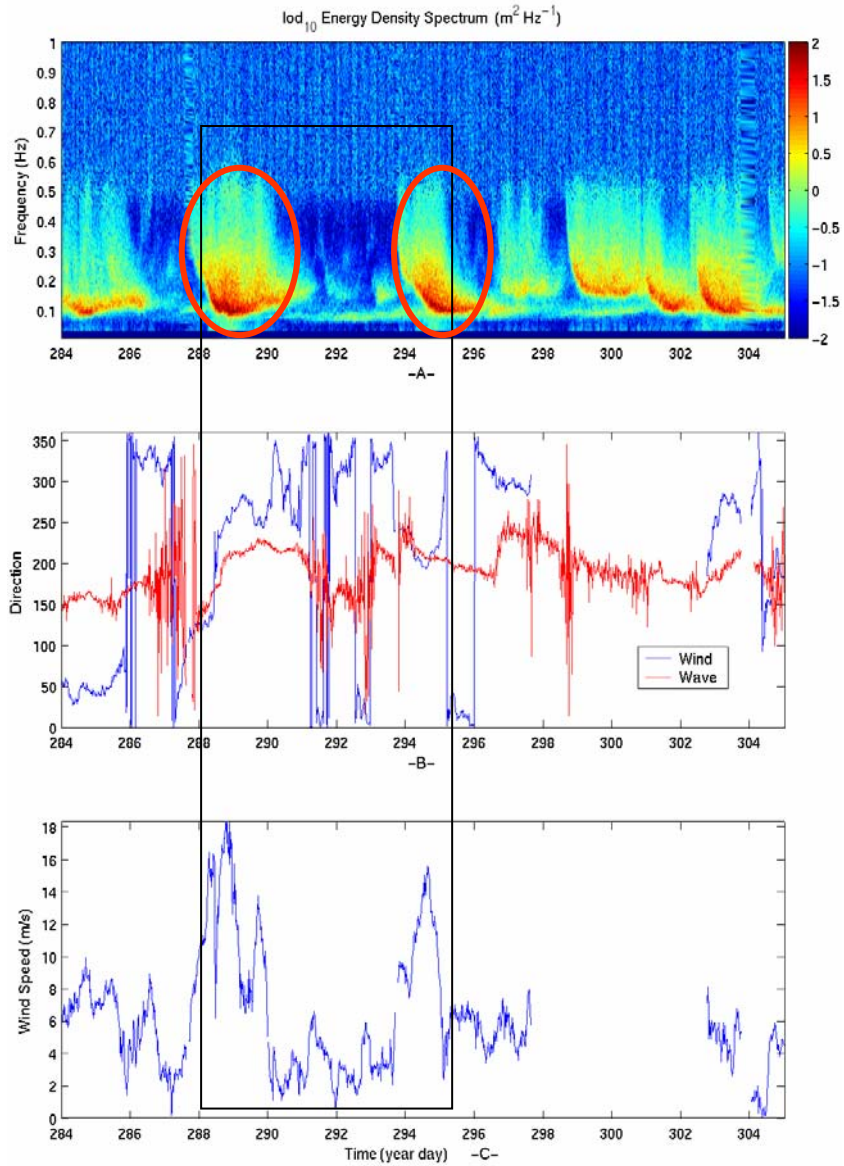
Figure 5.2   Panel A: Color plot of logarithmic scale wave energy density spectrum. Panel B: Wave and wind direction time series. Panel C: Wind speed time series between the year days 284 and 304. The region in the black square is the selected segment for this period of collected data and the region in the red circles represent typical wind-induced increasing wave field.

As the wind speed in Figure 5.2 panel B increases during year day 288, the wave spectrum evolves from short period local waves to fully-developed swell and sea conditions, as seen in the red circles in panel A. The wind reaches its maximum speed, 18 ms^{-1}, on the day 289 with the most energetic waves in the 6-10 second period band. After the day 289, the winds relax and the wave energy decreases. Wind speed is down to

73

2 ms^{-1} on day 291, and the wave energy shows a trend toward local, weakening, shortening period waves. After determining the locally developed sea conditions, long fetch conditions were determined in the wind direction time series (Figure 5.2-B). Southerly winds and waves were classified as long fetch. The black square is the time period when both these conditions were satisfied and defined a long-fetch, local wave field data segment.
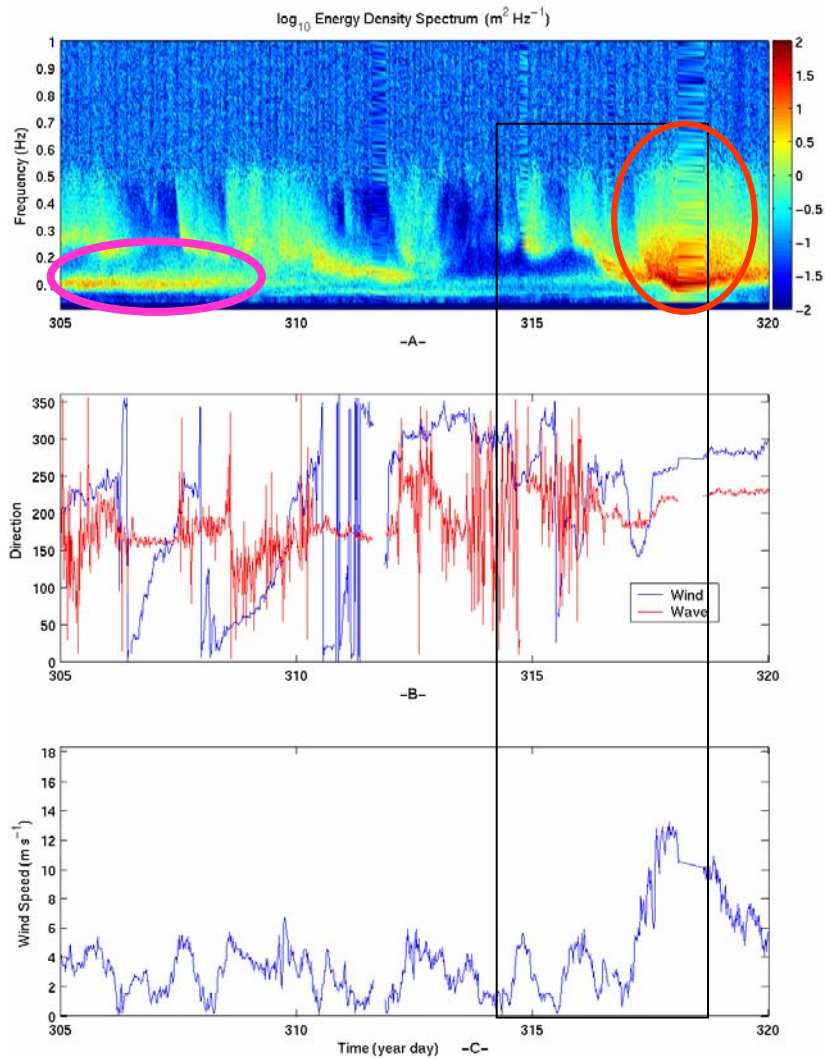
Figure 5.3   Panel A: Color plot of logarithmic scale wave energy density spectrum. Panel B: Wave and wind direction. Panel C: Wind speed time series between the year days 305 and 320. The Region in the black square is the selected segment for this period of collected data and the region in the red circle represents typical wind-induced, increasing wave field while the region in the purple circle represents the energetic swell coming from Atlantic Ocean.

74

The red circle in Figure 5.3-A starting on day 317 represents the locally developed seas with increasing wind speed. The region inside the purple circle indicates a period of high-energy swell coming from Atlantic Ocean. The region inside the black square is the selected segment between the days 314.5 and 319. The wind speed increases up to 14 ms^{-1} during this time period.
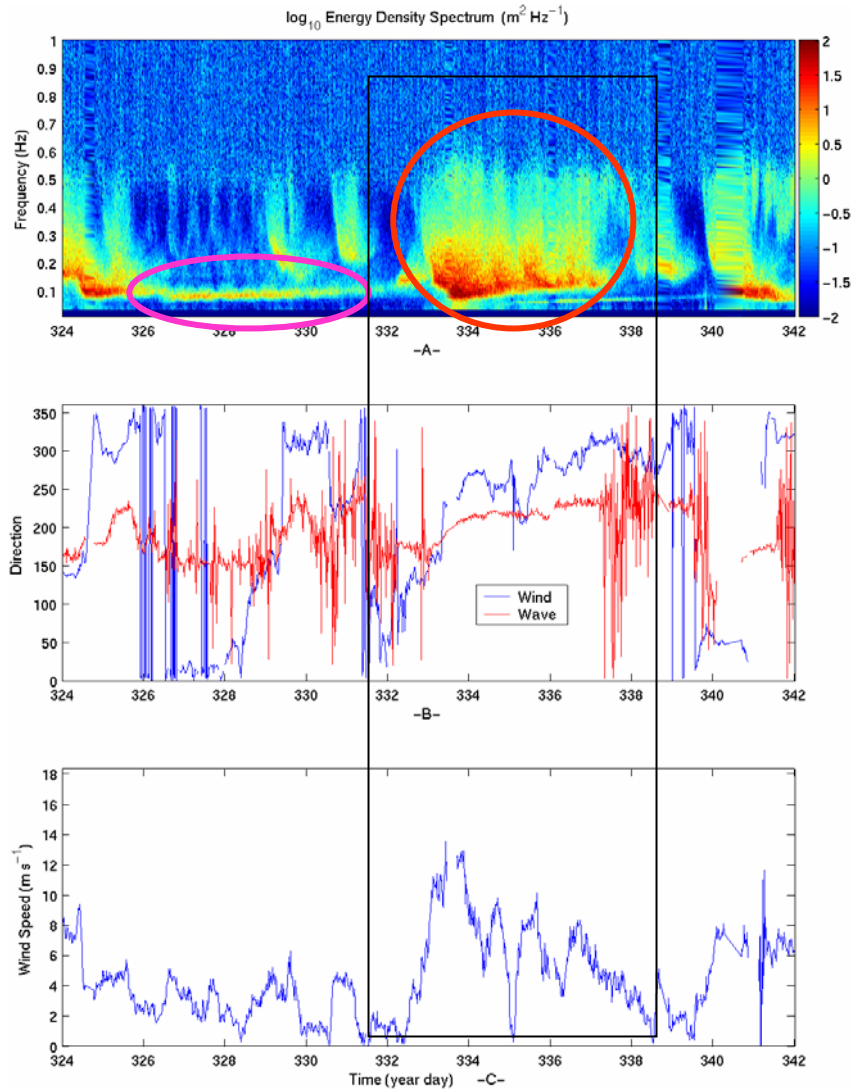
Figure 5.4   Panel A: Color plot of logarithmic scale wave energy density spectrum. Panel B: Wave and wind direction. Panel C: Wind speed between the year days 324 and 342. The region in the black square is the selected segment for this period of collected data and the region in the red circle represents typical wind-induced increasing wave field while the region in the purple circle represents the energetic swell coming from Atlantic Ocean.

The interval between the year days 331.5 and 338.5 was chosen for the time period shown in Figure 5.4. Swell from the Atlantic is very energetic between the days 326 and 331.5 (Figure 5.4-A). Wind speed starts to increase to 12 ms^{-1} on day 332, and decreases steadily between days 336.5 and 338.5.
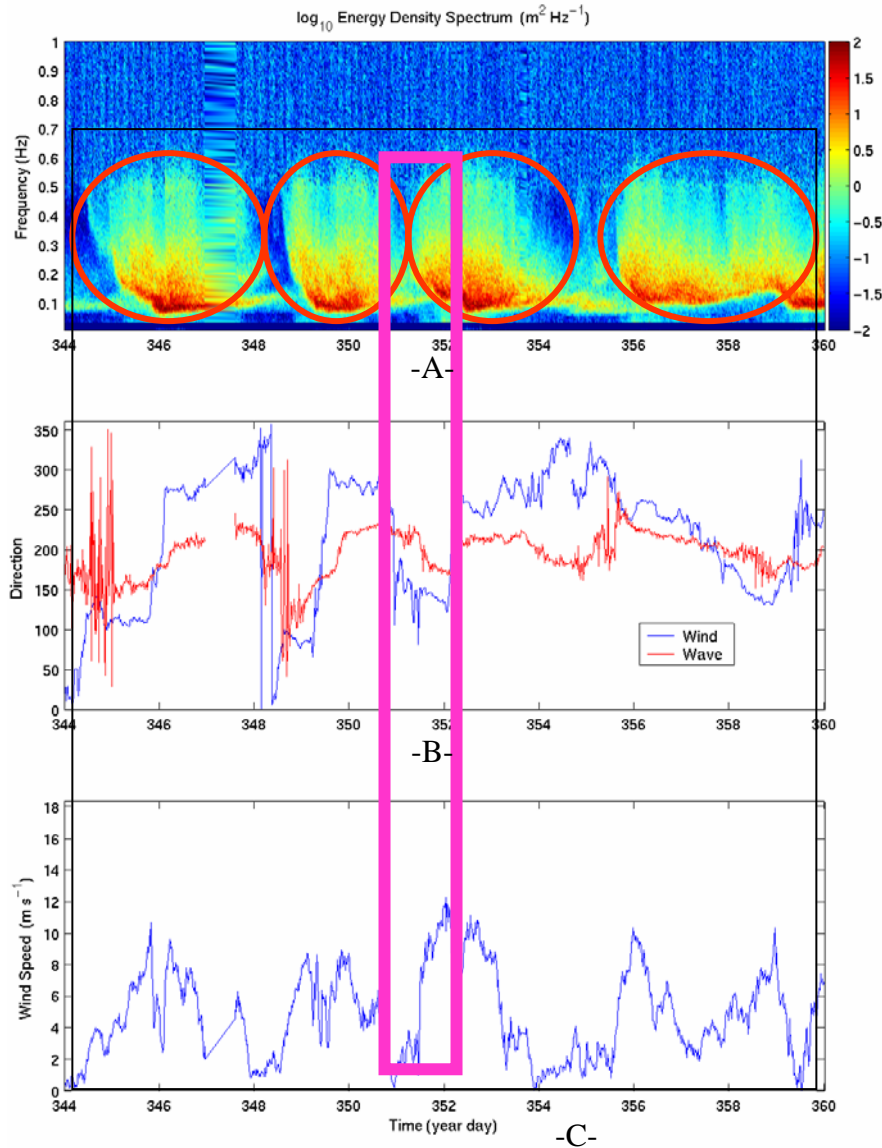

Figure 5.5   Panel A: Color plot of logarithmic scale wave energy density spectrum. Panel B: Wave and wind direction. Panel C: Wind speed between the year days 344 and 360. The region in the black square is the selected segment for this period of collected data and the region in the red circle represents a typical wind-induced increasing wave field. The purple square region is a one-day period between the days 351 and 352 for stratification and shear profile analysis.

There are four clear long fetch storm cases in the day 344 to 360 interval seen in Figure 5.5, so the whole time period shown in Figure 5.5 was chosen for the long-fetch, low-stratification analysis. The purple region represents a one-day period when the wind speed increased from 1 ms^{-1} to 12 ms^{-1} between the days 351 and 352, and the current profile was examined as follows for this period.
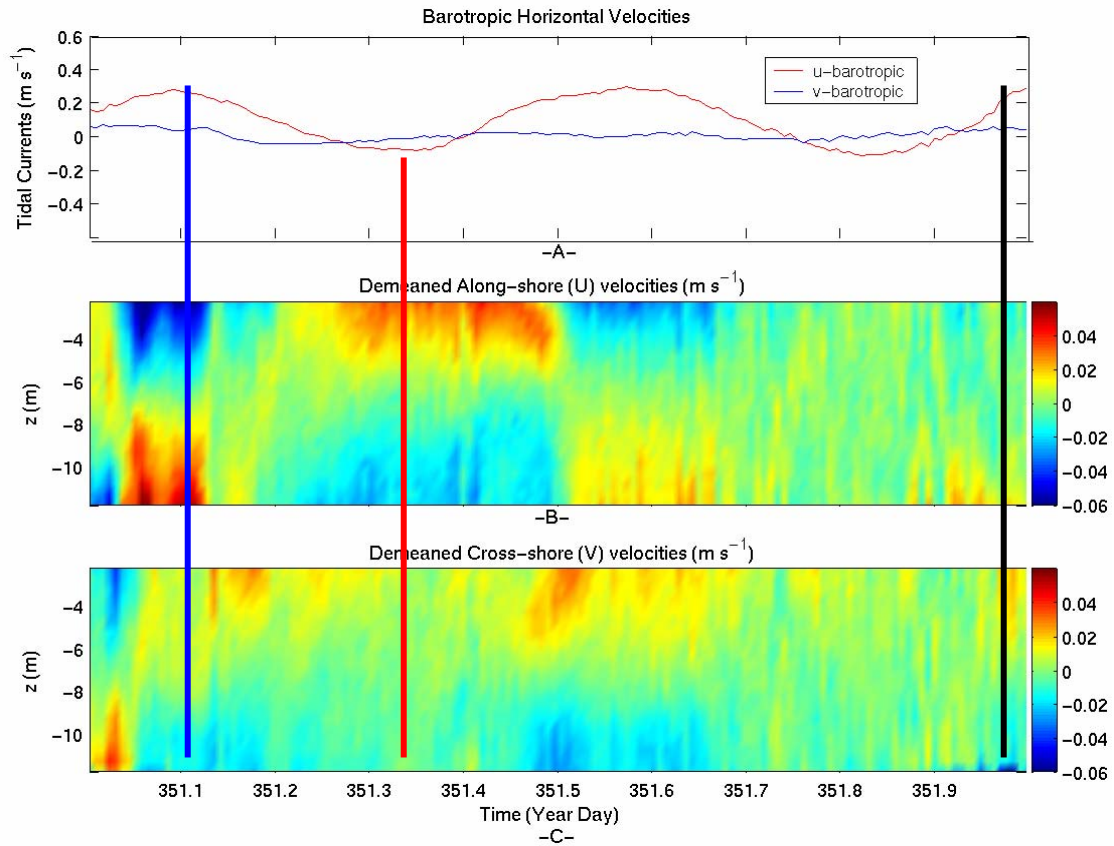
Figure 5.6   Panel A: Vertically averaged barotropic alongshore (u) and cross-shore velocities (v). Panel B: Demeaned alongshore velocity profile through the water column. Panel C: Demeaned cross-shore velocity profile through the water column between the year days 351 and 352. Vertical blue line represents the condition of low wind and high tidal current during 351.1 and 351.14, vertical red line represents the condition of low wind and low tidal current during 351.32 and 351.36, vertical blue line represents the condition of high wind and tidal current during 351.96 and 352.

Vertical mean horizontal velocity time series and demeaned current profile time series are shown in Figure 5.6 with along-shore (east-west) tidal currents greater than cross-shore tidal currents at this site for a 24 hour period. During this time wind speed before the 351.6 is between 0 and 2 ms^{-1}, then increases to 12 ms^{-1} on day 352. Velocity

differences between the upper and bottom ocean are clearly seen in the demeaned velocity profiles in Figure 5.6-B and Figure 5.6-C, under low wind conditions (before day 316.5). Once the wind speed starts to increase after day 351.5, the pre-existing velocity shear rapidly weakens through the water column. This suggests that the wind homogenizes existing shear under these conditions. During cold weather, strong wind forcing conditions in the fall at this site, the water column is largely unstratified. During these conditions, the strong tidal currents are likely to form a 'law of the wall' logarithmic velocity profile with constant stress across the water column. This hypothesis was tested by plotting a logarithmic depth scale versus horizontal velocities in the water column for a combination of high and low winds and tidal currents.
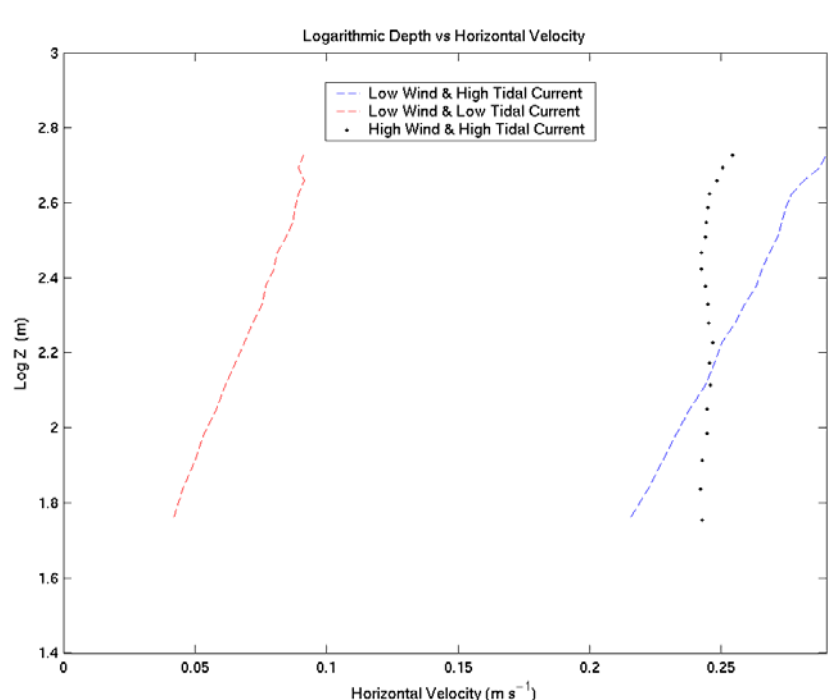
Figure 5.7   Logarithmic Depth scale and horizontal velocity plots to obtain the stratification for three different conditions described in Figure 5.6. The colors are the same with the colors used in Figure 5.6 to represent the three different conditions.

The linear decrease of horizontal velocities with respect to logarithmic scale indicates a well-developed constant stress flow at low wind speeds. The dashed red and blue lines in Figure 5.7 represent the low wind speed conditions, while the black dotted line shows high wind condition, using the same colors in Figure 5.6. The low wind and low current

condition profile in Figure 5.7 decreases almost linearly through the water column, indicating an unstratified weaker tidal boundary layer. After wind speed increases to 12 ms^{-1} the dotted black line in Figure 5.7 shows this log-layer to have been replaced with a low shear, homogenized water column.
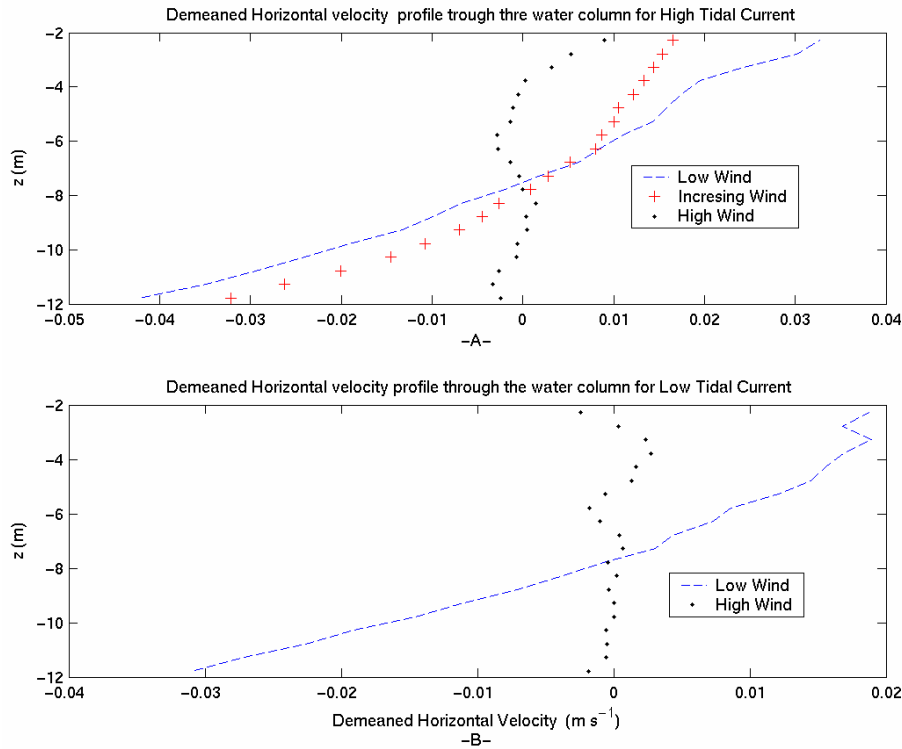
Figure 5.8   Demeaned Horizontal velocities vs. Depth. Panel A: The demeaned horizontal velocity profile through the water column for high tidal currents (greater than 0.1 ms^{-1}). Panel B: The demeaned horizontal velocity profile for low tidal currents (less than 0.1 ms^{-1}).

These profiles are shown as demeaned linear z profiles in Figure 5.8 to emphasize the differences in shear structure as wind increases. In Figure 5.8-A with high tidal current, the wind speed for the blue dashed line shear profile is about 2 ms^{-1} between the days 351.1 and 351.14 while the wind speed for red crossed line shear profile is about 8 ms^{-1} between the days 351.55 and 351.59. Demeaned horizontal velocity shear with 2 ms^{-1} wind speed is greater than demeaned horizontal velocity shear with 8 ms^{-1} wind speed, while the dotted black line shear profile with 12 ms^{-1} wind shows very low velocity shear for the time between the days 351.96 and 352. In Figure 5.8-B with low tidal currents, the blue dashed line demeaned horizontal velocity shear profile between the days 351.32 and

351.36 with 2 ms^{-1} wind speed is much greater than the dotted black line demeaned horizontal velocity shear profile between the days 351.82 and 351.86 with 10 ms^{-1} wind speed. For both high tidal and low tidal current cases, the bottom boundary layer shear profiles in the water column rapidly decrease with increasing wind speed while surface forced mixing processes increase.
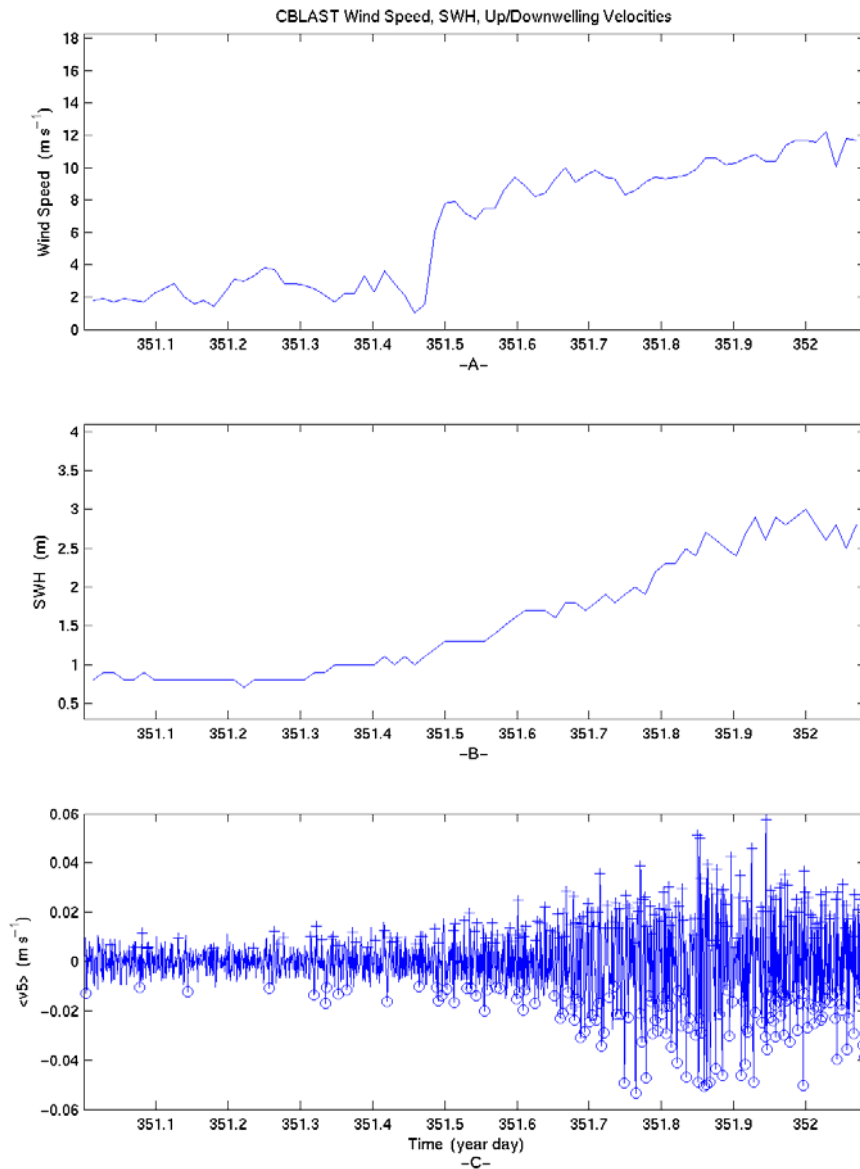
Figure 5.9   Panel A: Time series of wind speed. Panel B: Significant wave height (SWH) time series. Panel C: Detected downwelling / upwelling regions related to Langmuir circulations responsible for the mixing process between the days 351 and 352

A one-day time series of wind speed (Figure 5.9-A) and significant wave heights (Figure 5.9-B) show increasing wave heights with the increasing wind speed. The low wind speed and low significant wave heights before the day 351.5, result in low levels of wind and wave interaction, hence the amount of the detected downwelling / upwelling velocities related to the Langmuir circulations is small. After day 351.5, the wind and wave interaction effect is increasing, and creating more Langmuir circulations as shown in Figure 5.9-C above our detection thresholds. We hypothesize that the homogenizing process across the water column after 351.5 is due to the increasing strength of the Langmuir circulations acting in concert with surface shear-driven turbulence.

The days between 288 and 295.5; 314.5 and 319; 331.5 and 338.5; 344 and 360 were selected to represent unstratified, locally well-developed seas with southerly, long fetch wave / wind conditions. It is expected that strong Langmuir turbulence occurs for these time periods. Langmuir number is a parameter to predict if the Langmuir turbulence is strong or not. The Langmuir number was first described by Leibovich (1977a) as shown in Equation 2.38. McWilliams et al (1997) parameterized the turbulent Langmuir number as,

$$La_t = (u_* / U_s)^{1/2} \tag{5.1}$$

where u_* is the water friction velocity and the U_s is the surface Stokes drift velocity. Water friction velocity is parameterized through a widely used empirical drag coefficient by Large and Pond (1981) as

$$
\begin{aligned}
u_* &= \left(\tau / \rho_{ocean}\right)^{1/2} \\
\tau &= \rho_{air} C_D u_{10}^2 \\
C_D &= \left(4.9 \times 10^{-4} + 6.5 \times 10^{-5} \times u_{10}\right)
\end{aligned}
\tag{5.2}
$$

where τ is the wind stress at the sea surface, C_D is the drag coefficient, u_{10} is the wind speed measured at 10 m above the sea surface and ρ is the density. The surface Stokes drift is defined by Philips (1977) in Equation 5.3.

$$U_s = \sigma k a^2$$
$$\sigma = (gk)^{1/2}$$

(5.3)

where k is the dominant swell wave number, a is the wave amplitude, g is the gravitational acceleration and σ is the particular wave frequency associated with dominant swell wave number.

If the surface Stokes drift velocity is low for a given wind forcing, the turbulent Langmuir number will be large and shear turbulence will dominate. The smaller the turbulent Langmuir number (stronger U_s), the stronger the Langmuir circulation. Li et al (2004) defined a turbulent Langmuir number of approximately 0.7 for the transition from shear turbulence to Langmuir turbulence.
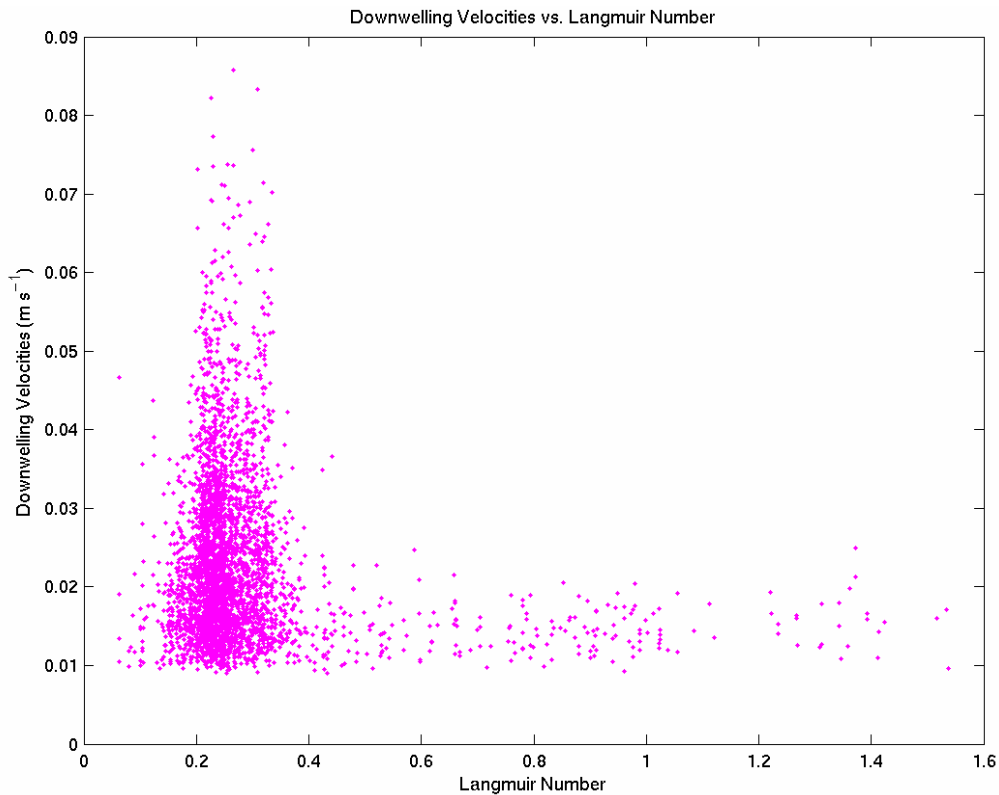
Figure 5.10   Downwelling velocities and Langmuir number relationship between the days 288 and 295.5; 314.5 and 319; 331.5 and 338.5; 344 and 360.
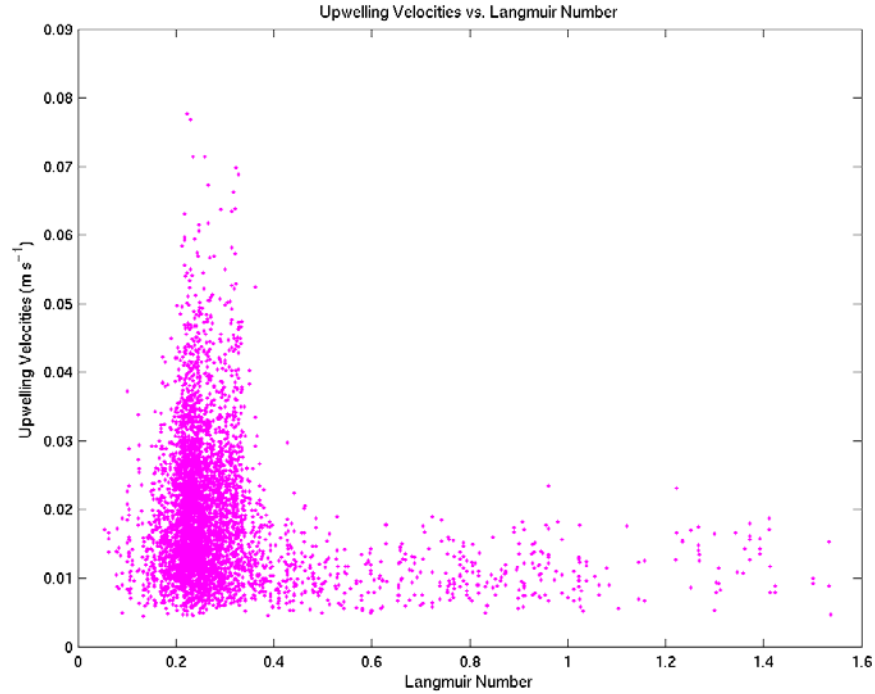
Figure 5.11   Upwelling velocities and Langmuir number relationship between the days
288 and 295.5; 314.5 and 319; 331.5 and 338.5; 344 and 360.

Both Figure 5.10 and 5.11 show a strong increase of detected downwelling / upwelling velocities largely occurring with a range of Langmuir numbers from 0.1 to 0.4, which confirms that the Langmuir turbulence is strongest for low Langmuir numbers where the wave Stokes drift is high. The velocities shown with the Langmuir number greater than 0.5, largely represent short fetch within the "long fetch" time series. In these cases, surface shear stress dominates over Langmuir turbulence. The period between days 291 and 293 is very good example for these cases (Figure 5.12 and Figure 5.13). In Figure 5.2-C, winds are northerly and wind speed is ~2 ms^{-1} on day 291 and increases up to 7 ms^{-1}, then decreases to 1 ms^{-1} between the days 291 and 292, then starts to increase and reaches 6 ms^{-1} on day 293. Under short fetch conditions the Langmuir number is greater, and the vertical velocities are lower for this time period. Li et al (2004) suggested a Langmuir number of 10, which results in a strong shear turbulence and very small Langmuir turbulence, but this is not seen for the forcing conditions seen here.
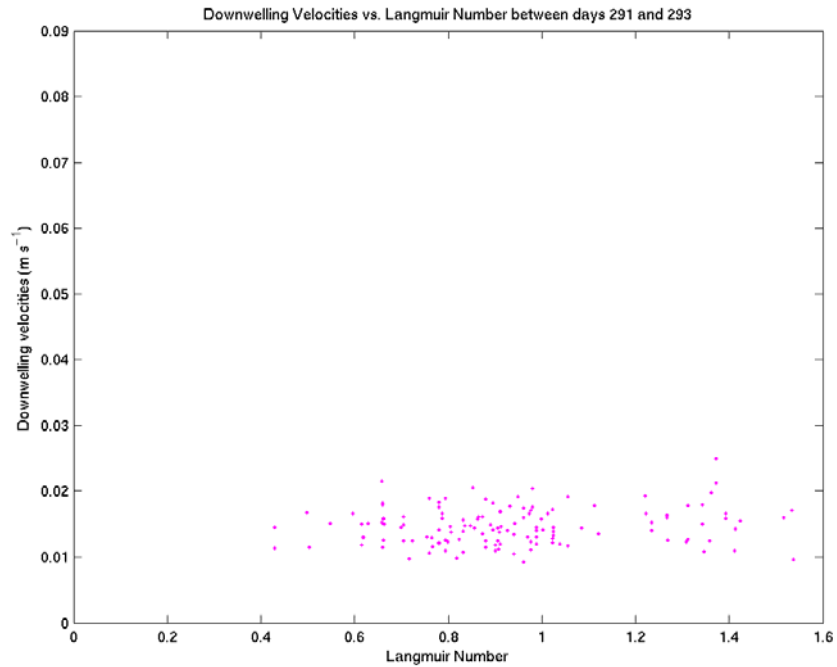
Figure 5.12   Downwelling velocities with Langmuir number between the days 291 and 293 with northerly winds (short fetch)
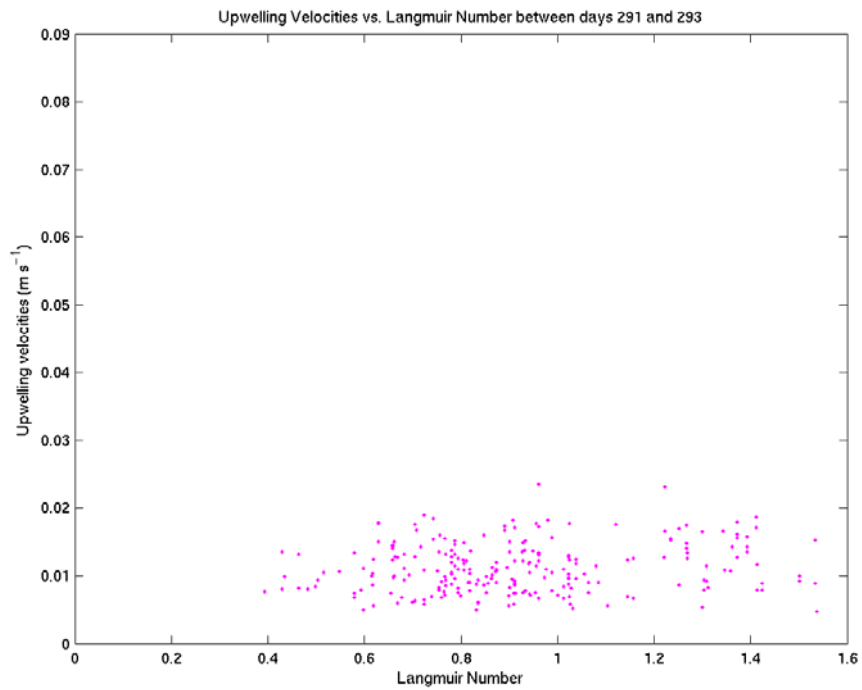
Figure 5.13   Downwelling velocities with Langmuir number between the days 291 and 293 with northerly winds (short fetch)
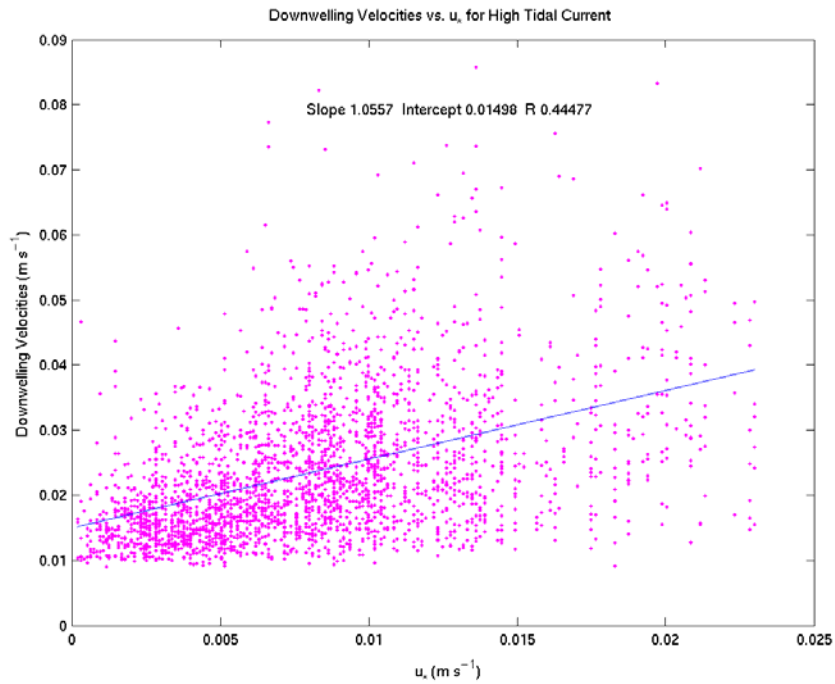
Figure 5.14   Downwelling velocities and friction velocity regression plot for tidal currents greater than 0.1 ms^{-1} for the selected days.
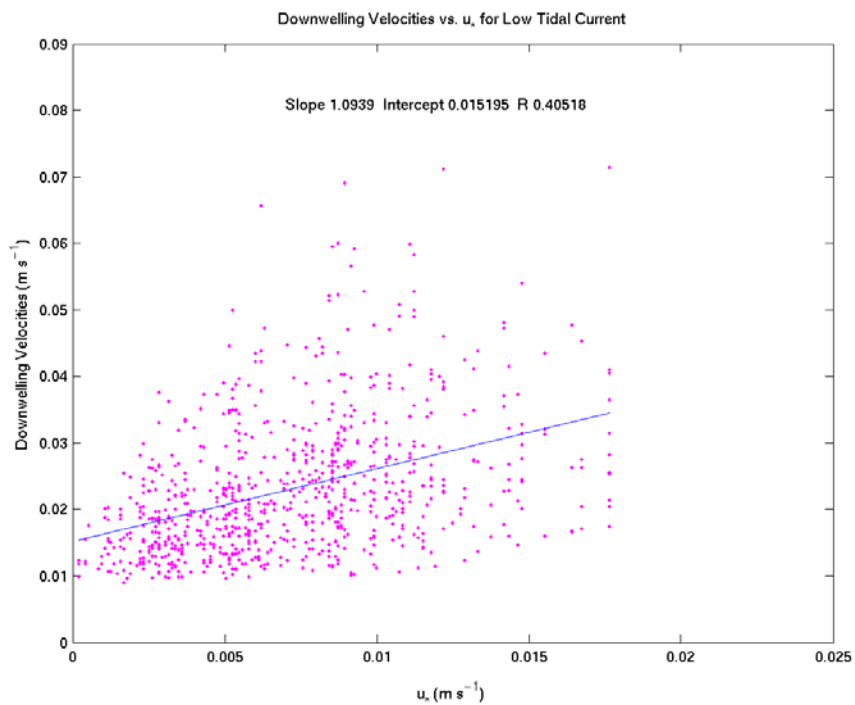
Figure 5.15   Downwelling velocities and friction velocity regression plot for tidal currents less than 0.1 ms^{-1} for the selected days.
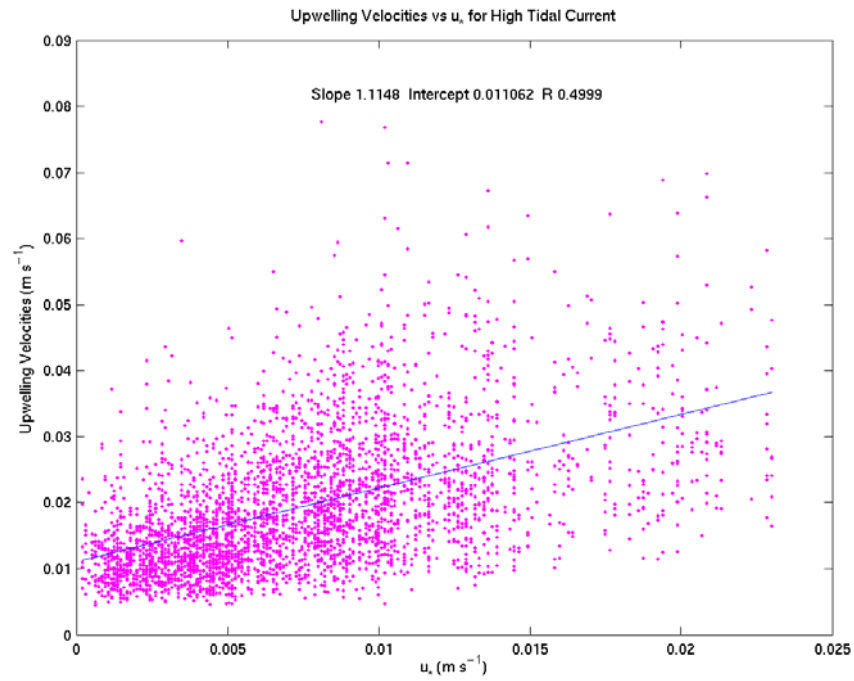
Figure 5.16   Upwelling velocities and friction velocity regression plot for tidal currents greater than 0.1 ms^{-1} for the selected days.
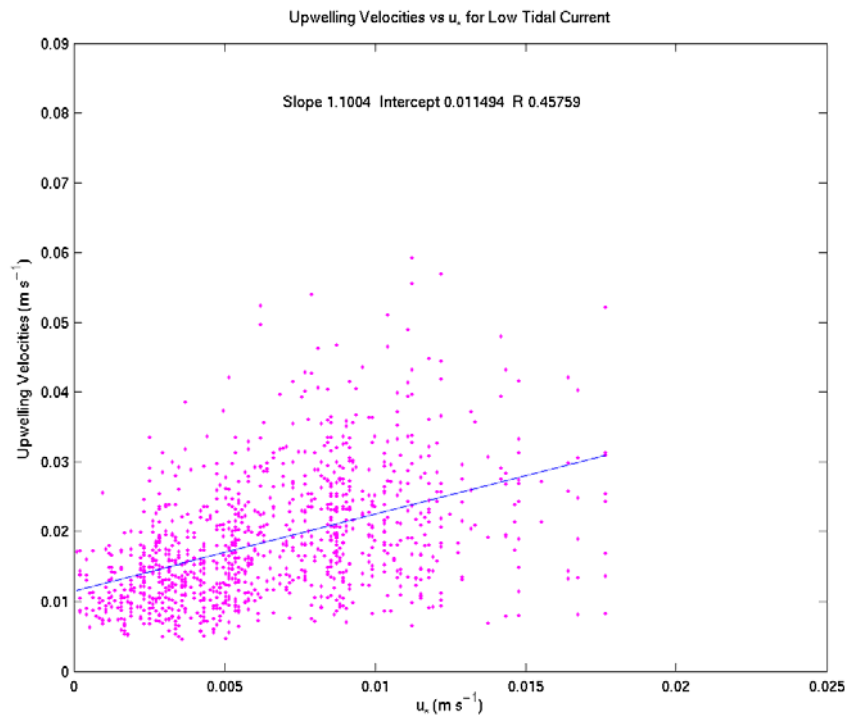
Figure 5.17   Upwelling velocities and friction velocity regression plot for tidal currents less than 0.1 ms^{-1} for the selected days.

Statistical relationships between the water friction velocity and downwelling / upwelling velocities for high tidal currents and low tidal current were examined for the

selected days to see whether the presence of a strong tidal boundary layer through the water column affected generation of Langmuir cells. Correlations between downwelling velocities and surface friction velocity are statistically significant for both high tidal currents and low tidal currents. In Figure 5.14 for high tidal current, the downwelling velocities increase with increasing friction velocity and the regression coefficient is 0.44 with a slope of 1.05. In Figure 5.15 for low tidal current, the regression coefficient is 0.41 with a slope of 1.09 between the downwelling velocities and friction velocity, suggesting no differences due to the presence of a strong tidal bottom boundary layer.

Similarly, upwelling velocities and friction velocities are statistically significant for both high tidal currents and low tidal currents. In Figure 5.16 for high tidal current, the upwelling velocities are increasing with increasing friction velocity and the regression coefficient is 0.50 with a slope of 1.1. In Figure 5.17 for low tidal current, the regression coefficient is 0.45 with a slope of 1.1 between the upwelling velocities and friction velocity.

The linear relationship found between the friction velocity and downwelling velocities is consistent with results of Leibovich (1983) shown in Figure 2.10. We also found a similar linear relationship for upwelling velocities in addition to his result. The slope of the regression line is ~1.07 for downwelling velocities while it is ~1.1 for upwelling velocities, which indicates that there is a slight asymmetry between them. Since wind and wind generated waves are responsible for the formation of these circulations, the strength of the circulations should increase with increasing forcing strength. The regression coefficients are not high, but we hypothesize that this is because of the wide range of scales of the Langmuir circulations within the water column for moderate and strong forcing. Langmuir (1938) and many others also observed that small-scale circulations exist within large-scale circulations.
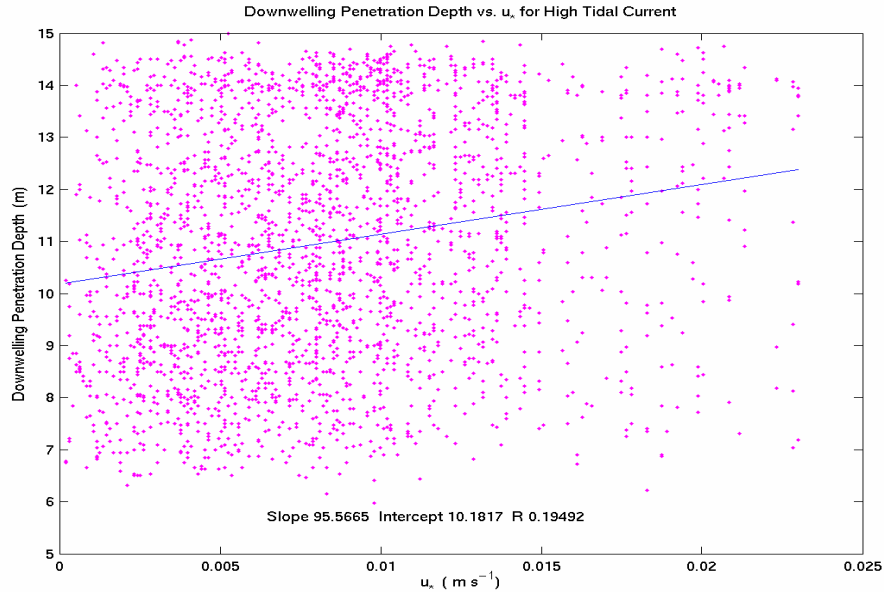
Figure 5.18   Downwelling Penetration Depths and friction velocity regression plot for tidal currents greater than 0.1 ms^{-1} for the selected days.

The relationship between downwelling penetration depths and the friction velocity is shown in Figure 5.16 with a regression coefficient of 0.19 and they are not statistically correlated. This confirms that penetration depth of the Langmuir circulations does not depend on the forcing mechanism but rather is related to water depth and stratification profiles at the site.
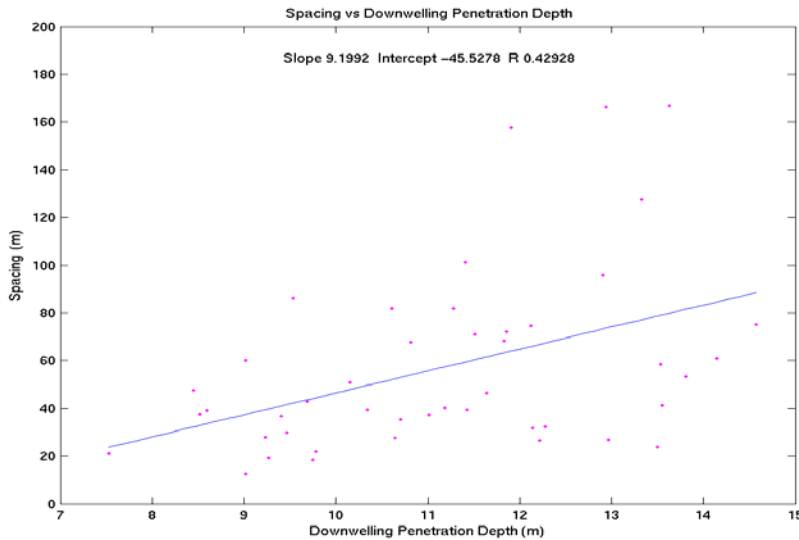
Figure 5.19   Downwelling penetration depth and spacing (between the downwelling regions) relationship for days 348 and 349; 351 and 352; 355 and 356, which represents increasing wind and wave forcing.

The correlation between cell spacing and penetration depth was found for both increasing wind speed and wave heights, and constant high winds and wave heights. The regression coefficient of 0.44 with a slope of 8.7 was found for increasing wave height and wind, which indicates a statistical correlation (Figure 5.19). Nevertheless, the same correlation was not found for the high constant wind speed and wave conditions which are representative of the older waves case with a small Langmuir number of ~ 0.3.
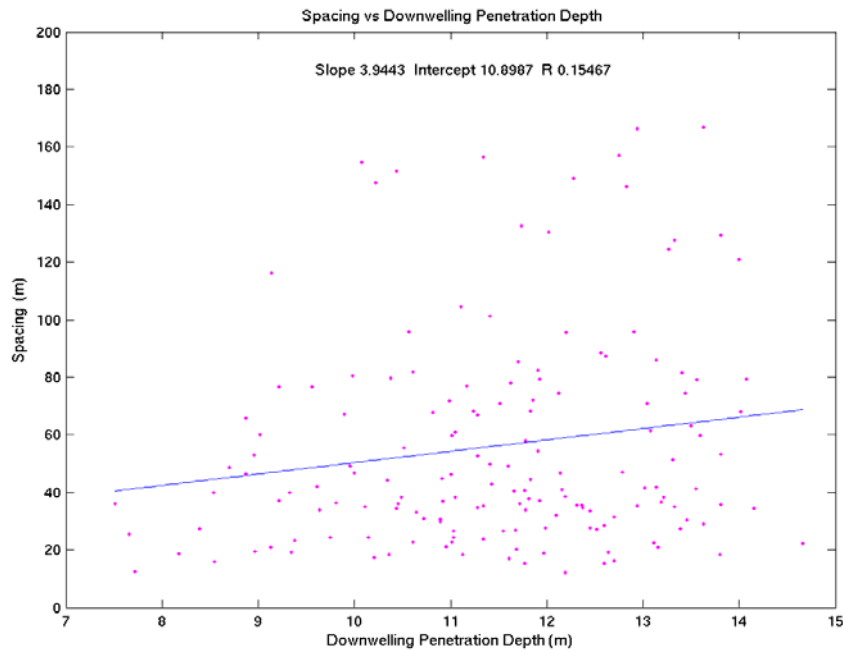
Figure 5.20   Downwelling penetration depth and spacing (between the downwelling region) relationship for the days selected for the days 349 and 350; 352 and 353; 356 and 357, which represents high wind speed and waves.

The regression coefficient of 0.15 in Figure 5.20 with slope of 4 indicates that there is not a significant correlation between spacing and downwelling penetration depths for high wind and wave conditions, again suggesting a wide range of cell scales for these conditions.

The detection of Langmuir circulations under stratified summer ocean conditions is complicated by the presence of strong internal waves. High vertical velocity internal solitons might have coherent vertical velocities like Langmuir circulations in the upper ocean. Evidence of this can be seen in the summer time velocity profiles between days

228 and 242. Strong velocity shear can be seen in a 24-hour demeaned current profile time series, shown in Figure 5.21 panel B and panel C.
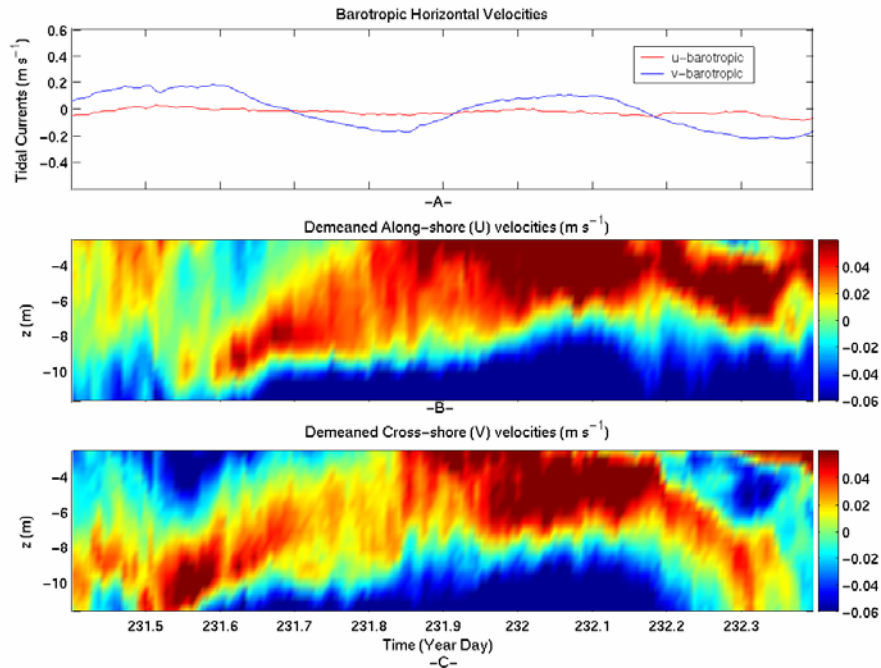
Figure 5.21   Panel A: Vertically averaged barotropic along-shore (u) and cross-shore velocities (v). Panel B: Demeaned along shore velocity profile through the water column. Panel C: Demeaned cross-shore velocity profile through the water column between the year days 231.4 and 232.4 during the summer time under strong stratification condition.

The wind speed is up to 8 ms^{-1}, but mixing is constrained to the upper few meters by strong stratification during this time period. The internal solitons having strong and coherent velocities are shown in Figure 5.22 by black circles. These were detected as Langmuir circulations (Figure 5.22–E). The analysis of Langmuir circulations detected under these conditions may give inaccurate results. For example, we found penetration depths down to 12 meters for detected upwelling / downwelling events in Figure 5.22–E, which are unlikely for 16.5 m depth of water with strong summer stratification. From Figure 5.21–B, the penetration depths of the Langmuir circulations should be a maximum of 3 to 5 m. Shallow Langmuir circulations constrained by near-surface stratification are not well resolved by the five beam BADCP and analysis techniques used in this study due to the co-existing strong internal solitons during the summer time.

90
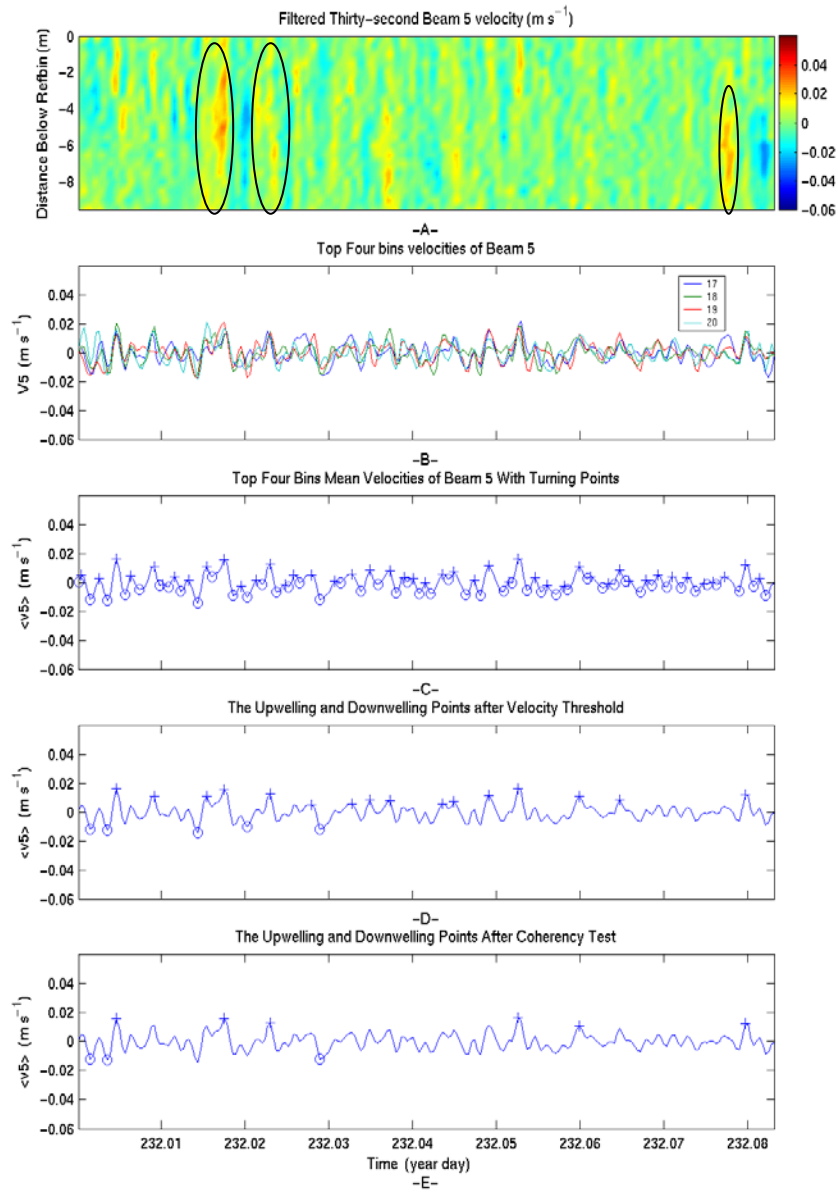
Figure 5.22   Panel A: Vertical velocities trough the water column. Panel B: Upper four bin vertical velocities. Panel C: Vertical mean of the velocities in panel B and all the upwelling (+) / downwelling (-) events. Panel D: Remaining upwelling / downwelling events after velocity thresholds. Panel D: Detected upwelling / downwelling events as Langmuir circulations between the days 232 and 232.0833. The black circles in Panel A are internal solitons, which are detected as Langmuir circulations.

THIS PAGE INTENTIONALLY LEFT BLANK

VI. CONCLUSIONS

Analyses of detailed water column velocity profiles for Langmuir circulations at an inner shelf site focused on long-fetch, unstratified water column with locally developed sea conditions. A detection algorithm for upwelling / downwelling velocities due to Langmuir circulations was created using high-resolution vertical velocity profiles from a five beam BADCP deployed during CBLAST-LOW at the ASIT research tower south of Martha's Vineyard.

The observations show that a wind-forced surface layer that generates strong Langmuir circulations greatly reduces water column shear arising from a tidally forced bottom boundary layer. Langmuir numbers were found between 0.1-1.5 for the time period of detected upwelling / downwelling velocities of Langmuir circulations, but the strongest vertical velocities were found with the Langmuir number of 0.1 to 0.4. This is consistent with the modeling results of McWilliams et al (1997), who found Langmuir number 0.3 most favorable for Langmuir circulations to develop. The short fetch conditions with Langmuir number greater than 0.5 have weaker vertical velocities than the long fetch conditions with Langmuir number less than 0.5. The Langmuir circulation effects on the mixing processes increase with increasing wind speed and wave heights.

The number and strength of Langmuir circulations increase with increasing wind speed and wave heights. Downwelling velocities were found from 0.01 to 0.08 ms^{-1}, while upwelling velocities were found from 0.05 to 0.07 ms^{-1} with a small difference, which indicates a small asymmetry between them.

The regression coefficients found between water friction velocity and both downwelling / upwelling velocities show that Langmuir circulation strength is statistically correlated with the joint surface stress and Stokes drift forcing mechanisms. The same correlations were found with high tidal and low tidal current conditions, suggesting that there is no significant effect from the strong tidal boundary layer on the formation of Langmuir cells. Co-existence of multiple scale Langmuir circulations results in low regression coefficients (i.e. from ~ 0.4-0.5), but the regressions still represent a statistically significant correlation.

The penetration depths of detected circulations were found to be from 6 to 14 meters and independent of the forcing strength. Langmuir spacing between the cells was found to be from 10 to 160 m, and a statistically significant regression coefficient of 0.44 was found between the spacing and penetration depths for increasing wind speed and wave heights. In contrast, the statistical correlation decreased to 0.15 for constant high wind and wave conditions with small Langmuir number.

Langmuir cells are energetic, vertically coherent, large horizontal scale circulations within the ocean surface layer that act to eliminate vertical gradients of current and other properties. Improved parameterizations of Langmuir circulation are being investigated in collaboration with ongoing LES modeling by Jim McWilliams and Ming Su.

LIST OF REFERENCES

1.   Assaf, G., R. Gerard, and A. L. Gordon . 1971 Some mechanisms of oceanic mixing revealed in aerial photographs. *J. Geophys. Res.* 76:6550-6572

2.   Craik, A. D. D. 1970. A wave-interaction model for the generation of windrows. *J. Fluid Mechanics.* Vol. 41, 801-821

3.   Craik, A. D. D. 1977. The generation of Langmuir circulations by an instability mechanism. *J. Fluid Mechanics*. 81: 209-223

4.   Craik, A. D. D. 1982a. The drift velocity of water waves . *J. Fluid Mech.* 116: 187-205

5.   Craik, A. D. D., and S. Leibovich. 1976. A rational model for Langmuir circulations. *J. Fluid Mechanics* vol. 73, part 3, 401-426

6.   Csanady, G. T. 1965. Windrow studies. *Report No. PR26,* Great Lakes Inst., Univ. Toronto, Ont. 82 pp

7.   Faller, A. J. 1964. The angle of windrows in the ocean. *Tellus* 16: 363-370

8.   Faller, A. J. 1981. The origin and development of laboratory models and analogues of the ocean circulation. In *Evolution of Physical Oceanography*, ed. B. A. Warren, C. Wunsch, 16: 462-479

9.   Faller, A. J., and E. A. Caponi 1978. Laboratory studies of wind-driven Langmuir circulations. *J. Geophys. Res.* 83: 3617-3633

10.   Faller, A. J., and A. H. Woodcock. 1964. The spacing of windrows of Sargassum in the ocean. *J. Mar. Res.* 22: 22-29

11.   Filatov, N. N., S. V. Rjanzhin, and L. V, Zaycev. 1981. Investigation of turbulence and Langmuir circulation in Lake Ladoga. *J. Great Lakes Res.* 7: 1-6

12.   Gammelsrod, T. 1975. Instability of Couette flow in a rotating fluid and origin of Langmuir circulations. *J. Geophys. Res.* 80: 5069-5075

13. Garrett, C. J. R. 1977. Generation of Langmuir circulations by surface waves – a feedback mechanism. *J. Mar. Res.* 34: 117:130

14. Harris, G. P., and J. N. A. Lott. 1973. Observations of Langmuir circulations in Lake Ontario. *Limnol. Oceanogr.* 18: 584-589

15. Ichiye, T. 1967. Upper ocean boundary-layer flow determined by dye diffusion. *Phys. Fulids* 10: 270-277

16. Kenny, B. C. 1977. An experimental investigation of the fluctuating currents responsible for the generation of windrows. *PhD thesis. Univ. Waterloo, Ont.* 163 pp

17. Kraus, E. B. 1967. Organized convection in the ocean surface layer resulting from slicks and wave radiation stress. *Phys. Fluids* 10: 294-297

18. Langmuir, I. 1938. Surface motion of water induced by wind. *Science* 87: 119-123

19. Large, W.G. and S. Pond, 1981. Open Ocean Flux Measurements in Moderate to Strong Winds, *J. of Phys. Oceanography*, 11: 324-336

20. Leibovich, S. 1977a. On the evolution of the system of wind drift currents and Langmuir circulations in the ocean. Part 1. Theory and the averaged. *J. Fluid Mech.* 79: 715-743

21. Leibovich, S. 1977b. Convective instability of stably stratified water in the ocean. *J. Fluid Mech.* 82: 561-585

22. Leibovich, S. 1983. The form and dynamics of Langmuir circulations. *Ann. Rev. Fluid Mech.* 15:391-427

23. Leibovich, S., and S. K. Lele 1982. Thermocline erosion and surface temperature variabilty due to Langmuir circulations. *FDA Rep #82-07,* Sibley School Mech. and Aerosp. Eng., Cornell Univ., Ithaca, N.Y.

24. Leibovich, S., Paolucci, S. 1980a. The Langmuir circulation instabilty as a mixing mechanism in the upper ocean. *J. Phys. Oceanogr.* 10: 186-207

25.   Leibovich, S., and S. Paolucci 1980b.   Energy stability of the Eulerian – mean motion in the upper ocean to three-dimensioanal perturbations. *Phys. Fluids* 23: 1286-1290

26.   Leibovich, S., and S. Paolucci 1981. The instability of the ocean to Langmuir circulations. *J. Fulid Mech.* 102: 141-167

27.   Leibovich, S., and A. Tandon 1993. Three-dimensional Langmuir circulation instability in a stratified layer. *Journal of Geophysical Research: Oceans* 98:16,501-16, 507

28.   Leibovich, S., and D. Ulrich 1972. A note on the growth of small scale Langmuir circulations. *J. Geophys. Res.* 77: 1683-1688

29.   Li, M., and C. Garrett 1995. Is the Langmuir circulation driven by surface waves or surface cooling? *J. Phys. Oceanogr.* 25: 64-76

30.   Li, M., C. Garrett, and E. Skyllingstad 2004. A regime diagram for classifying turbulent eddies in the upper ocean, Accepted by *Deep Sea Research* Aug 2004

31.   Maratos, A. 1971. *Study of near shore surface characteristics of windrows and Langmuir circulation in Monterey Bay*. MS thesis. Naval Postgraduate school, Monterey ,CA

32.   McWilliams, J. C., P. P Sullivan, P. P., and C. Moeng 1997. Langmuir Turbulence in the Ocean. *J. Fluid Mech.* 334: 1-30

33.   Myer, G. E. 1969. A field investigation of Langmuir circulations. *Proc. 12th. Conf. Great Lakes res., Ann Arbor, Mich.*, pp 625-663.

34.   Myer, G. E. 1971. *Structure and mechanics of Langmuir circulations on a small inland lake*. PhD dissertation. State Univ. N.Y., Albany

35.   Philips, O. M. 1977. *Dynamics of the Upper Ocean*. Cambridge Univ. Press. 336 pp. 2nd . ed

36.   Plueddemann, A. J., Smith, J. A., Farmer D. M., Weller, R. A., Crawford, W. R., Pinkel, R., Vagle, S. and Gnanadesikan, A. 1996. Structure and variability of Langmuir circulation during the surface waves process program. J. Geophys. Res., 101: 3525-3543

37.   Pollard, R. T. 1977. Observations and theories of Langmuir circulations and their role in near surface mixing. *In A voyage of Discovery: George Deacon 70th Anniversary Volume*, ed. M. Angel, pp. 235-251 Oxford: Pergamon

38.   RDI BADCP technical manuals, Direct Reading and Self-Contained Broadband Acoustic Doppler Profiler Technical Manual

39.   Scott, J. T., G. E. Myer, R. Stewart, and E. G. Walther 1969. On the mechanism of Langmuir circulations and their role in the epilimnion mixing. *Limnol. Oceanogr.* 14: 493:503

40.   Smith, J. A. 1980. *Waves, currents, and Langmuir circulations.* PhD thesis. Dalhouise Univ., Halifax, N. S. 242 pp

41.   Smith, J. A., R. Pinkel , and R. Weller 1987. Velocity structure in the Mixed layer during MILDEX, *J. Phys. Oceanogr.* 17: 425-439

42.   Smith, J. A. 1992. Observed growth of Langmuir circulation. *J. Geophys. Res.* 97: 5651-5664

43.   Smith, J. A. 1996. Observations of Langmuir circulation, waves and mixing layer, in *the Air sea interface: Radio and Acoustic Sensing, Turbulence, and Wave Dynamics,* Edited by M. A. Donelan, W. H. Hui, and W. J. Plant, pp 613-622, Univ. Of Toronto Press, Toronto, Ont

44.   Smith, J. A. 2001. Observations and Theories of Langmuir circulation : A Story of Mixing, in *Fluid Mechanics and the Environment : Dynamical Approaches* edited by J. L. Lumley, pp 295-314, Springer, New York

45.   Stommel, H. 1951. Streaks on natural water surface. *Weather* 6: 72-74

46.   Sutcliffe, W. H., E. R. Baylor, and D. W Menzel 1963. Sea surface chemistry and Langmuir circulations. *Deep-Sea Res.* 10: 233:243

47.   Thorpe, S. A., and A. J. Hall 1980. The mixing layer of Loch Ness. *J. of Fluid Mech.* 114: 237-250

48.   Uzaki, K. I., and N. Matsunaga 2000. Wind-driven currents with Langmuir Circulations in a shallow water region *Proc. of 4th Int. Conf. on Hydro-Science and-Engineering (Academic Journal)* 4/,CD-file

49.   Walther, E. G. 1967. *Wind Streaks*. MS thesis. State Univ. N.Y., Albany. pp 31

50.   Welander, P. 1963. On the generation of wind streaks on the sea surface by action of surface film. *Tellus.* 15: 67-71

51.   Williams, K. G. 1965. Turbulent water flow patterns resulting from wind stress on the ocean. *NRL Memo. Rep. 1653* US Nav. Res. Lab

52.   Woodcock, A. H. 1944. A theory of surface water motion deduced from the wind induced motion of Physalia. *J. Mar. Res.* 5: 196-205

53.   www.whoi.edu/science/AOPE/dept/CBLAST/Location.html, Aug 2004

54.   www.whoi.edu/science/AOPE/dept/CBLASTmain.html, Aug 2004

55.   www.whoi.edu/science/AOPE/dept/CBLAST/ASIT.html, Aug 2004

THIS PAGE INTENTIONALLY LEFT BLANK

INITIAL DISTRIBUTION LIST

1.   Defense Technical Information Center
        Ft. Belvoir, Virginia

2.   Dudley Knox LibraryNaval Postgraduate School
        Monterey, California

3.   Dr. Mary L. Batteen
        Chairman of Oceanography
        Naval Postgraduate School
        Monterey, California

4.   Professor Timothy P. Stanton
        Department of Oceanography
        Naval Postgraduate School
        Monterey, California

5.   Professor Edward B. Thornton
        Department of Oceanography
        Naval Postgraduate School
        Monterey, California

6.   Captain Ahmet Turker
        Osinografi Sube Muduru
        Seyir Hidrografi ve Osinografi Dairesi Baskanligi
        Cubuklu / Istanbul / Turkey (TURKIYE)

7.   Deniz Harp Okulu Kutuphanesi.
        Deniz Harp Okulu Komutanligi
        Tuzla / Istanbul / Turkey (TURKIYE)

8   Dr. Sule Orman
        Research Assistant
        Akdeniz Universitesi Ziraat Fakultesi Toprak Bolumu
        Antalya / Turkey (TURKIYE)

9.   Professor Bulent Cihangir
        Dokuz Eylul Universitesi Deniz Bilimler ve Teknolojisi Enstitusu
        Haydar Aliyev Bulvari Inciralti / Izmir / Turkey (TURKIYE)

10.   Istanbul Teknik Universitesi
        Ayazaga Kampusu Fen Bilimleri Enstitusu
        Maslak / Istanbul / Turkey (TURKIYE)